Title

Applications of Magnetic Resonance to Current Detection and Microscale Flow Imaging

Permalink

https://escholarship.org/uc/item/2fw343zm

Author

Halpern-Manners, Nicholas Wm

Publication Date

2011

Peer reviewed|Thesis/dissertation

Applications of Magnetic Resonance to
Current Detection and Microscale Flow Imaging

by

Nicholas Wm Halpern-Manners

A dissertation submitted in partial satisfaction of the
requirements for the degree of
Doctor of Philosophy

in

Chemistry

in the

Graduate Division
of the
University of California, Berkeley

Committee in charge:
Professor Alexander Pines, Chair
Professor David Wemmer
Professor Steven Conolly

Spring 2011

Applications of Magnetic Resonance to
Current Detection and Microscale Flow Imaging

Abstract

Applications of Magnetic Resonance to
Current Detection and Microscale Flow Imaging

by

Nicholas Wm Halpern-Manners

Doctor of Philosophy in Chemistry

University of California, Berkeley

Professor Alexander Pines, Chair

Magnetic resonance has evolved into a remarkably versatile technique, with major applications in chemical analysis, molecular biology, and medical imaging. Despite these successes, there are a large number of areas where magnetic resonance has the potential to provide great insight but has run into significant obstacles in its application. The projects described in this thesis focus on two of these areas. First, I describe the development and implementation of a robust imaging method which can directly detect the effects of oscillating electrical currents. This work is particularly relevant in the context of neuronal current detection, and bypasses many of the limitations of previously developed techniques. The approach rests on a resonant interaction between an applied radiofrequency field and an oscillating magnetic field in the sample and, as such, permits quantitative, frequency-selective measurements of current density with sensitivity near the threshold required for the detection of neuronal currents. The second part of this thesis focuses on novel methodology and applications for remotely detected magnetic resonance. Remote detection separates the encoding and detection steps of a traditional magnetic resonance experiment in both time and space, allowing for high-resolution time-of-flight imaging of very small volumes of flowing nuclei. Following a discussion of the recent developments in methodology and hardware design, I present a series of remotely detected imaging experiments within microporous bead packs and organic polymer monoliths. These techniques allow for the acquisition of high-resolution images which correlate velocity, spin relaxation, and time-of-flight in previously inaccessible microscale systems.

To Mom, to Dad, and to the teachers that I had.

Contents

List of Figures

Acknowledgments

I came to Berkeley with an open mind about what I would study. Spectroscopy was a likely choice, and the subsequent involvement of lasers seemed like a given. Visions of meticulous optical alignment began to emerge from the haze, but I wanted to do this thing right: no stone unturned, no option unexplored. I decided to tack on a meeting with Alex Pines. What I didn't know was that, in addition to being a brilliant scientist, Alex can focus and transmit his boundless enthusiasm with an intensity that often leaves one a bit stunned walking out the door. I could see there was something crazy going on here, and suddenly I wanted to be a part of it. Throughout the past five years, I've had the opportunity to work on a variety of remarkable projects, none of which would have been possible without Alex. When I went looking for an idea, Alex would give me ten. Some worked and some didn't, but all of them were fascinating and unique. I have had a great time working in his lab, and I cannot thank him enough for the opportunity.

My greatest thanks go to my fellow Pinenuts, whose good humor and camaraderie make the place what it is. While I could go on for pages about the scores of amazing graduate students and post-docs, I fear it might overshadow the remainder of this work. Instead, I will quickly mention a few individuals who I have collaborated closely with over the years. First and foremost, I'd like to thank Vik Bajaj for providing a constant flow of great ideas, helpful suggestions, and excellent scotch. David Trease, who I worked with on a variety of projects during my first couple of years, could always be counted on for a laugh, even if the damn thing didn't work. Xin Zhou somehow managed to make late-night liquid xenon collection seem like a pretty good time. Jeff Paulsen taught me the remotely detected ropes and was a tremendous help in getting the bead pack work off the ground. Tom Teisseyre has been an integral collaborator on more projects than can be easily named, and I truly enjoyed the opportunity to educate him on the topic of late-January Minnesotan weather.

There is, surprisingly, a world outside of lab, complete with a number of people worth thanking. Thursdays at Triple Rock with Joey, Ryan, and Westin went a long way toward enlivening the first year physical chemistry curriculum. My knowledge of craft beer and high-class mixology was exponentially broadened by living with Will, and for that I owe him an eternal debt of gratitude. I lived within audible range of Stolarski's laughter for a solid 8 years, and would like to take this opportunity to clarify that I am still refusing to grow my moustache back. As a way to unwind, there was nothing better than a night at trivia with Mat, Sonja, Alex, Liberty, Stolarski, and Will, with every evening indeed turning out to be a wonderful*ah* occasion*ah*.

At last, there are those whose significance to these past years cannot be summed up with pithy one-liners (not that I won't try). Priya has always been there for me, ready to listen and more than ready to eat. Finally, I thank my family, who have supported me in everything that I've done and, I have to assume, will continue to do so for whatever comes next.

Chapter 1

Magnetic Resonance Primer

1.1 Nuclear Magnetic Resonance

1.1.1 Nuclear Spin

In the end, it all comes down to spin. As an intrinsic property of subatomic particles, spin defies physical analogy. Experimentally discovered in the famous Stern-Gerlach experiment of 1922 and explained by Pauli and Dirac five years later, spin is now fundamental to our understanding of modern science, enabling vast leaps in technology and knowledge. As a form of angular momentum, spin can interact with a range of forces, including electromagnetic fields, orbital motion of particles, and other spins.

In chemistry, the characteristic spin-1/2 of electrons lies at the heart of bonding and can validate predictions made from the periodic table over 100 years ago. A wealth of spin values can be found when we shift our view to nuclei. Nuclear spins can take on both half-integer and integer values and form the basis of all experiments in nuclear magnetism. These spins can range from 0 (no spin angular momentum, i.e. ^{4}He) to 1/2 (many significant nuclei, including ^{1}H, ^{13}C, ^{31}P, and ^{129}Xe) to 7 and above (nuclei with high atomic number and unusual isotopes).

The presence of spin angular momentum ($\vec{I}$) gives rise to a magnetic moment ($\vec{\mu}$) which is directly proportional to the spin:

$$\vec{\mu} = \gamma \vec{I} \tag{1.1}$$

The proportionality constant γ, known as the gyromagnetic ratio, dictates the strength of this relationship and is an intrinsic property of each nucleus. While this formula applies to electrons as well as nuclei (providing the starting point for the theory of electron paramagnetic resonance), the spins in this work are entirely nuclear in nature and any general terms (such as spin, magnetic moment, angular momentum, etc...) should be assumed to refer to nuclei unless otherwise specified.

As a consequence of this formula, any nucleus with a nonzero spin angular momentum will have a corresponding magnetic moment. The interactions between this moment and nearby magnetic fields (which could be generated from other nuclei or from an external source) are the building blocks of nuclear magnetic resonance (NMR) experiments.
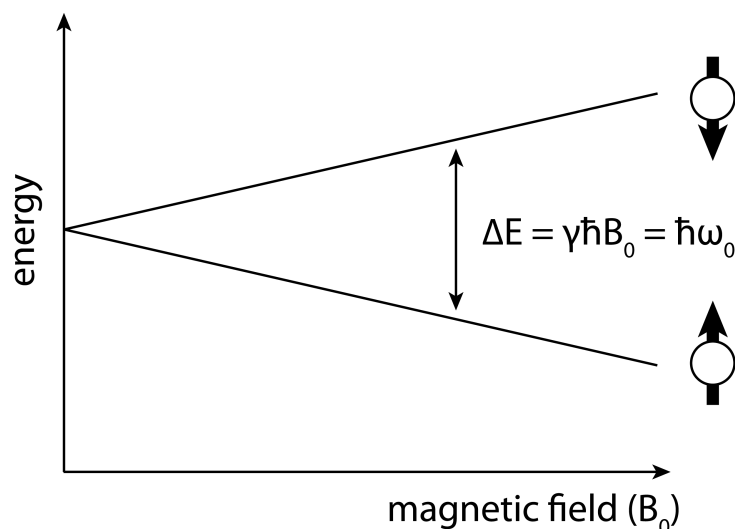
Figure 1.1: Energy level splitting due to the interaction between a nuclear magnetic moment and a static external magnetic field along $\hat{z}$, known as the Zeeman Effect. Due to this splitting, spin states which are aligned with the magnetic field $(+\frac{1}{2})$ are energetically favored.

1.1.2   The Zeeman Effect

The simplest (and most important) interaction is that between a magnetic moment and a static external magnetic field (denoted $\vec{B}$):

$$H_Z = -\vec{\mu} \cdot \vec{B} \tag{1.2}$$

If we assume the static field to be oriented along $\hat{z}$ ($\vec{B} = B_0\hat{z}$), we get:

$$H_Z = -\gamma B_0 I_z \tag{1.3}$$

The angular momentum operator I_z is defined so that when it is applied to a spin state $|m_I\rangle$, the result is $\hbar m_I |m_I\rangle$. It is then straightforward to see that in the presence of an external magnetic field along $\hat{z}$, the energy of this interaction will differ based on the quantum number m_I. For a spin-1/2 nucleus with $m_I = \pm\frac{1}{2}$, the energy difference between the $-\frac{1}{2}$ state (opposite the direction of the field, and therefore higher in energy) and the $+\frac{1}{2}$ state (aligned with the field, lower in energy) is:

$$\Delta E = E_{-1/2} - E_{+1/2} = (\frac{1}{2}\hbar\gamma B_0 + \frac{1}{2}\hbar\gamma B_0) = \hbar\gamma B_0 \tag{1.4}$$

This splitting is known as the Zeeman Effect (shown in Figure 1.1). The magnitude of this splitting is directly proportional to the strength of the external magnetic field, resulting in an increased energy bias towards the $+\frac{1}{2}$ spin state at higher magnetic field. It should be noted that this diagram corresponds to a nucleus with positive γ, as is the case with ^{1}H. The ordering of the energy levels would be reversed for any nucleus with $\gamma < 0$, such as ^{129}Xe.

We can easily rewrite this energy difference in terms of a frequency (since $\Delta E = \hbar\omega$). From this, another noteworthy formula can be extracted (note that I have changed the sign

on the energy difference in order to keep consistent notation):

$$\omega_0 = -\gamma B_0 \tag{1.5}$$

The frequency ω_0 is referred to as the Larmor frequency, and represents the transition energy between two spin states in an applied magnetic field. In typical spectroscopic fashion, we are able to stimulate transitions between spins in these two energy levels by applying radiation on resonance with ω_0. It also has tremendous significance in the classical vector description of spin dynamics, as we will discuss shortly.

1.1.3 Spin Polarization

Each nucleus with nonzero magnetic moment will interact with an external magnetic field. However, in order to observe these interactions (and, in fact, to perform any standard NMR experiment whatsoever), the magnetic moments must add up to form a net nonzero spin polarization. It is this net magnetization that we are able to manipulate with radiofrequency pulses, and which provides the oscillating magnetic flux that induces a detectable NMR signal. The calculation of this population excess is a classic topic in magnetic resonance, and, as such, is certainly worth repeating.

At thermal equilibrium, the population of a given nuclear spin state (ρ_i^{eq}) is easily determined using the Boltzmann distribution:

$$\rho_i^{eq} = \frac{\exp\left[-\hbar\omega_i/k_B T\right]}{\sum_j \exp\left[-\hbar\omega_j/k_B T\right]} \tag{1.6}$$

Defining the Boltzmann factor ξ as $\hbar\gamma B_0/k_B T$, we get:

$$\exp\left[-\frac{\hbar\omega_{\pm\frac{1}{2}}}{k_B T}\right] = \exp\left[\pm\frac{\hbar\gamma B_0}{2k_B T}\right] = \exp\left[\pm\frac{\xi}{2}\right] \tag{1.7}$$

Because ξ is small, we can expand the exponential in a Taylor series ($\exp(x) = 1 + x + \frac{x^2}{2!}\ldots$) and keep the first two terms (known as the high temperature approximation):

$$\exp\left[\pm\frac{\xi}{2}\right] \approx 1 \pm \frac{\xi}{2} \tag{1.8}$$

Thus, $\sum_j \exp\left[-\hbar\omega_j/k_B T\right] \approx 2$, and we see that $\rho_{+\frac{1}{2}}^{eq} \approx \frac{1}{2} + \frac{\xi}{4}$ while $\rho_{-\frac{1}{2}}^{eq} \approx \frac{1}{2} - \frac{\xi}{4}$. Using these populations, we can define a net polarization as $(\rho_+ - \rho_-)/(\rho_+ + \rho_-)$, which gives a thermal polarization value of $\xi/2$.

There are several important observations that can be made from this result. First, it can be easily seen that an increase in the static magnetic field will correspondingly increase the spin polarization. Likewise, a decrease in temperature will have the same effect, as there is less thermal energy available to promote population of the antiparallel spin state. For a room temperature ^{1}H experiment at 11.7 T (or 500 MHz in the parlance of NMR, where we refer to field strength in terms of the proton Larmor frequency in the magnetic field), the spin polarization is $\sim 4 \times 10^{-5}$. This is, sadly, rather small. In fact, the smallness of this number points directly towards the central problem of NMR, which is that of sensitivity.

1.1.4   Inherent Sensitivity

The quest for higher polarization is one of the guiding forces in magnetic resonance. With higher polarization comes higher sensitivity, allowing for high resolution experiments using far fewer spins. These benefits are particularly useful when dealing with low concentration samples (which is often the case when studying proteins, and is certainly relevant to the detection of trace analytes in a solution) and when performing time-consuming multidimensional experiments.

There are several ways to increase the spin polarization for an NMR experiment. As mentioned above, the most obvious of these are to increase the magnetic field or to decrease the temperature. The former has guided the trend towards larger and larger superconducting magnets over the past few decades, currently reaching fields of over 1 GHz in commercially available systems. However, these increases in field strength come at significant cost, and are delivering exponentially-dwindling returns in terms of MHz/\$. It is typically impractical to reduce the sample temperature, although notable sensitivity gains can be achieved using low-temperature cryo-probes, in which the detection coil is cooled to ~ 20 K. The coil exhibits greatly reduced thermal noise (and correspondingly enhanced sensitivity), but the technology remains specialized, costly, and time-consuming to maintain.

Due to the decreasing pace at which we can alter the polarization at thermal equilibrium, a large amount of attention has turned to alternative polarization methods. These include the hyperpolarization of noble gases by spin-exchange optical pumping [39], parahydrogen-based techniques such as PASADENA and ALTADENA [99], and the transfer of electron polarization to nuclei through Dynamic Nuclear Polarization [93] (it should be quickly noted that both γ and the spin density will play a large role in determining the net spin magnetization of a system and, in some cases such as hyperpolarized ^{129}Xe and ^{13}C, the dilute spin system and comparatively low gyromagnetic ratio may yield a magnetization that is no better than a conventional sample of water). While these methods are often fascinating and elegant applications of basic physics (and are a major area of investigation in the Pines lab), they have little relevance to the work described in this thesis and further discussion will be left to the literature.

1.1.5   Experimental Sensitivity

Sensitivity also comes into play on a basic hardware level, and is a major factor in the design and construction of radiofrequency magnetic resonance probes. While a detailed overview of probe construction is beyond the scope of this work, there are several important observations to note.

In a conventional experiment, a sample of nuclei (in solid, liquid, or gaseous form) sits within a probe, a piece of equipment housing a radiofrequency coil (commonly a solenoid, helmholtz coil, birdcage coil, or surface coil) and electronics which can be adjusted to form a resonant LC circuit. This process of adjustment is known as tuning and matching, and typically consists of making slight, iterative changes to a pair of variable capacitors in the circuit in order to match the probe resonance to the Larmor frequency. The coil and circuitry are housed within the probe body, which is itself inserted into the bore of the magnet such that the sample will sit directly within the homogeneous region of the magnet (known as the
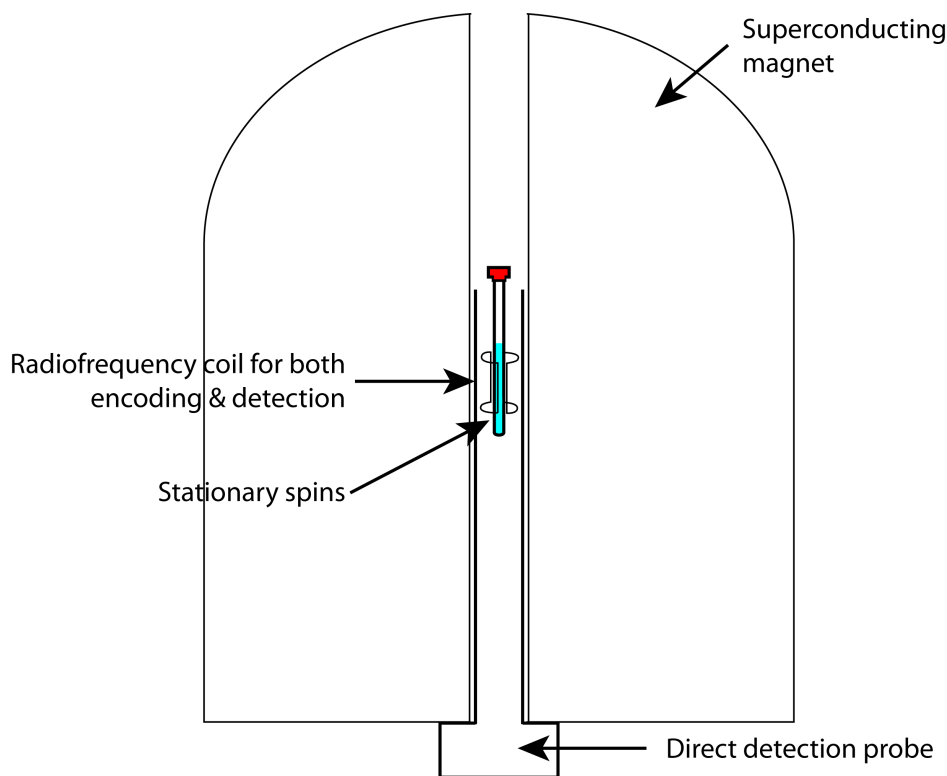
Figure 1.2: Cartoon showing the basic hardware setup for a directly detected NMR experiment.

"sweet spot"). A simple cartoon of a typical NMR setup for a direct detection experiment is shown in Figure 1.2.

This coil has two essential functions, referred to as "encoding" and "detection." In the encoding step, the coil is used to transmit resonant radiofrequency pulses, which interact with the spins, causing them undergo a series of rotations, flips, and other nuclear gymnastics in order to carry out the experiment and generate the desired information (which could be a spectrum, image, or a complex multidimensional dataset). This phase of the experiment is represented by a "pulse sequence," which provides a visual outline to the parameters in this complex dance. The second function of the coil is detection. In order to recover the information generated during encoding, the net spin magnetization is typically made to precess in the transverse plane (discussed below in Section 1.1.6), where the rotating magnetic flux induces detectable current flow within the coil.

In the encoding step, the design of the coil and the geometry of the sample are not terribly important, at least with respect to having all nuclei in the sample experience the pulses (however, the homogeneity and efficacy of the pulses can be very dependent on coil design and sample geometry). These concerns of are of much greater significance when it comes to detection. Smaller samples will clearly possess a smaller net magnetization, and the signal is therefore diminished (in comparison with a larger number of nuclei present in the same coil).

This form of sensitivity is usually discussed in terms of the signal-to-noise ratio (SNR). It

is easy to understand that, in an NMR experiment where the coil and sample geometries are fixed, an increase in sample concentration will cause an increase in the SNR. However, for the experiments discussed later in this thesis, our interests lie in the situation where these geometries can be changed at will. The parameter of interest in this situation is known as the filling factor, which reflects how well the volume of the coil is occupied by the sample. If the filling factor is low (for instance, a 150 μm capillary placed inside of a 10 mm coil), the SNR will be much worse than for a coil and sample with filling factor close to 1.

For our purposes, it's not the amount of sample that is present (you could have a sample tube 10 m in diameter which would still yield terrible results when placed in a 10 km diameter coil), it's how well the coil encloses the sample. The quantification of this principle was done by Hoult and Richards in 1976 [57], providing a formula for the SNR in an NMR experiment for any coil geometry of interest. In the case of a solenoid, the magnetic field generated over the sample volume (per unit current) is given by:

$$\frac{B_1}{i} = \frac{\mu_0 n}{d_c\sqrt{1 + (h/d_c)^2}} \tag{1.9}$$

where d_c is the diameter of the coil and h is the height. From this formula it is already apparent that a decrease in coil diameter will positively impact the sensitivity of the experiment. For solenoids with diameter greater than 100 μm, the formula above can be used to estimate the SNR (per unit volume) [77]:

$$(S/N)_{puv} = \frac{\omega_0^2 \left[n/d_c\sqrt{1 + (h/d_c)^2} \right]}{\sqrt{n^2 d_c \omega_0^{1/2}/h}} \propto \frac{\omega_0^{7/4}}{d_c} \tag{1.10}$$

where ω_0 is the Larmor frequency and n is the number of turns in the solenoid. In addition to further fueling the drive towards bigger magnets and higher Larmor frequencies, this formula clearly shows an inverse scaling between SNR and diameter of the coil (and thus, filling factor). Given that the detection of very small volumes of nuclei is a primary focus of this thesis, it should not be surprising that one of the major design choices in our experimental hardware is the use of microsolenoid detectors [101].

1.1.6 Vector Model & Larmor Precession

Returning from our brief foray into hardware concerns, it is now appropriate to provide a quick description of the spin dynamics during an NMR experiment. In order to do this, we use a classical vector description of the spin magnetization, a model which is more than sufficient to describe the essential experiments in magnetic resonance.

As discussed above, a population of nuclear spins will have a nonzero polarization in an external magnetic field. This net magnetization can be represented in the cartesian coordinate system of the lab as a vector, which will be oriented along the magnetic field at thermal equilibrium (by convention, this is $\hat{z}$).

This magnetization vector can be easily manipulated using well-defined radiofrequency pulses at resonance with the Larmor frequency (the mechanism of these pulses is discussed shortly). Using these pulses to generate rotations, the spin magnetization can be tipped
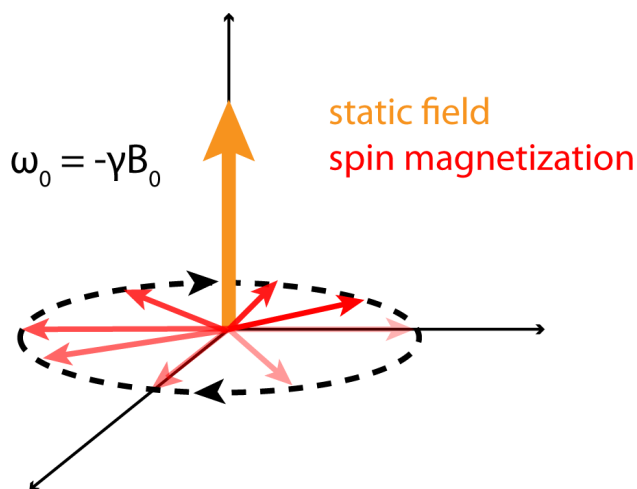
Figure 1.3: Larmor precession in the lab frame.

away from the static magnetic field. At this point, with the magnetization no longer aligned along $\hat{z}$, it begins to precess. This phenomenon is known as Larmor precession, and will occur in any situation where there is non-equilibrium magnetization in a magnetic field. If the field is along $\hat{z}$, the precession will occur in the orthogonal xy plane (shown in Figure 1.3) generating a rotating flux in the transverse plane which gives rise to the detectable magnetic resonance signal discussed above. The frequency of this precession is simply the Larmor frequency, $\omega_0 = -\gamma B_0$, providing an elegant link between the classical and quantum points of view.

1.1.7 Bloch equations

In order to formalize the vector model of magnetic resonance, one needs to have equations of motion which are able to describe spin dynamics in the presence of nearby magnetic fields. This behavior can be nicely captured in a tidy formalism known as the Bloch equations:

$$\frac{d\mathbf{M}(t)}{dt} = \gamma \mathbf{M}(t) \times \mathbf{B}(t) \tag{1.11}$$

Here, $\mathbf{M}(t)$ represents the trajectory of the spin magnetization and $\mathbf{B}(t)$ the time-varying or constant magnetic fields. This set of differential equations can be solved with relative ease, providing a natural description of phenomena such as Larmor precession and spin rotations which can be further modified to provide for relaxation in non-equilibrium systems.

We will briefly consider the two examples mentioned above: Larmor precession and spin rotation by a resonant radiofrequency pulse. For the first, we can set $\mathbf{B}(t)$ to $B_0\hat{z}$, the static

external magnetic field:

$$\frac{dM_x(t)}{dt} = \gamma M_y B_0 \tag{1.12}$$

$$\frac{dM_y(t)}{dt} = -\gamma M_x B_0 \tag{1.13}$$

$$\frac{dM_z(t)}{dt} = 0 \tag{1.14}$$

The solutions to these equations are:

$$M_x(t) = C_1 \cos(\gamma B_0 t) + C_2 \sin(\gamma B_0 t) \tag{1.15}$$
$$M_y(t) = C_2 \cos(\gamma B_0 t) - C_1 \sin(\gamma B_0 t) \tag{1.16}$$
$$M_z(t) = 0 \tag{1.17}$$

Choosing an initial non-equilibrium magnetization along $\hat{x}$ ($\mathbf{M}_0 = M_x \hat{x}$), we get $M_x(t) = M_x \cos(\gamma B_0 t)$ and $M_y(t) = -M_x \sin(\gamma B_0 t)$, which is exactly the Larmor precession described above.

The second example describes the rotation induced by a radiofrequency pulse with frequency resonant to the Larmor frequency, i.e. $\mathbf{B}_{RF}(t) = B_{RF} \cos(\omega_{RF} t + \varphi_P)\hat{x}$. This pulse represents a radiofrequency magnetic field which is oscillating along $\hat{x}$. Traditionally, this field is rewritten as a sum of two counter-rotating components:

$$B_{RF}\cos(\omega_{RF}t + \varphi_P)\hat{x} = \begin{cases} \frac{1}{2}B_{RF}(\cos(\omega_{RF}t + \varphi_P)\hat{x} + \sin(\omega_{RF}t + \varphi_P)\hat{y}) & \text{resonant} \\ \frac{1}{2}B_{RF}(\cos(\omega_{RF}t + \varphi_P)\hat{x} - \sin(\omega_{RF}t + \varphi_P)\hat{y}) & \text{non-resonant} \end{cases}$$

The situation of interest is when we fulfill the resonance condition, $\omega_{RF} \approx \omega_0$. In this case, the two magnetic fields describe rotating vectors in the transverse plane, which precess in opposing directions at the Larmor frequency. Only one of these two will match the direction of rotation inherent in Larmor precession, allowing us to drop the non-resonant second equation in most circumstances. This is known as the Rotating Wave Approximation (note, in some cases it is not appropriate to drop this term, as discussed at the end of Section 2.2.3). Now, the Bloch equations can be written:

$$\frac{dM_x(t)}{dt} = \gamma \left[M_y B_0 - \frac{1}{2} M_z B_{RF} \sin(\omega_0 t + \varphi_P) \right] \tag{1.18}$$

$$\frac{dM_y(t)}{dt} = -\gamma \left[M_x B_0 - \frac{1}{2} M_z B_{RF} \cos(\omega_0 t + \varphi_P) \right] \tag{1.19}$$

$$\frac{dM_z(t)}{dt} = \gamma \left[\frac{1}{2} M_x B_{RF} \sin(\omega_0 t + \varphi_P) - \frac{1}{2} M_y B_{RF} \cos(\omega_0 t + \varphi_P) \right] \tag{1.20}$$

These equations can certainly be solved as is, but it is far simpler (and particularly instructive to later discussions) if we first make a simple adjustment to the frame of reference.

1.1.8   Reference Frames

By now it should be clear that the Larmor frequency lies at the heart of all things NMR. Energy at this frequency will initiate transitions between spin quantum states, rotation at this frequency is a natural phenomenon when magnetization is tipped away from equilibrium, and, as we are in the process of showing, radiofrequency pulses resonant to this frequency can produce spin rotations. We know that spin magnetization will rotate around B_0 in any situation where the magnetization possesses components in the transverse plane. As these situations describe nearly all of the interesting parts of an NMR experiment, it makes sense to try to simplify our picture and remove the need to keep track of this dizzying precession.

To do this, we can change our frame of reference to one rotating at the Larmor frequency. In the quantum mechanical description of magnetic resonance, this is easily accomplished through a mathematical similarity transform, which moves the Hamiltonian into the rotating frame without much fuss. In the classical vector model, one can take oscillatory linear combinations of the cartesian axes such that the new coordinate system rotates in the proper direction with frequency ω_0. Rather than dwelling on the specific mathematics of how to do this, the discussion here will simply rely on intuitive statements, which are more relevant and useful in the context of this work.

The first of these is that, in a frame of reference rotating at ω_0, a radiofrequency pulse rotating at the Larmor frequency will appear stationary in the rotating frame. Thus, we can rewrite $\frac{1}{2}B_{RF}(\cos(\omega_0 t + \varphi_P)\hat{x} + \sin(\omega_0 t + \varphi_P)\hat{y})$ as $\frac{1}{2}B_{RF}\hat{x}$ (making the choice of $\varphi_P = 0$). In the rotating frame, the resonant radiorequency pulse now appears as a static magnetic field along $\hat{x}$.

The second observation is that we may now neglect the $B_0\hat{z}$ term when writing our rotating frame Bloch equations. As shown above, this term will result in a description of Larmor precession. Since our frame is now rotating at the Larmor frequency, this precession disappears and spins will appear stationary. Therefore, in the rotating frame, our Bloch
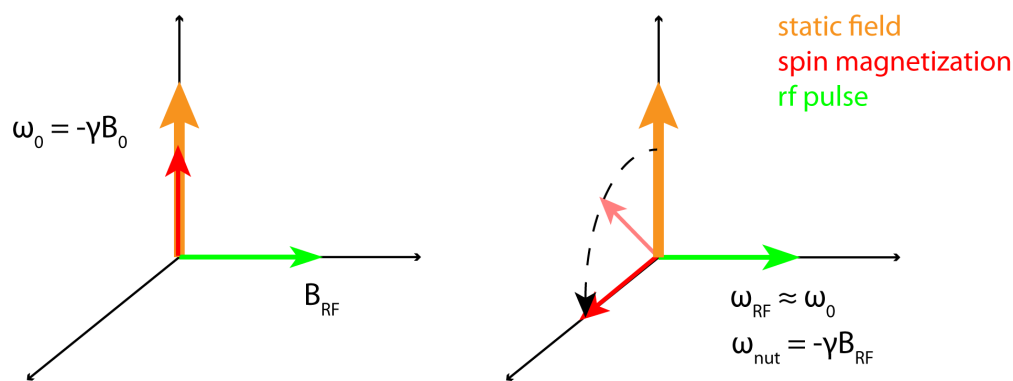
Figure 1.4: Rotation of spin magnetization by a resonant radiorequency pulse, as shown in the rotating frame of reference.

equations become:

$$\frac{dM_x(t)}{dt} = 0 \tag{1.21}$$

$$\frac{dM_y(t)}{dt} = \frac{1}{2}\gamma M_z B_{RF} \tag{1.22}$$

$$\frac{dM_y(t)}{dt} = -\frac{1}{2}\gamma M_y B_{RF} \tag{1.23}$$

This set of equations is identical to Eqs. 1.12-1.14 after a simple coordinate system rotation and a change from B_0 to $\frac{1}{2}B_{RF}$. As such, the solution will be much the same: a precession about the stationary magnetic field (here, the rotating frame version of the resonant pulse). Starting at equilibrium ($\mathbf{M}(t) = M_z\hat{z}$), the trajectory of the components is given by $M_x(t) = 0$, $M_y = M_z\cos(\frac{1}{2}\gamma B_{RF}t)$, and $M_z = -M_z\sin(\frac{1}{2}\gamma B_{RF}t)$. We can now define $\omega_{nut} = -\frac{1}{2}\gamma B_{RF}$, which is known as the nutation frequency. This frequency describes a precession in the yz plane about $\hat{x}$ (shown in Figure 1.4), and is completely analogous to the lab frame Larmor precession described earlier.

In addition to illustrating the mechanism of the primary tool in NMR pulse sequences, the previous discussion shows several equivalencies between static and oscillating magnetic fields when considering different frames of reference. This particular concept is of great significance when discussing the resonant current detection work further on (Section 2.2.3 in particular). While the later pulse sequence may initially appear unclear in its effects, the mechanism is easily understood through a change in reference frames and analogy to the effects of resonant radiofrequency pulses discussed here.

1.1.9 Relaxation

Relaxation is a fact of life and a fundamental part of magnetic resonance. In some cases it's good, in many it's bad, and in all of them it's unavoidable. There are two major types of spin relaxation, referred to as T_1 (spin-lattice relaxation) and T_2 (spin-spin relaxation). The discussion here focuses on giving a concise description of the causes and effects of these relaxation forms, and how they relate to the experiments discussed later in this work. A more specialized form of relaxation within the rotating frame, known as $T_{1\rho}$, is particularly relevant for discussing the current detection experiments and is discussed in Section 1.1.11.

$\mathbf{T}_1$

Much of the preceding discussion has focused on the behavior of spins moved away from their equilibrium configuration. This is an unnatural state of affairs: these states are higher in energy, and any nucleus within them will do all that it can to return to its natural state of rest. Here, thermal equilibrium describes a situation in which the net magnetization is aligned with the external static magnetic field. When the magnetization is rotated into the transverse plane (through the action of a radiofrequency pulse), it will no longer be in the most favorable energy configuration, and will take advantage of any mechanisms available to realign with the field.
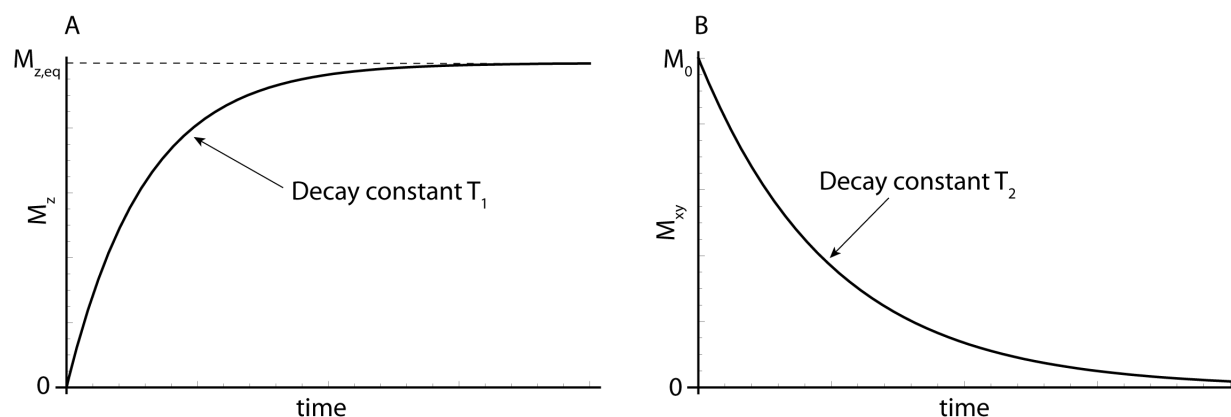
Figure 1.5: Relaxation of magnetization by (a) T_1 and (a) T_2 mechanisms.

This recovery of the longitudinal magnetization is often called spin-lattice relaxation, which refers to the interaction of a spin with the magnetic fluctuations caused by molecular motion within the larger "lattice" of surrounding nuclei. These motions, in the form of vibrations and rotations of nearby molecules, lead to fluctuations in the local magnetic field. In the absence of fluctuations, a non-equilibrium spin in the transverse plane would have no obvious method to return to $\hat{z}$. In order to recover the longitudinal magnetization, we would require the presence of magnetic fields able to produce such a rotation. If the static field along $\hat{z}$ were the only field available, we'd be out of luck: the only rotation it's going to produce is Larmor precession in the xy plane. However, if these local fluctuations happen to produce temporary magnetic fields with transverse components, we suddenly have a way for our non-equilibrium spin to begin the climb back up to $\hat{z}$. With each step, the energetic situation grows more favorable, and the nucleus will inevitably find its way home.

When considered in the context of the bulk magnetization, this process is described by an exponential growth of longitudinal magnetization, and can be written as:

$$M_z(t) = M_{z,eq}\left(1 - \exp^{-t/T_1}\right) \tag{1.24}$$

where T_1 describes a time constant for this relaxation. This recovery of longitudinal magnetization from the transverse plane is shown in Figure 1.5a.

Spin-lattice relaxation has a number of very significant effects on the way experiments are performed in magnetic resonance. First, T_1 places a restriction on how frequently we can repeat an experiment which begins from a state of thermal equilibrium. The most basic experiment, sometimes referred to as a "pulse-acquire," is an illustrative example. At the start of the pulse sequence, the net spin magnetization is found at thermal equilibrium, aligned along $\hat{z}$. A resonant radiofrequency pulse is applied, causing rotation of the spins away from the longitudinal axis. After a pre-calibrated amount of time τ_{90}, the pulse is stopped so that the magnetization lies completely within the xy plane. The magnetization precesses around $\hat{z}$, creating an oscillating magnetic flux which can be detected by a radiofrequency coil. In many cases, a number of these experiments will be performed sequentially, for purposes such as signal averaging or the cancellation of unwanted components of the signal by introducing small variations in the pulse sequence (known as phase cycling).

In order to make sure that each experiment is equivalent (leaving aside any differences introduced by the user), the spin magnetization must return to full thermal equilibrium after each acquisition. The amount of time that this takes is dictated by T_1, and can often be on the order of seconds. Furthermore, a duration of 3 - 5 T_1 should be used in order to ensure that the spins have returned to full equilibrium. Considering that a typical pulse-acquire experiment may only take 100 ms, this relaxation delay can become a severe bottleneck. In complex experiments involving multiple dimensions and intricate phase cycling, thousands of acquisitions may be necessary, meaning that any small additional delay between acquisitions can result in compounded delays which are several orders of magnitude longer.

There are a number of methods which may be used to alleviate these difficulties in certain situations. For instance, experiments can be performed using smaller tip angles. If a 30° pulse is used rather than a full 90°, the amount of time required for recovery of longitudinal magnetization will be dramatically decreased, although at the cost of a decrease in detectable signal in the transverse plane. However, if the quantity of experiments takes precedence over the quality, this is a viable option. Additionally, the intrinsic T_1 of a sample can be altered through the addition of a dopant, usually a paramagnetic metal complex such as $GdCl_3$. The unpaired electron spins in these complexes will interact with nearby nuclear spins, facilitating relaxation and dramatically decreasing T_1 and T_2. One example of this practice can be found in the current encoding experiment detailed in Chapter 2, where paramagnetic doping was used in order to decrease the amount of time required to take current-encoded images (image resolution is typically dependent on the number of acquisitions, meaning that long T_1 values can dramatically impede experiment duration).

Not all effects of T_1 are undesirable. The fact that spin magnetization may undergo complex manipulations and retain its configuration for seconds (or even minutes and hours, in some systems) is quite remarkable, and allows a great deal of latitude in applying lengthy pulse sequences and studying dynamical processes on a variety of timescales. In particular, T_1 is of fundamental importance to the remote detection experiment first discussed in Chapter 2.3.3. The basic principle of remote detection relies on the ability to transport information (carried by spins with encoded magnetization stored along $\hat{z}$) from one location to another, where it can be re-excited and recovered. If this transport can be accomplished in an amount of time smaller than the longitudinal relaxation, the information is preserved. It is therefore of utmost importance that T_1 be long enough for this to occur, and the value of the relaxation constant often serves as the deciding factor in figuring out whether or not an experiment can be done.

T_2

If T_1 provides the primary limitation on time between pulse sequences, then T_2 provides the corresponding limit on time within them. While the simplicity of the vector model of magnetic resonance is quite powerful, it fails to convey the sense of what is occuring with the individual spins that are summed up to form the net magnetization. At thermal equilibrium, the net magnetization lies along $\hat{z}$, a configuration where spins are relatively impervious to local variations in the longitudinal magnetic field. Following an excitation into the transverse plane, the initial individual vectors will be mostly aligned along an axis orthogonal to the excitation pulse. After this, things begin to diverge.

Since each one of these spins occupies a different environment (whether locally or within the macroscopic sample), their behavior will differ in small but significant ways. Small differences in the local magnetic field will cause spins to precess at slightly different speeds (here, longitudinal fluctuations are what will change precession frequency), causing the individual magnetization vectors to "spread out" in the xy plane according to their speed of precession. The effect of this, when viewed in the context of a bulk magnetization vector is that the transverse magnetization decays, with time constant T_2 (shown in Figure 1.5b):

$$M_{xy}(t) = M_0 \exp^{-t/T_2} \tag{1.25}$$

It is worth making a subtle, but important distinction at this point. The spread of individual magnetization vectors in the transverse plane, caused by differences in the local magnetic field, can arise from two different sources. The first of these can be ascribed to random magnetic field fluctuations due to molecular motion, much the same as with T_1. Since these fluctuations have no specific order, whether temporally or spatially, there is no way one can anticipate or correct for their effects. On the other hand, one may have local field differences which are caused by a more ordered source.

The primary example of this can be found in situations where there are inhomogeneities in the magnetic field throughout the sample. These can be caused by poor shimming, paramagnetic impurities, or through the magnetic susceptibility gradients which arise at the boundaries between materials with inherently different magnetic properties (for a relevant example of this, please see Section 4.3.3, where T_2 values are examined for liquid flowing through a microporous bead pack). In this case, the spread in transverse magnetization is caused by differences in the longitudinal magnetic field at each spin rather than by random fluctuations.

The net transverse relaxation is, therefore, a sum of the effects from these two different mechanisms. The first of these, totally random and unavoidable in its effects, is simply referred to as T_2. However, this relaxation value will be obfuscated by the presence of nonrandom disorder, here referred to as T_2^{inhom}. The observable relaxation value is therefore a combination of the two, and is known as T_2^*:

$$\frac{1}{T_2^*} = \frac{1}{T_2} + \frac{1}{T_2^{inhom}} \tag{1.26}$$

If the local inhomogeneities or interactions remain constant or vary in predictable ways, it is not unreasonable to think that a form of compensation could be implemented. To learn more about this, we turn to a quick discussion of the spin echo, one of the key foundations of modern NMR.

1.1.10 The Spin Echo

First invented in the 1950 by the illustrious Erwin Hahn [44], the spin echo is an incredibly powerful building block for experiments in magnetic resonance. As has been described, the main portion of most pulse sequences takes place when the net spin magnetization has been tipped away from its equilibrium position and lies, at least partially, in the transverse plane. As sequences grow increasingly complicated, with numerous pulses instigating all manner
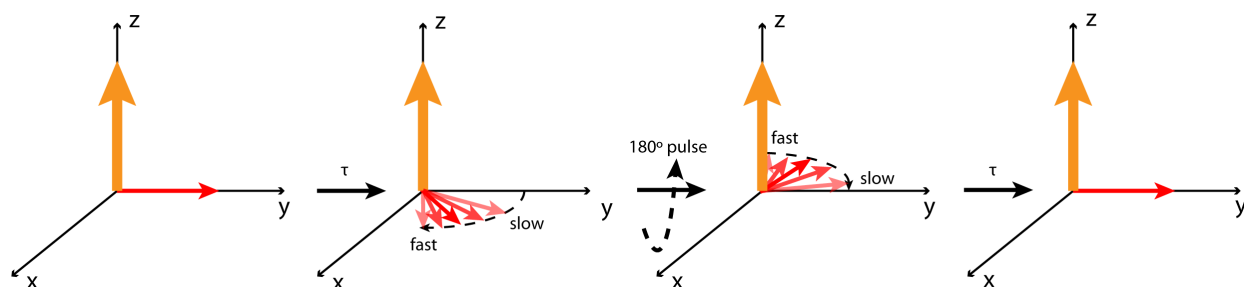
Figure 1.6: Vector diagram showing the effects of a spin echo pulse sequence.

of spin acrobatics, it becomes very important that we have ample time to get through our sequence before the transverse magnetization relaxes. While the incoherent nature of T_2 prevents us from alleviating the effects of intrinsic spin-spin decay, we have far more options when it comes to T_2^{inhom}. If we can remove this decay from our observed T_2^*, we at least have a chance to greatly prolong the duration of transverse magnetization.

The way to accomplish this is through a spin echo, which is shown in Figure 1.6 and proceeds as follows. We start from an initial situation in which the net spin magnetization has been rotated into the transverse plane by a resonant radiofrequency pulse. Immediately following this pulse, all transverse spin magnetization will remain aligned. Allowing the spins to precess for a time τ will cause the effects of T_2 and T_2^* to manifest themselves as the magnetization spreads apart due to slight differences in precession frequencies. If we consider only the effects due to spatial inhomogeneities in the magnetic field, we can see that certain spins will lag behind while others speed ahead, depending on the strength of their local field. At this point, a 180° pulse (also referred to as a π pulse) is applied along $\hat{y}$. The resulting rotation of spin magnetization serves to mirror the spread of vectors across $\hat{y}$, where they continue to precess in a clockwise direction. At this point, we see that the slow moving spins, previously at the back of the pack, are now correspondingly closer to $\hat{y}$, while the fast spins are now in back.

The key insight is that since the local inhomogeneities causing T_2^* relaxation are consistent, the slow spins will remain slow, the fast spins will remain fast, and all of them will end up exactly aligned along $\hat{y}$ if we wait an identical time τ. The ability to refocus the spin magnetization to its original value (aside from the irreversible effects of T_1 and T_2) is incredibly powerful, and a fascinating example of time-reversal symmetry at work. Spin echoes and their progeny are ubiquitous elements of magnetic resonance pulse sequences, allowing for highly complex experiments with a minimum of signal loss and excellent cancellation of inhomogeneity-based artifacts. Spin echoes make an appearance in nearly all pulse sequences described in this work, from remote detection (where they serve to recover the full amount of signal immediately prior to storage of the encoded magnetization) to resonant current imaging (where they form the backbone of the spin echo imaging sequence, chosen to minimize inhomogeneity-based artifacts).

1.1.11 Spin Locking and Relaxation in the Rotating Frame

There is one final mode of relaxation which is relevant to the current detection experiments described in Chapter 2. This relaxation, known as $T_{1\rho}$, takes place within the rotating frame of reference, during a specialized pulse called a spin lock.

To understand the spin lock, we must first travel back into the rotating frame of reference. As discussed in Section 1.1.8, this vantage point allows us to greatly simplify the description of many magnetic resonance experiments. The static magnetic field along $\hat{z}$ is gone from our vector diagram, and any pulse with frequency resonant to ω_0 will appear static in the transverse plane.

To start, imagine a situation where the spin magnetization has been tipped down along $\hat{y}$. If the spins continue to precess at exactly ω_0, they remain completely aligned along $\hat{y}$. As we have discussed, this is not quite the case; slight variations in the Larmor frequency arise from a variety of sources, and even if we eliminate inhomogeneous broadening using a spin echo, we will still experience the random fluctuations giving rise to T_2 decay. In the rotating frame, the "spreading" of spin magnetization from T_2 will appear as a spreading away from $\hat{y}$ in both positive and negative directions. Any spins with precession frequencies below ω_0 will slowly fall away from $\hat{y}$, while those precessing faster will slowly gain ground. Since this is all still centered on ω_0, the net magnetization vector will simply shrink along $\hat{y}$.

Now, consider what happens if we apply a continuous resonant pulse along $\hat{y}$. In the rotating frame, this pulse is static. If all of the spins remained exactly aligned along $\hat{y}$, it would have absolutely no effect, and would serve as a sort of pseudo-static field when viewed from the rotating frame of reference. However, if our spin magnetization begins to pull away from $\hat{y}$ due to T_2, this pulse kicks into action with a rather interesting effect. In the rotating frame, any off-resonant components which tip away from $\hat{y}$ will be pulled into a precession about the spin lock pulse, exactly the same as with lab frame Larmor precession. The spread of magnetization caused by T_2 will be pulled back (or pushed forward) by precession around $\hat{y}$, effectively cancelling out the influence of relaxation and "locking" the spin magnetization onto the y-axis. This is really nothing more than thermal equilibrium with a static field along $\hat{y}$, and can be an excellent way to investigate processes occuring on longer timescales, such as chemical exchange.

However, the situation is by no means relaxation-free. It is true that, as long as the spin lock pulse remains on, the magnetization will remain locked to its axis. The intensity of the magnetization along that axis is what decays, on a timescale characterized by a new relaxation constant $T_{1\rho}$. What does this decay represent? To come up with an intuitive answer, we need to step back to the notion of polarization. In a static field along $\hat{z}$, we know that spins will come to a thermal equilibrium with net polarization given by $\xi/2$, where $\xi = \hbar\gamma B_0/k_B T$. The value of the polarization depends directly on the strength of the magnetic field. Therefore, if we are describing a new equilibrium within the rotating field, defined by a "static" spin lock pulse along $\hat{y}$, we also need a new rotating frame polarization due to this field. Because the spin lock pulse is far weaker than the external magnetic field, this polarization will be much smaller.

Following an initial 90° pulse and immediate application of a spin lock along the magnetization axis, the level of spin polarization will remain at the thermal equilibrium characteristic to the external field ($M_{z,eq}$). Along the rotating frame spin lock axis, this is a highly non-
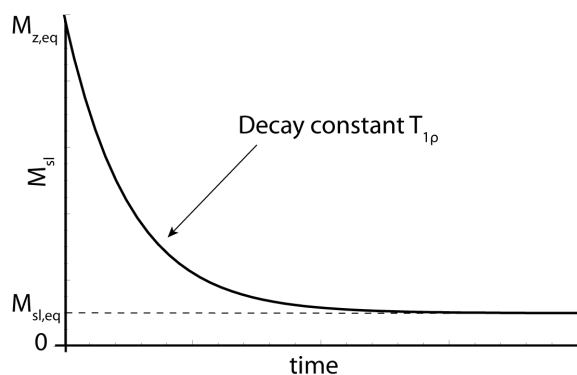
Figure 1.7: Relaxation of rotating frame spin-locked magnetization by a $T_{1\rho}$ mechanism.

equilibrium state of affairs. Therefore, the locked magnetization will decay from its initial (large) value to the polarization one would expect due to the strength of the spin lock pulse ($M_{sl,eq}$, which is much smaller). Mathematically, this can be written:

$$M_{sl}(t) = (M_{z,eq} - M_{sl,eq}) \exp^{-t/T_{1\rho}} + M_{sl,eq} \tag{1.27}$$

As mentioned, the timescale for this decay is given by $T_{1\rho}$. The decay curve for the spin locked magnetization is shown in Figure 1.7. A fair number of experiments, particularly in medical imaging [125][30][114], make use of spin locking experiments to mimic low-field conditions within a high-field rotating frame of reference. This idea is the heart of the resonant current imaging experiments further on, where it will be discussed in greater detail.

1.1.12 The NMR Signal

Having spent a fair amount of time describing what happens during an NMR experiment, it is now a good time to step back and consider the sort of data that is acquired at the end of it. The source of the NMR signal has already been suggested: as the encoded magnetization vector precesses about the static field, it creates a detectable magnetic flux, oscillating at the characteristic frequency of rotation. Using inductive detection in an enclosing radiofrequency coil, this flux is measured and sent on to the spectrometer for amplification and digitization.

Consider several cases. First, an experiment free from the effects of relaxation, where the measured rotation frequency is exactly on resonance with ω_0. In the lab frame, the signal would show up as a sinusoid, oscillating at the Larmor frequency. If we are able to subtract the Larmor frequency (essentially performing a transformation into the rotating frame of reference), the signal would be a straight line with height dictated by the intensity of the signal. Now, add the effects of relaxation. With T_1 and T_2 mechanisms active, the magnitude of the transverse magnetization will decay during the course of the measurement. The resulting signal will appear as an oscillation (lab frame) or line (rotating frame), contained within an envelope showing characteristic relaxation-based exponential decay. This is known as a Free Induction Decay (FID). Next, look at the case where the oscillation frequency is off resonance by $\Delta\omega$. The lab frame FID will show a frequency of $\omega_0 + \Delta\omega$, while the rotating frame FID will now have frequency $\Delta\omega$. Finally, consider a situation where multiple spins
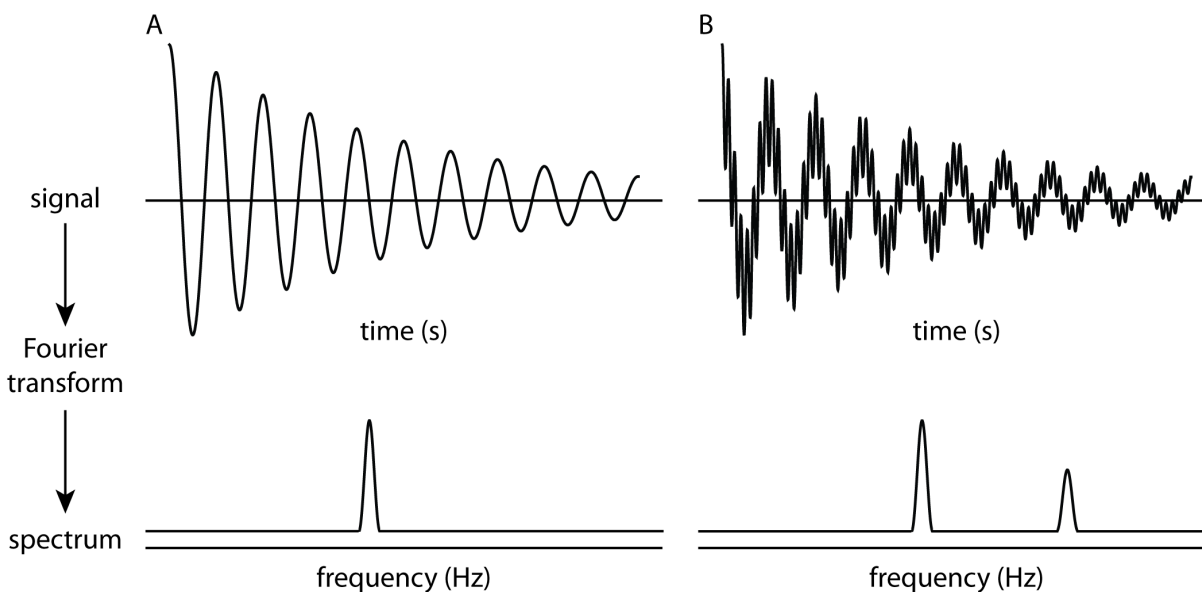
Figure 1.8: Fourier transformation of FIDs containing one (a) and two (b) off-resonant frequencies.

are precessing simultaneously, at ω_0 and $\omega_0 \pm \Delta\omega$. The measured FID for this experiment will be modulated by multiple frequencies, with a slightly more complex appearance.

The determination of which frequencies make up the measured NMR signal is the end result of most experiments. If all spins oscillated at exactly the Larmor frequency, there would be very little of interest to the technique. Instead, we find a wide diversity in behavior, enabling experiments which can be used to assign chemical structures, measure bond distances, study dynamic processes, and so on. While many of the factors that can alter the precession of magnetization are basic elements of any introductory NMR class (such as the chemical shift, J-coupling, and dipole-dipole coupling), they are not required to understand the methods developed in this work. Detailed discussion of the NMR lineshape is also not required for these methods. Instead, we will state that T_2 relaxation increases linewidth (with the Full Width at Half Maximum $\propto 1/\pi T_2$) and leave it at that.

The method by which we determine the constituent frequencies is the Fourier transform, which takes an input signal in time (here, the FID) and transforms it into an output spectrum in frequency. The formula to accomplish this can be written as:

$$F(\omega) = \int_{-\infty}^{\infty} f(t) \exp^{-i\omega t} dt \tag{1.28}$$

Examples of the Fourier transform on signals containing one frequency and multiple frequencies are shown in Figure 1.8. The collection of an FID and subsequent application of a Fourier transform are procedures common to nearly all experiments in magnetic resonance, and those described in this work are no different. However, rather than obtaining spectra, the majority of these experiments produce images.

1.2 Magnetic Resonance Imaging

At this point, our discussion has covered a core selection of important topics in NMR. The choice of these topics is unapologetically biased; while there are countless areas of research in magnetic resonance that are fascinating and applicable, only a small subset have direct relevance to the experiments in this work. One could speak at length about the intricate details of spectrometer design or the myriad of multidimensional experiments, but these are topics better left to the textbooks. The areas of NMR discussed in Section 1.1 form a nearly complete foundation upon which the relevant discussion can stand. The one significant area yet to be discussed is magnetic resonance imaging, a topic unto itself.

From personal experience, whenever someone in magnetic resonance attempts a cocktail party explanation of their work, it's always easiest to add a phrase similar to, "a lot of our applications are in MRI." Despite the stature of NMR as an analytical tool of tremendous power and widespread application, it remains relegated to the somewhat obscure class of scientific experiments that are mostly unknown to the general population. Not so with MRI. In the field of medical imaging, MRI provides a unique way to perform high-resolution, noninvasive, and nondestructive imaging experiments, providing medical practitioners with unparalleled insight on conditions from broken bones to metastatic tumors. As a phrase, MRI is tossed around frequently and casually, and the field is big business.

While the bulk of MRI research is directed towards medical applications, there's clearly more that can be achieved with this powerful imaging method. Nearly all of the experiments in this thesis depend on MRI in one way or another, making it an important topic to cover before diving in. To that end, we will now highlight a selection of the most critical concepts in MRI, with an eye aimed towards subjects that are specifically relevant to the subsequent experiments.

1.2.1 The Principle of MRI

In its most basic form, MRI is a very simple experiment to understand. Consider a situation where an object is placed in the magnet. The object has a distinct 1-dimensional profile, with peaks and slopes and troughs, spread across the axis which defines the profile. If we were to perform an NMR measurement as usual, the detected signal would be made up of contributions from all nuclei in the object, with precession frequencies unaffected by their spatial location. This isn't a whole lot of use for imaging. What we want is some way to encode the spatial location of each nucleus directly into its frequency, such that we can separate the net detected signal according to location.

The straightforward way to do this is to apply a gradient in the longitudinal magnetic field. With the addition of this gradient on top of the existing static field, we find that the total magnetic field is given by:

$$\vec{B}(\vec{r}) = (B_0 + \vec{G} \cdot \vec{r})\hat{z} \tag{1.29}$$

where $\vec{G} = G_x\hat{x} + G_y\hat{y} + G_z\hat{z}$. For a simple 1-dimensional linear gradient along $\hat{x}$, we have $\vec{B}(x) = (B_0 + G_x x)\hat{z}$, with G_x given in units of magnetic field per distance, i.e. G/cm. With an applied linear gradient, the Larmor frequency becomes dependent on position ($\omega_0(x) =$
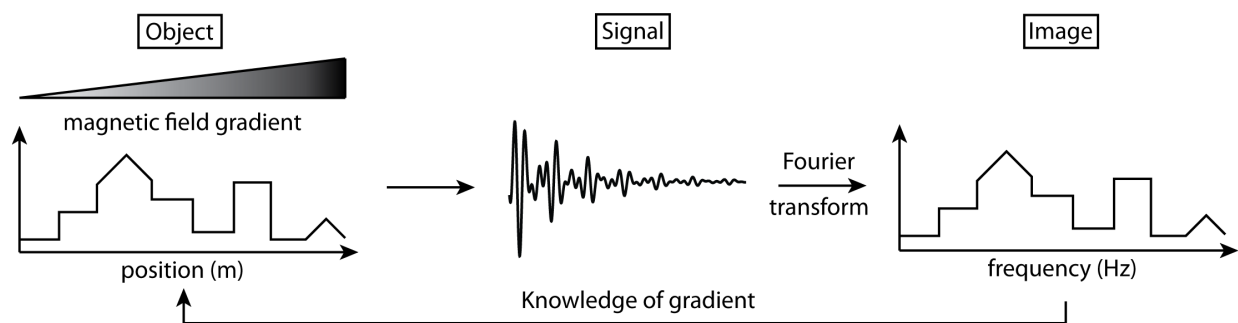
Figure 1.9: 1-dimensional MRI using frequency encoding.

$-\gamma(B_0 + G_x x))$, and the signal at each point in the object will exhibit a characteristic frequency which varies linearly with its coordinate along $\hat{x}$.

An illustration of this procedure is shown in Figure 1.9. The 1-dimensional image is formed just as we have described. An object is placed in a static magnetic field with an additional position-dependent gradient. The spins are excited into the transverse plane, and an NMR signal is collected, consisting of the sum of all signals from each spin. Since these signals now exhibit differing frequencies due to their location in the gradient, the Fourier transform of the signal will no longer yield a single peak at the Larmor frequency. Rather, the intensity of the signals found in the spectrum will directly reflect the quantity of spins precessing at each frequency, and will form a profile which recreates the shape of the object. Correlation of the observed frequency with the well-defined gradient will allow the image to be moved from frequency-space to position-space. This method of performing MRI is known as frequency encoding.

1.2.2 Phase Encoding & k-Space

Frequency encoding works extremely well for taking 1-dimensional profiles. While it is certainly possible to extend the technique to images in 2 or 3 dimensions (known as Projection-Reconstruction), this requires a wide sampling of gradient orientations and is far from a practical solution. A better way to approach this problem can be found with the technique of phase encoding.

Consider a function $m(x, y)$, describing the distribution of the nuclear spins. When excited to the transverse plane (and in the absence of inhomogeneities), this distribution will remain fixed in the rotating frame of reference. Under application of a gradient, the nuclear precession frequencies will change, acquiring an additional time- and position-dependent phase given by $\gamma G_x t_x x$, where G_x is a gradient along x, t_x is the duration of the gradient, and x is the position of the nuclei. Mathematically, the resulting signal can be written as $m(x, y) \exp(-i\gamma G_x t_x x)$.

At this point, we can define a new variable, $k_x = (\gamma/2\pi)G_x t_x$, which represents a "spatial frequency" dictated by the strength of the gradient and the duration of its application (or the area under the gradient waveform, as represented in an MRI pulse sequence). If we apply
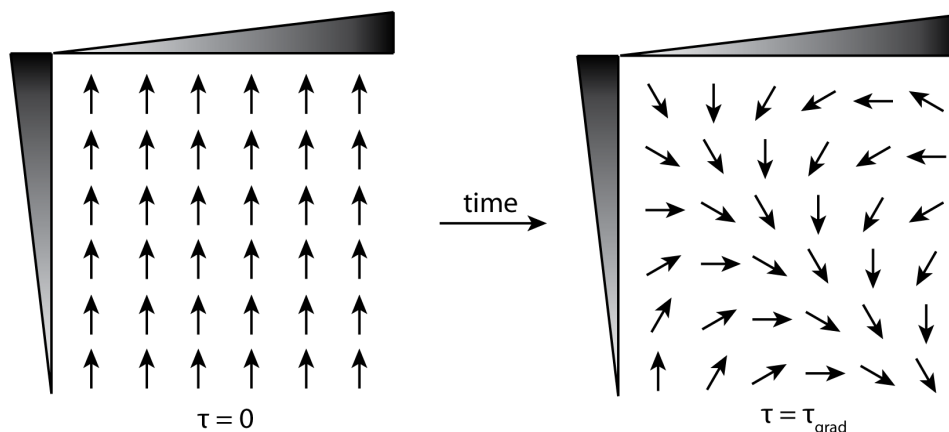
Figure 1.10: Effects of 2-dimensional phase encoding on magnetization vectors.

gradients along both $\hat{x}$ and $\hat{y}$, the resulting signal can be written as:

$$s(t) = \int_x \int_y m(x,y) e^{-i2\pi k_x x} e^{-i2\pi k_y y} dx \; dy \tag{1.30}$$

The physical effect of these gradients can be seen in Figure 1.10. The phase of each spin will be altered according to its position with respect to the two orthogonal gradients, creating a sort of "spin warping" effect on the magnetization vectors. While the consequences of this transformation may not be intuitively obvious, it's easy to see what we've done by looking at the signal equation.

The formula given in Equation 1.30 is, simply, a 2-dimensional Fourier transform between frequency-space (our signal, dependent on time), and "k-space" (our position-dependent spin encoding, dictated by spatial frequencies k_x and k_y). Because this is a Fourier relationship, the transform can be inverted, allowing us to recover our original spatially-dependent distribution of spins, $m(x,y)$. This procedure forms the basis of MRI in its most commonly used form.

While it would be fantastic to simply "measure" all points in k-space, it would require a continuous sampling of all available gradient strengths in all of the relevant dimensions. Therefore, the trick to MRI is to find the best way to sample a set of points in k-space such that you can invert your acquired signal data to retrieve an accurate representation of $m(x,y)$. There are countless ways to do this, but the experiments in this work depend only on two basic approaches.

The first of these is referred to as "pure phase encoding," and consists of sampling k-space in a point-by-point fashion. In other words, each experiment corresponds to a single point in k-space, reached by turning a set of gradients to specific strengths and durations to reach that particular point. The experiment is repeated across a multidimensional array (depending on the dimensionality of the image) of incremented gradient strengths, forming a rectangular grid within k-space (alternative sampling schemes are available, of course, but a grid is most common). This scheme is shown in Figure 1.11a, and is the only available imaging scheme in remote detection experiments. Because we need to perform one experiment for each point, pure phase encoding is a time-consuming process, and clever techniques such as compressed
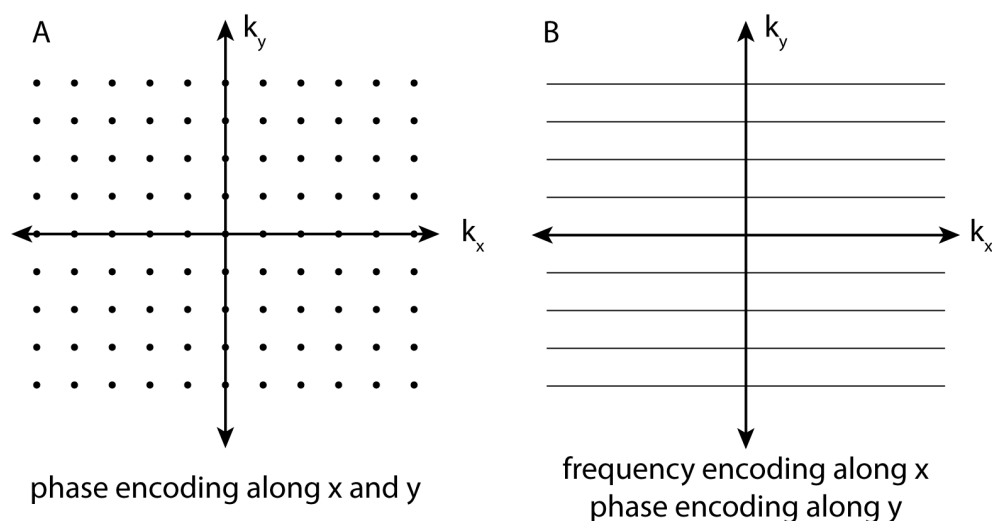
Figure 1.11: Relevant methods for sampling k-space.

sensing [89] have been applied to decrease the size of the acquisition without compromising much in terms of resolution (discussed further in Section 3.5).

A far more common option is to combine phase encoding with the sort of frequency encoding discussed above in the context of 1D images. In an N-dimensional experiment, we perform phase encoding for N-1 dimensions (by applying specifically calibrated gradients for a set amount of time to reach the relevant k-space point in those dimensions). During acquisition, we apply another gradient along the remaining dimension (often referred to as the readout gradient), allowing us to sample that dimension through the mechanism of frequency encoding. In a 2D image, the k-space sampling scheme looks like a set of parallel lines: one chooses a discrete position along one of the axes using phase encoding, and then travels parallel to the other axis by reading off the signal during continuous application of the frequency-encoding gradient. This is shown in Figure 1.11b for an image with phase encoding along k_y and frequency encoding along k_x. Since the frequency encoding can be accomplished during the time it takes to acquire your signal, experimental time is greatly decreased. However, the ease of performing high-resolution frequency encoding contrasts with the time consuming nature of phase encoding, often resulting in the choice of lower resolutions for the phase encoded dimensions.

1.2.3 Basic Imaging Sequences

The second method discussed forms the basis for two of the most common MRI imaging protocols, often referred to as spin echo and gradient echo sequences (shown in Figure 1.12). Spin-echo imaging is used in all of the directly detected current imaging experiments described in Chapter 2 due to its robust ability to cancel out imaging artifacts caused by inhomogeneities in the magnetic field. This is a natural consequence of the spin echo placed after the encoding step, as it will compensate for T_2^*-related effects. Gradient echo imaging relies upon a similar echo signal, but forgoes the 180° pulse and relies entirely on two read-out gradients of opposing polarity to trigger an echo (while there is no need to go into the
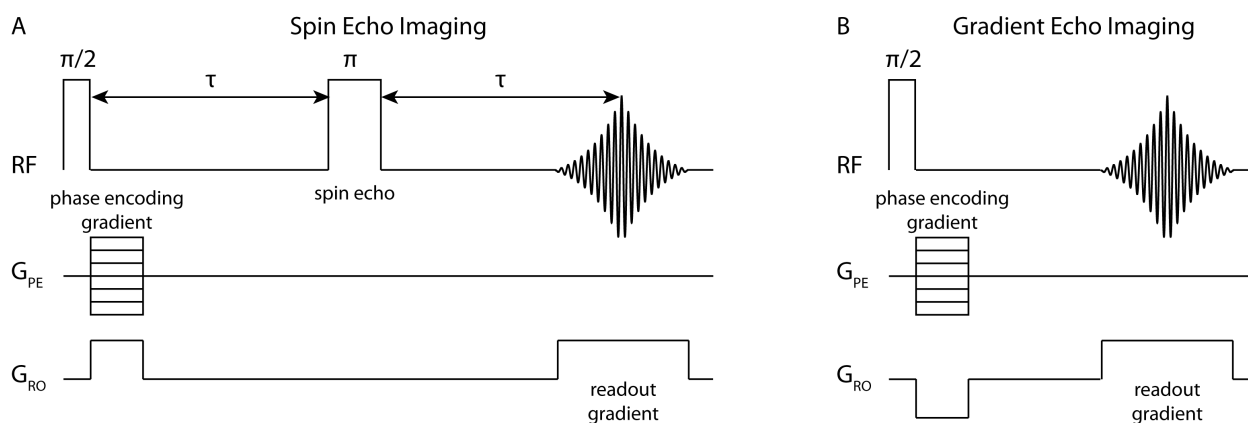
Figure 1.12: Pulse sequences for basic spin echo and gradient echo imaging experiments.

mechanism, the basic idea is that the flip in gradient strengths serves to flip the speeds of precession, in that "fast" spins now go slow and "slow" spins now go fast, allowing all of them to meet up once again and recapture the glory of their original signal).

The spin echo sequence actually creates a gradient echo on top of the spin echo, due to an initial application of the readout gradient during phase encoding. Unlike in the gradient echo sequence, this lobe is the same polarity as the later readout gradient, which is due to the fact that the 180° pulse refocuses the spin magnetization in a similar manner to the change in gradient sign (essentially, if this lobe were opposite the later readout, it would negate the effects of the spin echo). In the k-space picture, these lobes serve to move the starting point for the frequency encoding line away from the middle. Thus, for a k_x frequency encoding, the first lobe moves the starting point to $-k_{x,max}$ while the second takes it from $-k_{x,max}$ to $k_{x,max}$ during the readout, completing the desired line in k-space.

While the current detection experiments rely almost entirely on spin echo imaging (a precautionary measure due to the inhomogeneity-causing metal wire loop in the sample), the experiment is easily adaptable to gradient echo sequences which do not require the initial excitation of spins to be a complete 90° pulse, enabling small flip angle excitations and further decreasing experiment duration.

1.2.4 Resolution & Field-of-View

There are only a few more basic concepts that need to be covered in order to have the background for our later imaging experiments. The first of these focus on the determination of the resolution and Field-of-View (FOV) in an MRI experiment. As discussed above, there are two basic ways to sample k-space: phase encoding and frequency encoding. Since these methods sample the data in different ways, there are slight differences in how the imaging resolution and dimensions are calculated.

In phase encoding, we acquire k-space points individually, usually in a regularly sampled line or grid. It is an intuitive idea that the number of k-space points we sample will determine the number of imaging points we obtain, which therefore determines our resolution (increase the number of sampled points and you'll have an increase in the density of image points). To determine the resolution, however, we first need to know the spatial extent of our image,

i.e. the FOV.

Here, the Fourier relationship between frequency-space and k-space comes in handy. When taking a Fourier transform of a signal which has been sampled using a discrete set of points, the range in the conjugate transform dimension will always be given by the inverse of the time between each point. For instance, if we sample an NMR signal using 256 points with 100 ms spacing (also known as the dwell time), our resulting spectral width will be given by $1/(.1 \text{ s}) = 10$ Hz, with a resolution of 10 Hz/256 points $= .039$ Hz. For an image, our Fourier relationship is between k-space and frequency space, with the dwell time becoming the distance in k-space between two points, Δk_i (where i is the sampling axis). Thus, we can write:

$$\text{FOV}_i = \frac{1}{\Delta k_i} \tag{1.31}$$

Since $k_i = \frac{\gamma}{2\pi} G_i t_i$, we can write the FOV for both phase and frequency encoding scenarios. In phase encoding, t_i remains constant (call it τ), while G_i is incremented in steps of ΔG_i. In frequency encoding, $G_{ro,i}$ remains constant while discrete point are sampled at an interval Δt. Therefore:

$$\text{FOV}_i = \frac{1}{\Delta k_i} = \begin{cases} 1/(\frac{\gamma}{2\pi} G_{ro,i} \Delta t) & \text{frequency encoding} \\ 1/(\frac{\gamma}{2\pi} \Delta G_i \tau) & \text{phase encoding} \end{cases}$$

The corresponding resolutions are then given by $\delta_{pe} = \text{FOV}_i/N_{pe}$ (N_{pe} represents the number of phase encoding steps) and $\delta_{ro} = \text{FOV}_i/N_{ro}$ (N_{ro} represents the number of points sampled in the readout dimension).

1.2.5 Slice Selection

The last topic of interest is slice selection. While the pulse sequences drawn above use an initial "hard" 90° pulse, this can be replaced with a special shaped pulse designed to excite only a specific region of the sample. The general idea is straightforward. First, we apply an additional slice selection gradient along the axis of interest (almost always $\hat{z}$ in the experiments described here), which imposes a position-dependence upon the precession frequencies of spins in the transverse plane. Next, we replace our standard "hard" excitation with a shaped pulse which is designed to excite a specific range of frequencies, centered around its characteristic frequency offset.

The design of these pulses is not of significant importance to our discussion; typically, a sinc-function shaped pulse can be calibrated to excite a specific range of frequencies based on the pre-determined 90° pulse parameters. There are a few important parameters that relate the physical scale of the slice to the experimental parameters. We know that the gyromagnetic constant, γ, can be expressed in units of Hz/G. The slice selection gradient, G_{ss}, is in units of G/cm. The duration of the slice selection gradient, τ_{ss}, is also important (and, of course, in units of s). Simple dimensional analysis can be used to figure out the formula for Δz, the physical size of the slice (in cm):

$$\Delta z = \frac{1}{\frac{\gamma}{2\pi} G_{ss} \tau_{ss}} \tag{1.32}$$
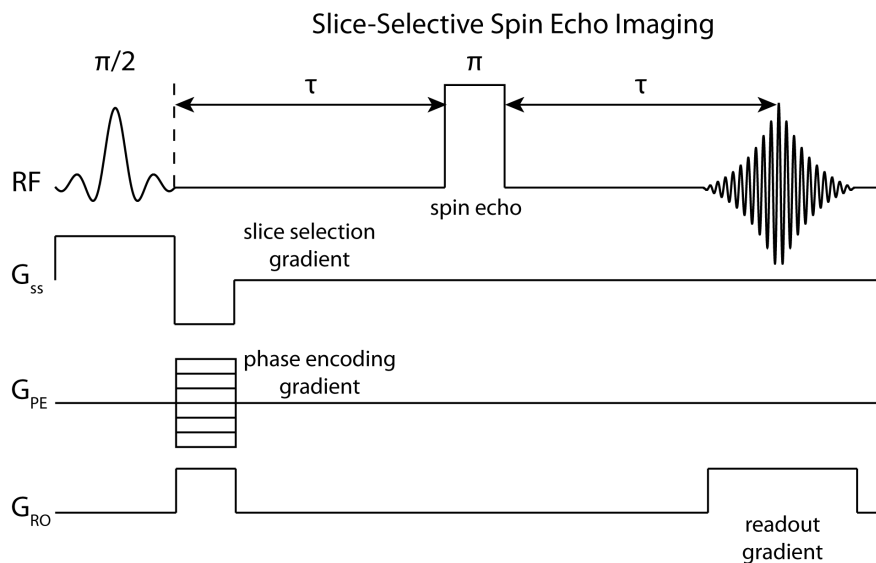
Figure 1.13: Slice-selective spin echo imaging sequence.

With these two elements in place (a position-dependent frequency and a way to excite only a select range of frequencies), we are able to perform slice-selective excitations. A slice-selective version of the spin echo imaging sequence is shown in Figure 1.13. As we will see later, slice selection is of particular use in "zooming in" to regions of interest (a procedure which is most useful in a remote detection experiment). One can excite only a specific slice of the sample and then narrow the imaging field-of-view to perform a high-resolution image on a smaller region with no compromise in resolution or experimental duration.

Chapter 2

Magnetic Resonance Imaging of Oscillating Electrical Currents

This chapter contains material previously published in reference [46], which has been reproduced here with the consent of its co-authors.

2.1 Background

2.1.1 Neuronal Currents

In some cases, including living neural tissue, moving electric charges within the sample produce oscillating magnetic fields that can be visualized by MRI methods. The imaging of current distributions by MRI has developed significantly over the last 20 years, with early applications based upon measuring the effects of externally applied current in order to image current density and conductivity within model systems [118][119] and *in vivo* [64][65][163]. However, the most active focus in recent current imaging studies is the possibility of directly imaging neuronal currents.

The human brain contains approximately 10^{11} neurons which link together to form 10^{14} connections (synapses), creating a massively interconnected signaling network. Neuronal currents arise during the signaling from one neuron to another, when neurotransmitters travel across the synaptic cleft and bind to the membrane of the postsynaptic neuron. Subsequent alterations in the membrane potential will cause specific ion channels to open or close, causing a net flow of ions (and therefore a current). While the currents generated by a single neuron are far too small to measure, detectable magnetic field changes on the order of $0.1 - 1$ nT [13] may result from synchronized postsynaptic currents in a large number of neurons.

The frequency of oscillatory neural activity is also extremely significant. In addition to the previously demonstrated significance of alpha waves (~ 10 Hz) in processes related to the visual cortex, memory, and attentiveness [69], a body of recent work has identified the importance of brain activity in the gamma and high gamma frequency ranges ($25 - 250$Hz) [104][81][53][31][20][62] to the synchronization of anatomically distant centers. Further, phase synchronization between neuronal activities operating across a range of frequencies may ultimately point to a global model of cognition, where brain function is coordinated across

numerous frequency regimes [103]. To date, most successful approaches to the mapping of γ-wave frequencies have involved the implantation of electrodes in direct contact with the brain, usually during a surgical procedure. Because of these experimental difficulties, the significance of these higher frequency brain waves remains poorly understood and a topic of very active debate. A non-invasive measurement of oscillating currents in the gamma frequency range is thus an important goal.

2.1.2 Existing Current Detection Methods

Functional MRI

Unlike optical methods for neuronal current monitoring [27], magnetic resonance is non-invasive and can be applied deep within optically opaque tissue. The development of functional Magnetic Resonance Imaging (fMRI) over the past 20 years has led to a rapidly expanding field of research in magnetic resonance neuroimaging, and fMRI has become an important tool of researchers and clinicians who seek to understand patterns of neuronal activation that accompany sensory and cognitive processes.

The fMRI technique is a relaxometry measurement based upon the modulation of water relaxation by oxygenated hemoglobin in regions of neuronal activity, known as blood-oxygen-level-dependant (BOLD) contrast [100]. Areas of neuronal activation typically exhibit an increased demand for oxygen, which is met by a subsequent rise in the levels of oxygenated hemoglobin carried within the blood flow to these regions. The difference in magnetic properties between oxygenated (diamagnetic) and deoxygenated (paramagnetic) hemoglobin has localized effects on the relaxation of nearby protons, causing an observable contrast in regions subject to a change in the relative proportion of oxygenated hemoglobin. Statistical methods are then employed to determine which regions display quantifiable evidence of BOLD contrast [165][160]. Because fMRI is built upon the imaging capabilities of MRI, it provides the same level of spatial information as the underlying MR image from which it is derived.

However, the interpretation of fMRI images rests on assumptions about the relationship between neuronal firing and hemodynamic response that are not firmly grounded in rigorous theory or experimental evidence. The hemodynamic response, which generates the BOLD contrast used to correlate an MRI observable to neuronal firing, evolves over a period that is two orders of magnitude longer than the underlying processes which are thought to cause it [96]. The interpretation of this effect depends on assumptions about its correlation with neuronal activity, a connection which quite often cannot be justified [86]. Signs of neuronal activation in a dead Atlantic salmon [10] point to the dangers of drawing conclusions from ill-founded statistical analyses, and recent experiments provide evidence of physiological mechanisms by which hemodynamic response is affected by mere anticipation of a stimulus, rather than the stimulus itself [127]. These concerns illustrate the strong need for a direct neuronal current detection modality, which could provide near real-time correlations between stimulus and neuronal response.

Electro- and Magneto-encephalography

Magnetoencephalography (MEG) and electroencephalography (EEG) provide an alternate means to monitor changes in neuronal activity, in which a network of sensors is placed
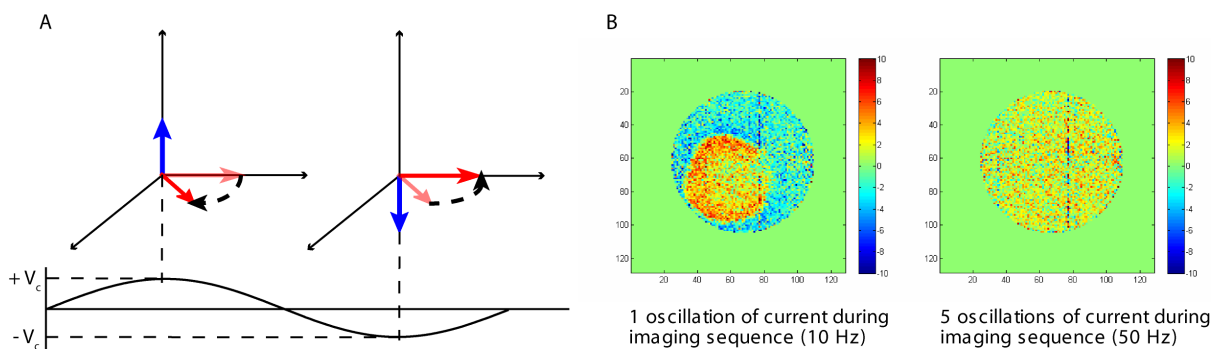
Figure 2.1: Illustration of a direct current detection approach relying on the accumulation of phase changes in the spin magnetization. In the case of an oscillating current source, the periodic nature of the current-induced magnetic field will cause reversal (and therefore cancellation) of the accrued phase every time the signal changes sign (a). An experimental demonstration of this is shown in (b), where a standard imaging sequence was carried out in the presence of an oscillating current-induced magnetic field within a loop of wire. At left, phase differences within the wire loop are clearly visible when a very slowly varying signal is used (one 100 ms cycle of a 10 Hz current), whereas, at right, we see complete cancellation of this effect when the number of current oscillations is increased (five 20 ms cycles of a 50 Hz current).

on the scalp (or directly on the surface of the brain) to measure electrical or magnetic fields in real time. For EEG, these sensors are simply a set of electrodes, while MEG is accomplished through the use of superconducting quantum interference devices (SQUIDs), which are very sensitive detectors of weak magnetic fields and require cryogenic containment.

However, the advantages in temporal resolution from these methods are offset by poor spatial localization due to the impossibility of inverting exterior field measurements to determine their source [55]. EEG and MEG are, therefore, unable to describe the internal structure of measured current sources, and are not well suited for answering questions requiring localized determination of neuronal activity. Furthermore, as the methods involve measurement on the scalp, the strength of the detectable magnetic fields will be significantly weaker than if their effects are encoded into spins within millimeters of the source, as in MRI. Concurrent fMRI and EEG measurements are possible with significant technical effort, although these yield images of neuronal processes with a resolution of only several millimeters per dimension [37][38], at least an order of magnitude worse than what is typically achievable using MRI. While these experiments remain worthwhile, it is not trivial to perform signal processing and draw correlations using techniques with opposing temporal and spatial regimes.

Direct Current Detection (Phase & Magnitude Contrast)

Due to these limitations, there has been a significant effort to develop a method to perform sensitive, high-resolution direct current imaging, with an emphasis on the detection of neuronal currents. These studies have primarily been proof-of-principle demonstrations

using artificial systems [13][14][66][70] and theoretical examinations of the feasibility of neuronal current detection [70][43][102][106][162][21]. While work is being done to develop a viable and broadly applicable detection modality for in vivo experiments [107][25][112][161], a number of studies [26][143][108][87] have cast doubt as to the feasibility of a technique based on traditional current imaging methods.

The most commonly used method for simulating these experiments *in vitro* relies upon application of a DC or slowly oscillating current during a conventional imaging sequence in a phantom. When the current-induced magnetic field is oriented parallel to the external field, it alters both the phase and the magnitude of nearby spins. Changes to the magnitude reflect a net spread in the phase of spins within an imaging voxel, while a phase change implies a coherent rotation of transverse magnetization. While some authors predict the phase effect to be stronger by up to two orders of magnitude [70][71], it is highly susceptible to cancellation effects due to spatially disordered structures, oscillating signals with a mean phase change of zero, incoherent signals, and location of the current source within a given imaging voxel [14][70]. Figure 2.1a illustrates the cause of this cancellation: as the current changes sign, the direction of spin precession is reversed, eliminating any accrued phase change. In Figure 2.1b, we see two phase imaging experiments using slowly (10 Hz, left) and rapidly (50 Hz, right) oscillating current signals. It is clear that the significant phase changes detected in the slowly oscillating signal are completely eliminated when the current frequency is increased. Other than a few specialized cases offering only a limited frequency range [120] or requiring careful synchronization of the pulse sequence to the current source [97][16], present applications of this technique cannot easily image oscillating fields with frequencies above ~ 10 Hz [74].

2.2 Resonant Current Detection

2.2.1 Previous Approaches

As has been shown previously [159], many issues related to cancellation of accumulated phase in phase contrast techniques can be resolved by using a rotating-frame resonant mechanism, termed stimulus-induced rotary saturation (SIRS), to generate current-induced contrast. SIRS builds upon earlier work by Kraus et al. [73][74] involving resonant current detection at ultra-low magnetic fields. In these experiments, a pre-polarized sample is simultaneously placed in an ultra-low measurement field ($1 - 100$ μT, giving $\omega_H = 40 - 4000$Hz) and an orthogonal current-induced magnetic field designed to mimic the oscillating fields of interest. When the current frequency is matched to the proton Larmor frequency (which is in the audio-frequency range, due to the ultra-low magnetic field), nearby spins undergo a detectable rotation around the orthogonal axis of the current-induced field. The strength of the ultra-low measurement field can be adjusted within the previously specified range in order to choose which frequency of current will cause the resonant rotation. For higher sensitivity at low magnetic fields, the dynamics were observed using a superconducting quantum interference device (SQUID). While this method has several advantages, including applicability at low-field and compatibility with oscillating zero-mean fields, it requires a cryogenically cooled SQUID for detection (along with additional pre-polarization hardware) and suffers

from the sensitivity challenges associated with low-field imaging [22][23]. In contrast, the SIRS method exploits an analogous rotating frame resonance condition by matching the power of an applied spin lock field to the frequency of oscillating currents (a detailed explanation of resonant mechanisms can be found in Section 2.2.2). This method should be applicable at high field and is compatible with conventional clinical MRI hardware. However, in practice, experimental imperfections and non-idealities in biological current sources compromise its robustness.

Here, we demonstrate that, in addition to its advantages over phase and magnitude imaging, current imaging through a resonant mechanism permits spectroscopic control over the contrast mechanism. Spectroscopic control exercised through modulation of the spin lock fields allows us to compensate for non-idealities in the experimental hardware or the current sources by producing inhomogeneity-compensated and band-selective variants of the experiment, essential for imaging biological sources with multiple constituent frequencies. Next, we introduce a Fourier imaging experiment in which the spatial variation of the magnetic field can be readily measured. Finally, after confirming the limit of detectable field strength to be on the level of synchronized neuronal activity, we perform a remotely-detected analogue
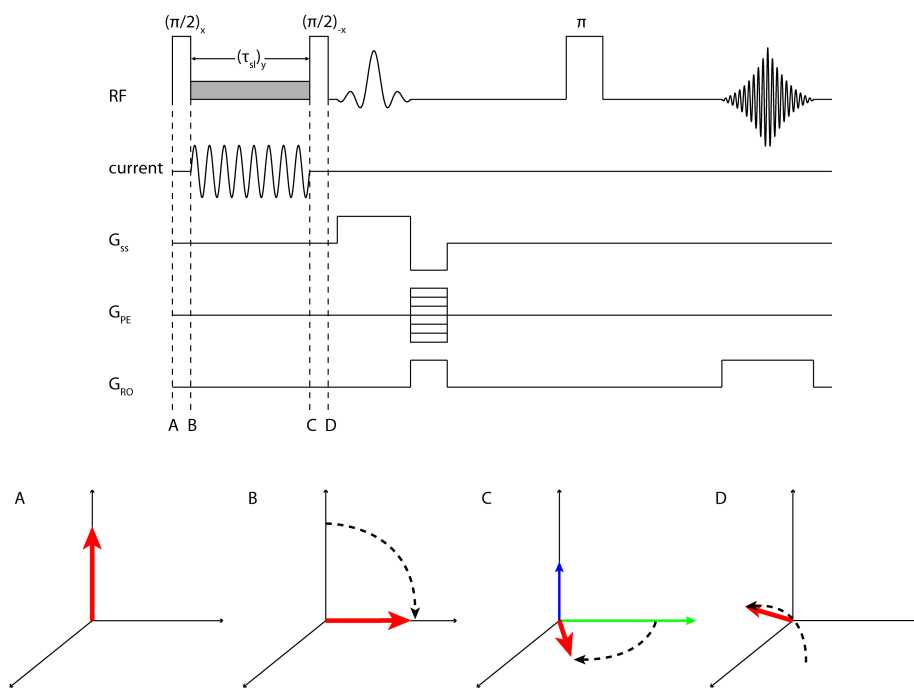
Figure 2.2: Conventional spin-echo imaging sequence combined with preceding spin lock module, application of current, and storage pulse. Corresponding vector diagrams of the magnetization in the doubly rotating frame are shown below, with the spin lock indicated in green, the audio-frequency magnetic field in blue, and the magnetization in red. The initial magnetization aligned along the static field (a) is flipped into the transverse plane by a $\pi/2_x$ pulse (b), where it proceeds to rotate around the audio field for a time τ_{sl} during application of the resonant spin lock (c). Afterwards, a second $\pi/2_{-x}$ pulse projects and stores the y-magnetization along (d) in preparation for the imaging sequence.

| Rotate onto y-axis | Current encoding time | Storage of y-component | Initial conditions for imaging |
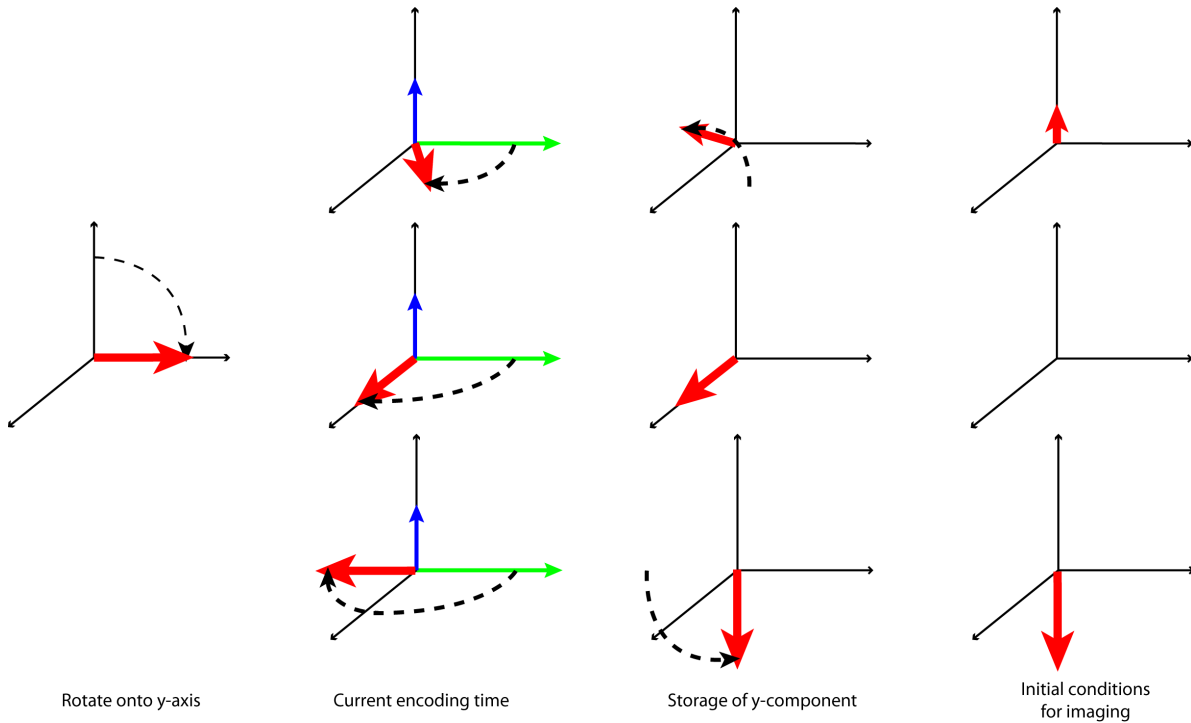
Figure 2.3: Vector diagrams of the spin magnetization in the doubly rotating frame, showing magnetization trajectories for three different current encoding durations. Here, the magnetization is shown in red, the spin lock in green, and the audio-frequency magnetic field in blue.

of the experiment (*vide infra*), in which we achieve high sensitivity and spatial resolution by using an optimized remote detector of magnetic resonance.

2.2.2 Resonant Mechanism & Pulse Sequence

A typical current imaging pulse sequence is shown in Figure 2.2. An initial $\pi/2_x$ pulse is applied, aligning the magnetization along $\hat{y}$ where it is then held via application of a spin lock modulated at the proton Larmor frequency with power B_{sl} and duration τ_{sl}. When viewed in the rotating frame, the spin lock field remains aligned along $\hat{y}$, with magnitude B_{sl} (2.35 μT for $B_{sl} = -\gamma B_{sl} = 100$ Hz). Simultaneous application of an audio frequency current will generate an oscillating magnetic field along $\hat{z}$. When $\omega_c \approx \omega_{sl}$, the resonant component of the audio field induces a rotation of M_y around $\hat{z}$. After τ_{sl}, a $\pi/2_{-x}$ pulse is applied to store M_y along $\hat{z}$, after which a conventional spin-echo imaging sequence is carried out. A two-step phase cycle of the $\pi/2$ pulses and the spin lock was employed to cancel out effects of any residual transverse magnetization after the spin lock.

The result of this rotation is illustrated in Figure 2.3 for three different current-encoding intervals. In the top case, the magnetization vector is rotated to a position between $\hat{x}$ and $\hat{y}$, which, following storage of M_y along $\hat{z}$, will give a decreased initial magnetization at the start of the imaging sequence. In the second case, the rotation is stopped when the magnetization has reached $\hat{x}$, yielding no y-component and thus a completely depleted initial
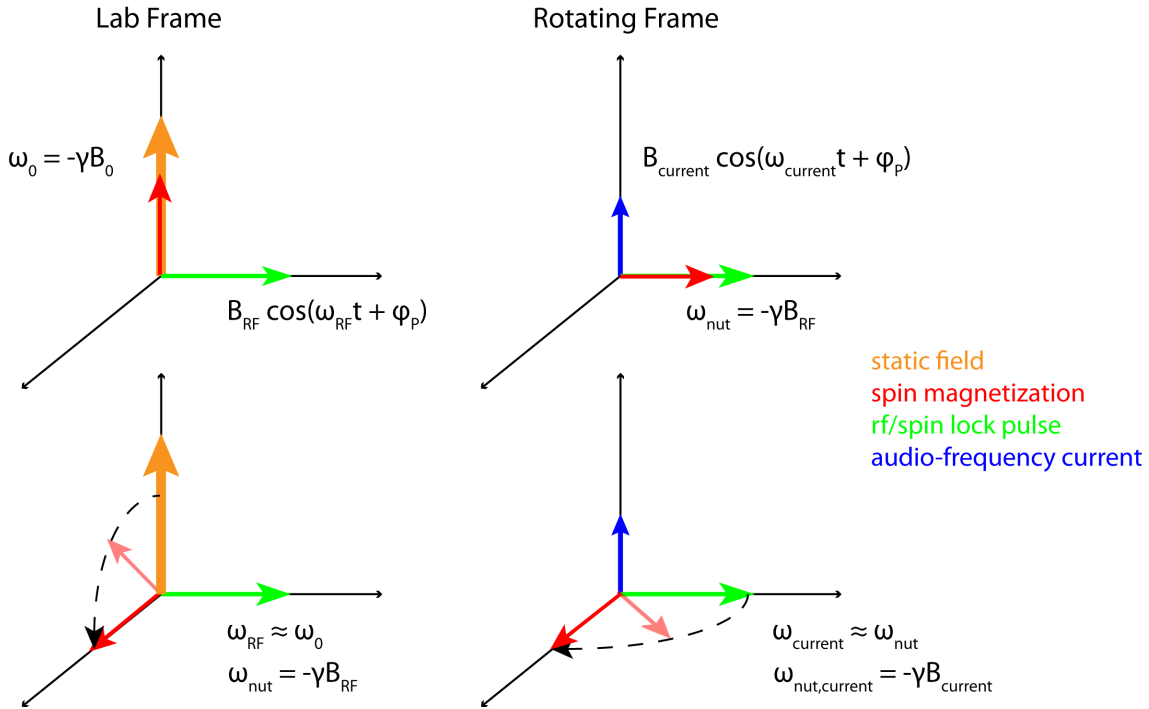
Figure 2.4: Analogy between a standard radiofrequency pulse applied in the lab frame and a resonant current-induced pulse applied in the spin-locked rotating frame. Once we have transformed into the doubly rotating frame of reference, these two scenarios are identical after a rotation of the coordinate system.

magnetization along $\hat{z}$. Finally, if the magnetization proceeds to $-\hat{y}$, storage of M_y will give a negative maximum (although still smaller than the initial equilibrium magnetization due to relaxation during the rotation). The oscillatory behavior of the stored magnetization provides an additional means to characterize the strength of the current-induced magnetic field, as discussed below.

When viewed in a frame of reference rotating both around $\hat{z}$ at the Larmor frequency and around $\hat{y}$ at the spin lock frequency, the situation is analogous to the application of a normal pulse (the current-induced field, in our case) to magnetization aligned with a static field (here, the spin lock). A comparison of these two situations is one of the best ways to understand the rotating frame saturation effect, and is shown in Figure 2.4. For a traditional pulse applied in the lab frame (left side), we start with our spins at equilibrium along $\hat{z}$, aligned with a static field with characteristic (Larmor) frequency $\omega_0 = -\gamma B_0$. Application of a pulse with the form $B_{RF} \cos(\omega_{RF} t + \phi_P)\hat{y}$ will cause a rotation of magnetization in the xz plane when $\omega_0 \approx \omega_{RF}$. The frequency of this rotation is dictated by the strength of the pulse, and is referred to as the nutation frequency (where $\omega_{nut} = -\gamma B_{RF}$). If we then move into the (doubly) rotating frame of reference (right side), we can remove the static field from our diagram and our resonant pulse becomes static along $\hat{y}$ ($B_{RF} \cos(\omega_{RF} t + \varphi_P)\hat{y} \rightarrow B_{RF}\hat{y}$). The resonant rotation begins once the spins are aligned with the spin lock along $\hat{y}$ and an audio-frequency oscillating magnetic field is applied along $\hat{z}$. At this point, it is easy to see that this vector diagram is identical to a typical pulse in the lab frame with a 90°

rotation of the coordinate system. Therefore, when the characteristic frequency of the spin lock pulse ($\omega_{nut} = -\gamma B_{RF}$) matches the frequency of the current-induced magnetic field along $\hat{z}$, the spin magnetization rotates about the "pulse" in the xy plane, with frequency $\omega_{nut,current} = -\gamma B_{current}$. The spin dynamics of this rotation are further discussed in Section 2.2.3.

Resonant rotations of spin magnetization will be initiated by components of the current-induced field which are aligned along $\hat{z}$. The method will be nearly insensitive for other components of the current-induced magnetization, complicating retrieval of the true field distribution in cases where this is of interest.

2.2.3 Spin Dynamics for Resonant Current Detection

A more detailed explanation of the current detection experiment can be found by examining the equations governing spin dynamics in the presence of a spin lock and resonant current-induced magnetic field. The Bloch equations are well suited to model this type of experiment, and can be solved numerically in Matlab once all of the magnetic fields and initial conditions have been defined. For simplicity, the following equations and simulations are shown in the standard rotating frame of reference (to remove the effects of Larmor rotation). As has been previously discussed, the Bloch equations (neglecting the effects of relaxation) are given by:

$$\frac{d\mathbf{M}(t)}{dt} = \gamma \mathbf{M}(t) \times \mathbf{B}(t) \tag{2.1}$$

When moving from the laboratory frame to the rotating frame (see Section 1.1.8), we are able to remove any terms involving $B_0\hat{z}$, and all pulses applied at the resonant frequency can be represented as stationary components along their respective axes (i.e. $B_1 \sin(\omega_0 t)\hat{y} \to B_1\hat{y}$, where $\omega_0 = -\gamma B_0$). In a current detection experiment with an oscillating current-induced magnetic field along $\hat{z}$ and a spin lock applied along $\hat{y}$, $\mathbf{B}(t)$ is given by:

$$B_x(t) = 0 \tag{2.2}$$
$$B_y(t) = B_{sl} \tag{2.3}$$
$$B_z(t) = B_c \cos(\omega_c t) \tag{2.4}$$

For the resonant saturation experiment described above, the initial magnetization vector $\mathbf{M}_i(t)$ is given as M_y, meaning that the spin magnetization is aligned with the spin lock along $\hat{y}$ following the initial $\pi/2$ pulse. The traditional way to calculate the effect of a resonant pulse on orthogonal spin magnetization is to separate the pulse (in this case, the oscillating current along $\hat{z}$) into two counter-rotating components in the plane orthogonal to the magnetization (here, xz), as discussed earlier in Section 1.1.7:

$$B_c \sin(\omega_c t)\hat{z} = \begin{cases} \frac{1}{2}B_c(\sin(\omega_c t)\hat{x} + \cos(\omega_c t)\hat{z}) & \text{resonant} \\ \frac{1}{2}B_c(-\sin(\omega_c t)\hat{x} + \cos(\omega_c t)\hat{z}) & \text{non-resonant} \end{cases}$$

In most situations, only the first of these two components is capable of generating a significant rotation of the spin magnetization, and the non-resonant component may be safely ignored (known as the Rotating Wave Approximation). Rotations will occur once the
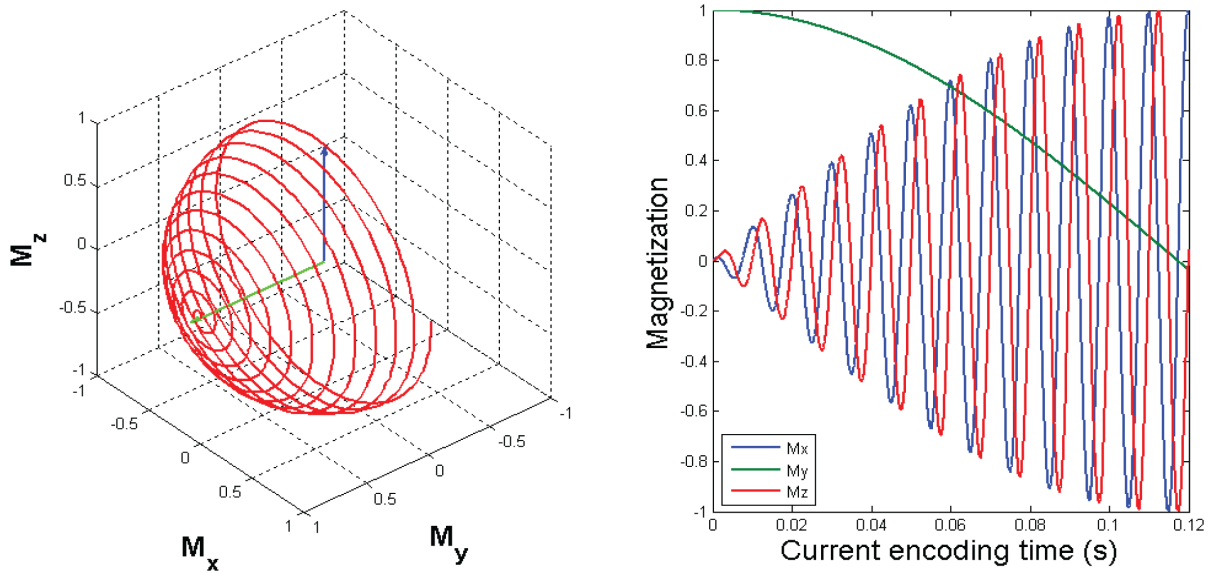
Figure 2.5: Simulated spin dynamics during resonant current rotation. The 3-dimensional trajectory of an initial M_y spin vector is shown in the rotating frame (a), with red indicating the spin magnetization, green indicating the spin lock, and blue indicating the oscillating current-induced magnetic field. In (b), we see the values for each magnetization component during the trajectory shown in (a). For this simulation, $\tau_{sl} = 120$ ms and $\omega_c = 100$ Hz, with a current-induced field strength of 100 nT.

resonance condition is met, which is that $\omega_c \approx -\gamma B_{sl}$. Plugging the resonant component into the Bloch equations, with initial magnetization M_y, gives:

$$\frac{d\mathbf{M}(t)}{dt} = \gamma(M_y\hat{y}) \times \left\{ \frac{1}{2}B_c \sin(\omega_c t)\hat{x} + B_{sl}\hat{y} + \frac{1}{2}B_c \cos(\omega_c t)\hat{z} \right\} \tag{2.5}$$

$$\frac{dM_x(t)}{dt} = \gamma \left[\frac{1}{2}M_y B_c \cos(\omega_c t) - M_z B_{sl} \right] \tag{2.6}$$

$$\frac{dM_y(t)}{dt} = -\gamma \left[\frac{1}{2}M_x B_c \cos(\omega_c t) - \frac{1}{2}M_z B_c \sin(\omega_c t) \right] \tag{2.7}$$

$$\frac{dM_z(t)}{dt} = \gamma \left[M_x B_{sl} - \frac{1}{2}M_y B_c \sin(\omega_c t) \right] \tag{2.8}$$

These coupled differential equations can be readily solved using numerical integration in Matlab. The dynamics of the spin magnetization vector are illustrated in Figure 2.5a (using parameters $\omega_c = 100$ Hz, $B_c = 100$ nT, and $\tau_{sl} = 120$ ms), with the spin lock in green, current-induced magnetic field in blue, and spin trajectory in red. A plot showing the behavior of each component of the magnetization is shown in Figure 2.5b. From the plots, it is clear that two separate rotations are taking place (at different frequencies). The first of these is the resonant rotation around the current-induced field, which serves to rotate the y-component of the spin magnetization from $\hat{y}$ to $\hat{x}$ over the course of 120 ms. The second
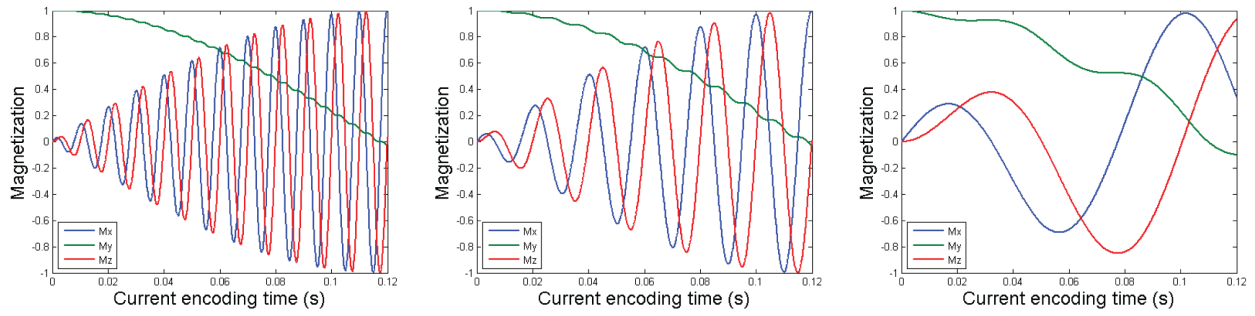
Figure 2.6: Simulated spin dynamics for resonant current detection, without the Rotating Wave Approximation. The trajectories of the magnetization components are shown for $\omega_c = 100$ Hz, 50 Hz, and 10 Hz.

is a rotation around the spin lock itself, which occurs at higher frequency (because the spin lock field is stronger than the current-induced field by an order of magnitude). However, while M_x and M_z oscillate at the product of these frequencies, M_y only varies at a frequency dictated by the strength of the current-induced field. Thus, storage of this component for imaging will generate an oscillation in signal intensity with frequency directly proportional to the current-induced field strength at each voxel in the image.

Finally, it should be noted that it is not always appropriate to neglect the off-resonant component of the current-induced magnetic field. As the frequency of the current (ω_c) is decreased, the strength of the spin lock pulse at resonance (where $\omega_c \approx \omega_{sl}$) will also need to be decreased, since $\omega_{sl} = -\gamma B_{sl}$. Therefore, at very low frequencies of current the resonant spin lock becomes quite weak. As discussed by Abragam [2], the Rotating Wave Approximation breaks down in situations where B_c/B_{sl} is no longer small. As a result, the counter-rotating non-resonant component of the oscillating field must be considered, typically leading to a change in resonance frequency known as the Bloch-Siegert shift [12].

This effect should certainly be considered when dealing with current frequencies lower than 50 Hz. The Bloch equations can be easily modified to incorporate the non-resonant component, simply by replacing the resonant field rotating in xz with the original form of $B_c \cos(\omega_c t)\hat{z}$:

$$\frac{d\mathbf{M}(t)}{dt} = \gamma(M_y\hat{y}) \times \{B_{sl}\hat{y} + B_c \cos(\omega_c t)\hat{z}\} \tag{2.9}$$

$$\frac{dM_x(t)}{dt} = \gamma\left[M_y B_c \cos(\omega_c t) - M_z B_{sl}\right] \tag{2.10}$$

$$\frac{dM_y(t)}{dt} = -\gamma\left[M_x B_c \cos(\omega_c t)\right] \tag{2.11}$$

$$\frac{dM_z(t)}{dt} = \gamma\left[M_x B_{sl}\right] \tag{2.12}$$

The results of this effect on the spin dynamics are shown in Figure 2.6 for $\omega_c = 100$ Hz, 50 Hz, and 10 Hz. From these trajectories, one can clearly see that as ω_c, and therefore B_c, decrease, the secondary oscillations caused by rotation around the spin lock diminish in frequency and M_y is no longer completely independent from these oscillations (as previously

seen in Figure 2.5). However, while the spin lock frequency has an increasingly noticeable effect on M_y, the rotation we are interested in (around the audio-frequency current-induced field) remain, and the value of M_y at the end of the period of rotation remains the same as that obtained at higher frequencies. So, while the resonant rotation is still valid at low ω_c, it should be noted that the stored intensity from M_y will exhibit periodic variations from the expected value which will become more noticeable at low B_{sl}, as this oscillation decreases in frequency and increases in magnitude.

The weak spin lock field at low B_{sl} will also result in characteristic image artifacts related to pulse imperfections and RF inhomogeneity. This behavior can be easily fixed by adding additional phase-compensated pulses to the spin lock, as discussed in Section 2.4.3.

2.3 Materials & Methods

2.3.1 Direct Current Imaging

Direct imaging experiments were performed using Paravision 4.0 and Topspin 1.3 on a 7.05 T Oxford Instruments magnet using a Bruker AVANCE 300 (Bruker, Billerica, MA) spectrometer. Images were taken with a Bruker MIC 300S1/AS microimaging probe.

The imaging sequence (Figure 2.2) consists of a spin lock module and simultaneous pulsed current preceding acquisition of each line of k-space. After rotation of the magnetization into the transverse plane, the spin lock was applied with intensity resonant with the frequency of a simultaneously applied current pulse. Following this interval, the M_y component was stored along $\hat{z}$, and slice-selective spin-echo imaging was used. Variations on the spin lock and storage pulse are described elsewhere within the chapter. A two-step 180° phase cycle of the $\pi/2$ pulses and the spin lock was employed to cancel out effects of any residual transverse magnetization after the spin lock. 2D images in the plane of the loops and 3D images were obtained in $\sim 1 - 1.5$ minutes and ~ 40 minutes per experiment, respectively, and used a spin-echo imaging sequence with resolutions of 128×64 and $128 \times 64 \times 32$ and a FOV of 12 mm in each dimension. The spin-echo imaging sequence was chosen to minimize artifacts from the copper loop, although a gradient echo version also generates satisfactory images at resonance and would be a suitable choice in biological samples and when factors such as experiment duration or power deposition are a matter of concern.

2.3.2 Apparatus

Current imaging phantoms consisted of 28-guage insulated wire immersed in a solution of deionized water (diluted to 20% in D2O and paramagnetically doped to decrease relaxation times) within a 10 mm glass NMR tube. Photographs of the single (a) and double (b) loop phantoms are shown in Figure 2.7. The wire loops in both single- and double-loop phantoms had ~ 6.5 mm diameter, and were oriented perpendicular to B_0 in order to create magnetization along $\hat{z}$. In the double-loop phantom, the two loops were positioned coaxially along $\hat{z}$ with ~ 6.5 mm vertical spacing. The single loop phantom has a red circular plastic spacer placed above the solution to aid in centering the current source. Since insulated wire was used, there was no galvanic electrical contact with the solution. Current
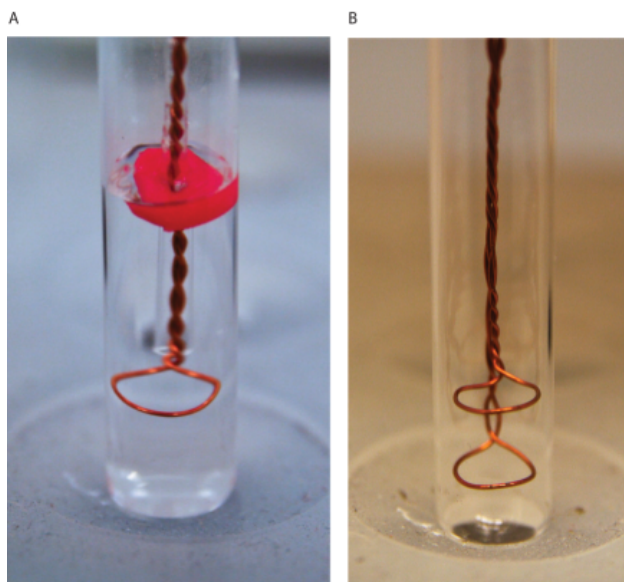
Figure 2.7: Wire loops used for both single- (a) and double-loop (b) direct current detection experiments. All loops had diameters of ~ 6.5 mm, and were coaxially oriented with respect to the longitudinal axis, such that the resulting current-induced magnetic field would lie primarily along $\hat{z}$.

pulses were produced using DS345 (Stanford Research Systems, Sunnyvale, CA) and 3314A (Hewlett Packard, Palo Alto, CA) function generators synchronized via TTL input triggered within the pulse sequence. TTL-triggered multi-tone signals were generated using a National Instruments USB-6215 DAQ and SignalExpress 3.0 (National Instruments, Austin, TX). For experiments involving very small current signals, precalibrated attenuators (Mini-Circuits, Brooklyn, NY) were used to output the desired voltage.

2.3.3 Remote Current Imaging

Remote experiments were performed using VnmrJ on an Oxford Instruments 7.05 T wide-bore magnet and a Varian imaging console. Excitation, spin lock, and storage pulses were performed with a 40mm Varian volume imaging probe, while gradients were applied using a Varian triple-axis gradient system producing up to 100 G/cm on all three axes. The detection probe was a custom-built microcoil probe connected to the capillary tubing via commercially available connectors (Upchurch Scientific, Oak Harbor, WA). Water flowed through the system at a constant pressure of ~ 10 psi, driven by a nitrogen gas ballast system and regulated by a proportional control system (Omega Engineering, Stamford, CT).

For more detailed information on pulse sequences for remote detection, please refer to Chapter 3. Briefly, the remote detection experiment consists of spatially separated encoding and detection steps. The pulse sequence, shown in Figure 2.8, begins with an excitation into the transverse plane, which can be made slice selective by the simultaneous application of a refocused gradient along $\hat{z}$ during shaped sinc excitation and storage pulses. Once the magnetization has reached the transverse plane, a collinear spin lock is applied along with a synchronously triggered current pulse to generate the resonant effect. Bipolar velocity-
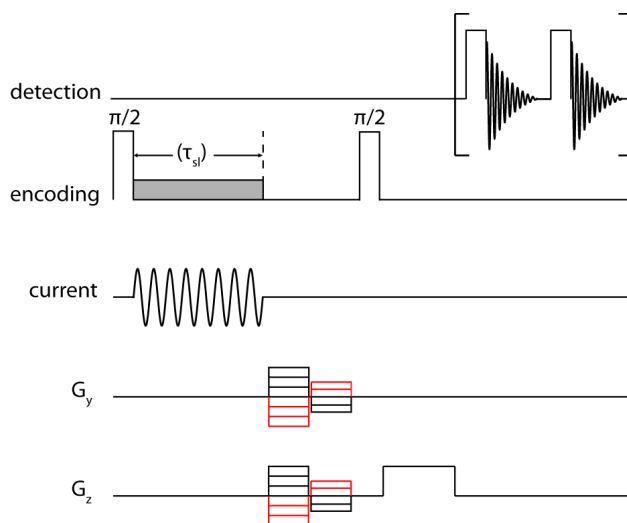
Figure 2.8: Pulse sequence for remote current detection experiments. Flowing spins are first rotated into the transverse plane with the initial 90° excitation (which can be made slice selective with a gradient along $\hat{z}$). Current encoding takes place immediately afterwards through the simultaneous application of an oscillating electrical current and resonant spin lock pulse. Imaging points in k-space are then sampled via phase encoding along multiple axes, and a second 90° pulse stores the magnetization along $\hat{z}$ for travel to the detector. The current- and phase-encoded data are then read out stroboscopically within the microcoil, adding an additional time-of-flight dimension to the data.

compensated phase encoding is performed along two axes, followed by a storage pulse to return the encoded magnetization components to the longitudinal axis for travel to the detection coil. The stored magnetization is read off stroboscopically within the microcoil by a series of $\pi/2$ pulses, yielding an additional time-of-flight dimension. Phase contrast was generated by comparison with a control image where TTL triggering of the current burst had been disabled. Current and control experiments were interleaved with respect to collection of points in k-space. While remote detection sequences typically contain an echo pulse in the center of the encoding section (to rephase magnetization at the time of storage), it was omitted here due to the difficulties in finding a phase cycle which does not also cancel the accrued phase from the current-induced rotation. Instead, a simplified four-step phase cycle of the storage pulse and receiver phase was employed, which stores both components of the encoded magnetization while removing artifacts caused by excitation of spins outside the encoding region (the storage pulse and receiver were kept 180° out of phase, and incremented by 90° at each step with all other pulses maintaining constant phase). Images were taken with 45×45 resolution, with no signal averaging beyond the phase cycle.

2.3.4 Data Processing

Data were processed using Matlab 7.7.0 (Mathworks, Natick, MA). For clarity in displaying the 2D current loop images, voxels outside of the sample volume were suppressed by creating a mask from the control image in which voxels with signal intensity lower than

a specified percentage of the maximum voxel intensity were set to zero. 3D images were apodized with Gaussian functions along all three dimensions, and contours plotted at saturation levels of 30%, 50%, 70%, and 90% (increasing in opacity) with respect to a control. In order to generate the field map, the frequency spectrum in each voxel was calculated by Fourier transformation of the oscillating signal after subtracting a best-fit exponential curve in order to eliminate the peak at zero frequency due to relaxation-based decay. The field strength was then calculated by determining the weighted mean of the frequency spectrum. The remote image data were zero-filled by a factor of two and apodized along both phase encoding dimensions. The direct dimension of each time-of-flight acquisition was Fourier transformed and then summed across the peak prior to 2D Fourier transformation of the phase encoding dimensions (for more detail on data processing for remote detection experiments, please refer to Section 3.4). Phase images were plotted by masking out voxels with intensity less than the maximum intensity multiplied by a cutoff value and determining the relative phase of each voxel between the current image and the control.

2.4 Results

2.4.1 Resonance Spectra & Images

In order to fulfill the resonance condition, one must match the spin lock frequency ($\omega_{sl} = -\gamma B_{sl}$) to the current frequency (ω_c). While this is not a difficult task, it is not as straightforward as one might expect, as pulse powers are measured in decibels on NMR spectrometers and the definition of these scales varies between Varian and Bruker instruments. To this end, a simple calibration experiment can be performed to find the resonant spin lock power. By holding the current frequency fixed and sweeping the power of the spin lock, one can observe a noticeable change in the NMR spectra at the point of resonance. Therefore, the experiment consists of a spin lock/current encoding period (τ_{sl}), directly followed by acquisition of the NMR spectrum. Once an array of spectra have been taken at different spin lock powers, the peaks are integrated and plotted according to spin lock power, as shown in Figure 2.9. This plot clearly indicates the point of maximum resonance at 100 Hz, and displays ~ 10 Hz width at half maximum. Because these spectra contain signal from the entire sample, the degree of the observed resonant effect will be much weaker than for the voxels nearest to the current source. While one might expect to observe oscillatory modulation of the dip amplitude (in keeping with the behavior under rotation described earlier), this is typically not the case, as the majority of the signal depletion comes from increased relaxation when the magnetization is rotated away from the spin lock.

Two-dimensional axial images at 100 Hz were obtained using the modified spin-echo imaging sequence described above, and are shown in Figure 2.10. As discussed earlier, the current imaging experiment consists of a resonant current encoding module preceding a conventional spin echo imaging sequence. Following the resonant rotation and storage of M_y, spins will exhibit initial intensities which differ from their equilibrium values. Thus, the rotary resonance effect will manifest as dark regions within the image, which exhibit characteristic oscillation frequencies that vary spatially throughout the sample with the strength of the current-induced magnetic field. Since only the magnitude of M_y is stored
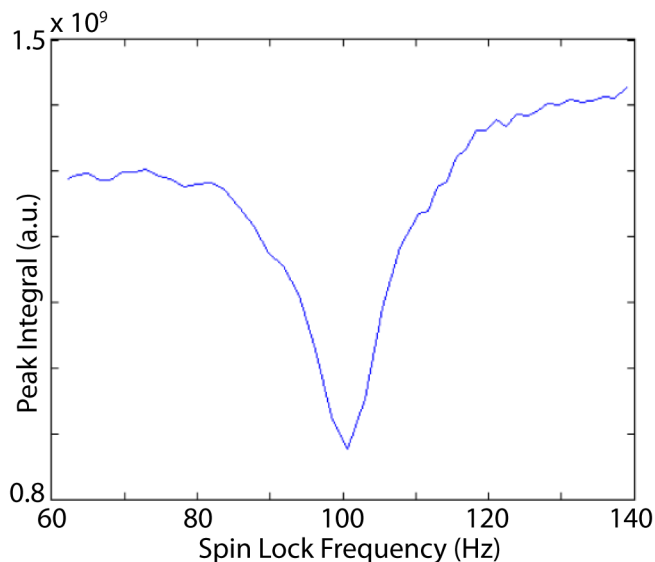
Figure 2.9: Integrated peak area during a sweep of the spin lock power across resonance with an audio-frequency magnetic field ($\tau_{sl} = 100$ ms, $\omega_c = 100$ Hz, $V_{current} \sim 800$ μV).

after the spin lock period, the images shown rely on detection of changes in magnitude rather than phase. Phase-sensitive images can easily be reconstructed if a complementary experiment is performed to store the M_x component.

Next, we collected a series of rotary resonance images as a function of the spin lock duration, illustrating the oscillatory behavior of the transverse magnetization within each imaging voxel, as shown in Figure 2.11a. Because the imaging sequence only measures the magnitude of the initial intensity, the voxel intensities are all positive, and the appropriate mathematical expression for this oscillation is an oscillating component, $\cos^2(-\gamma B_c t)$, multiplied by a decaying exponential representing the damping due to rotating frame relaxation, $e^{-t/T_{1\rho}}$. In Figure 2.11b, we applied Fourier analysis to determine the average current frequency driving the oscillation, which allows for direct calculation of current-induced magnetic field strength throughout the sample. Fourier transformation of a $\cos^2$ function will yield identical peaks
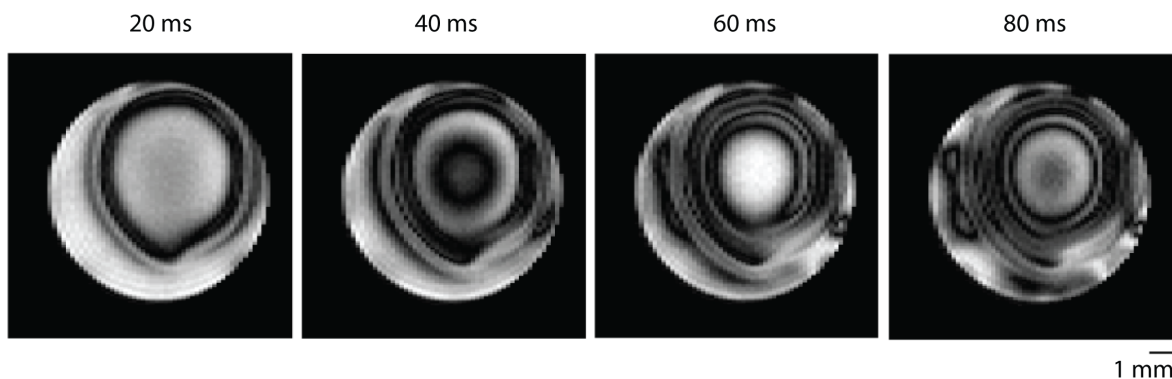
Figure 2.10: 2D images with $\omega_c = 100$ Hz, and $V_{current} \sim 1.5$ mV, at $\tau_{sl} = 20$ ms, 40 ms, 60 ms, and 80 ms.
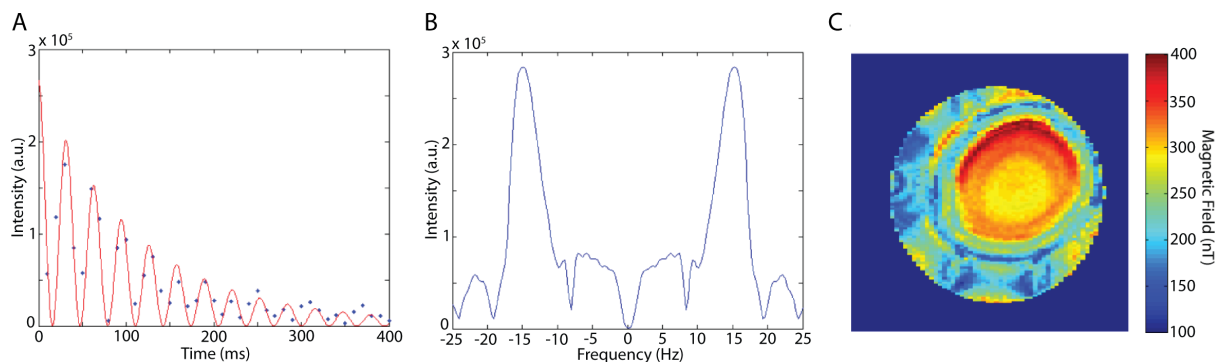
Figure 2.11: Data from a τ_{sl}-incremented series of images with $\omega_c = 100$ Hz and $V_{current} \sim$ 1.5 mV. The magnitude of a voxel in the center of the current loop is shown in (a) with an overlaid fit of a $\cos^2$-modulated exponential decay that would simulate the projection of the y-component of an oscillating transverse magnetization. Fourier transformation of these data (after correcting for the relaxation decay) (b) reveals an average oscillation frequency of ~ 12.8 Hz in the center of the loop, corresponding to a field strength of ~ 300 nT at this voltage. Plotting the magnetic field given by the average frequency in each voxel yields a map of the field strength throughout the slice (c).

at both positive and negative frequencies, so the average frequency can be determined by calculating the weighted mean frequency from one half of the spectrum. In this way, the evolution of M_y may be followed and used to map the audio-frequency magnetic field strength, as shown in Figure 2.11c for a current with voltage ~ 1.5 mV. The strength of the field at the center of the loop is calculated to be ~ 300 nT (these data were collected well above the sensitivity threshold), and the field map is in good agreement with simulations of the magnetic field density from a current loop (see Section 2.4.2). The node-like features near the edge of the sample tube are caused by RF inhomogeneity, as verified by an image of the RF nutation frequencies within the sample. In situations where the current sources are not isotropically distributed, or where multiple frequencies are stimulated by the resonant spin lock, the oscillatory behavior becomes less distinct and the saturation effect manifests itself as a damped exponential decay with a rate constant shorter than the intrinsic $T_{1\rho}$.

2.4.2 Loop Field Simulation

Simulations of the magnetic field generated by a simple current loop were performed in Comsol 3.5 using the AC/DC module. The model system consisted of an 8 mm diameter cylinder surrounding the current-carrying "loop," which was modeled as a torus of 28-gauge copper with 6.5 mm loop diameter. Appropriate current density (to model the experiments at 1.5 mV) was determined by connecting a $2\,\Omega$ resistor in series with the single loop phantom and measuring the corresponding voltage drop for a number of signal amplitudes in order to find the current. A map of the axial magnetic flux density within the loop (in T) is shown in Figure 2.12, which shows a magnitude of several hundred nanotesla in the central region of the loop and an increasingly stronger field near to the wire. This is consistent with our Fourier analysis, especially given the non-ideal nature of our loop phantom (caused by mild
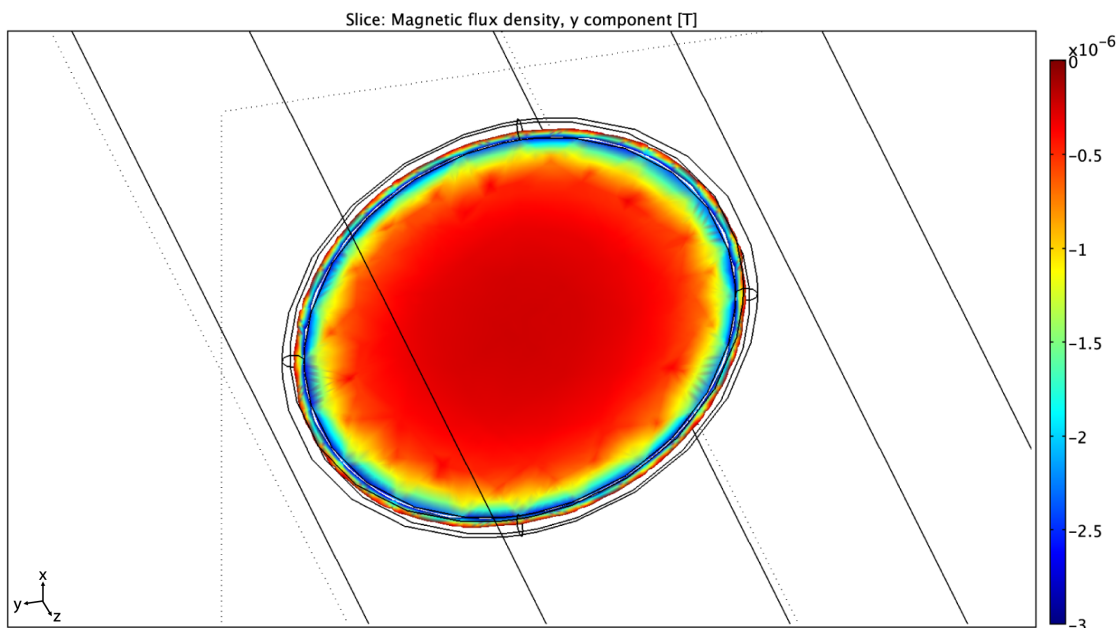
Figure 2.12: Finite element simulation of the magnetic field generated by a 6.5 mm diameter copper loop, at 1.5 mV applied voltage. The calculated axial magnetic flux density is several hundred nanotesla in the center of the loop, consistent with the results of the Fourier field mapping technique described earlier.

deviations from circularity and the transition to the leads running above the loop).

2.4.3 Spectroscopic Control via Modulated Spin Lock Pulses

Because the contrast mechanism is under spectroscopic control, several modifications to the spin lock might render the sequence able to selectively excite specific bands of the current spectrum, and also make it more robust in the presence of experimental imperfections including RF inhomogeneity. As a test of this idea, we explored several variations on the elementary rotary saturation pulse sequence.

The frequency range over which the resonant mechanism operates to produce detectable changes in the image is a particularly important feature of this experiment, especially with respect to *in vivo* neuronal activity. The resonant saturation effect remains strong at lower frequencies: experiments were performed at conditions down to one 200 ms cycle of current oscillating at 5 Hz (Figure 2.13 shows a current imaging experiment performed at 10 Hz). However, the very weak spin lock fields required to meet the resonant condition contribute to increasingly noticeable artifacts due to imperfections in the spin lock field [158], shown in Figure 2.14a. Fortunately, this effect can be easily corrected through the use of a phase-alternating spin lock sequence designed to refocus the effects of inhomogeneities in the spin lock pulse as well as RF inhomogeneities in the B_0 field [24][15][158] (as illustrated in Figure 2.14b). It is important to note that the simplest of these sequences ($\pi/2_x - \tau_{sl}/2_y - \tau_{sl}/2_{-y} - \pi/2_{-x}$) will refocus the accrued phase angle from the resonant rotation as well as the inhomogeneous effects. Insertion of a π_y rotation in the center of the

10 Hz spin lock, no current   10 Hz spin lock, current on
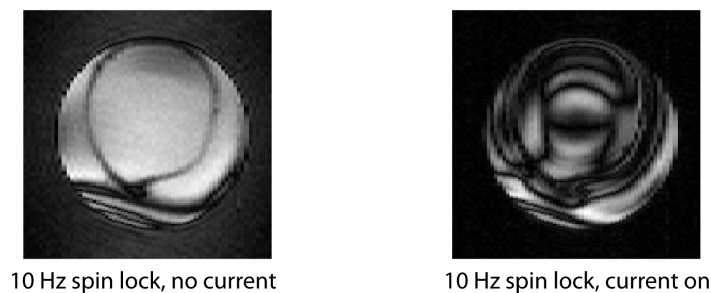
Figure 2.13: Demonstration of resonant current detection performed at very low ω_c (10 Hz). At left, a control experiment is performed with a resonant spin lock but no current. At right, a 10 Hz current is applied simultaneously, causing obvious current saturation effects in the image. The banding artifacts present in both images are characteristic of low power spin lock experiments, and may be eliminated through a modified spin lock sequence, as discussed below.

sequence compensates for this effect and, with a 180° change in phase of the storage pulse $(\pi/2_x - \tau_{sl}/2_y - \pi_y - \tau_{sl}/2_{-y} - \pi/2_x)$, provides a spin lock which is insensitive to inhomogeneities in both B_0 and B_{sl}. Thus, with the use of phase-alternating spin lock sequences, the resonant direct detection method provides consistently strong effects throughout the full range of neuronal activity.

A
Uncompensated spin lock

B
10 Hz, compensated spin lock

50 Hz   25 Hz

10 Hz   5 Hz

$(\pi/2)_x$ π_y $(\pi/2)_x$

$(\tau_{sl}/2)_y$ $(\tau_{sl}/2)_{-y}$
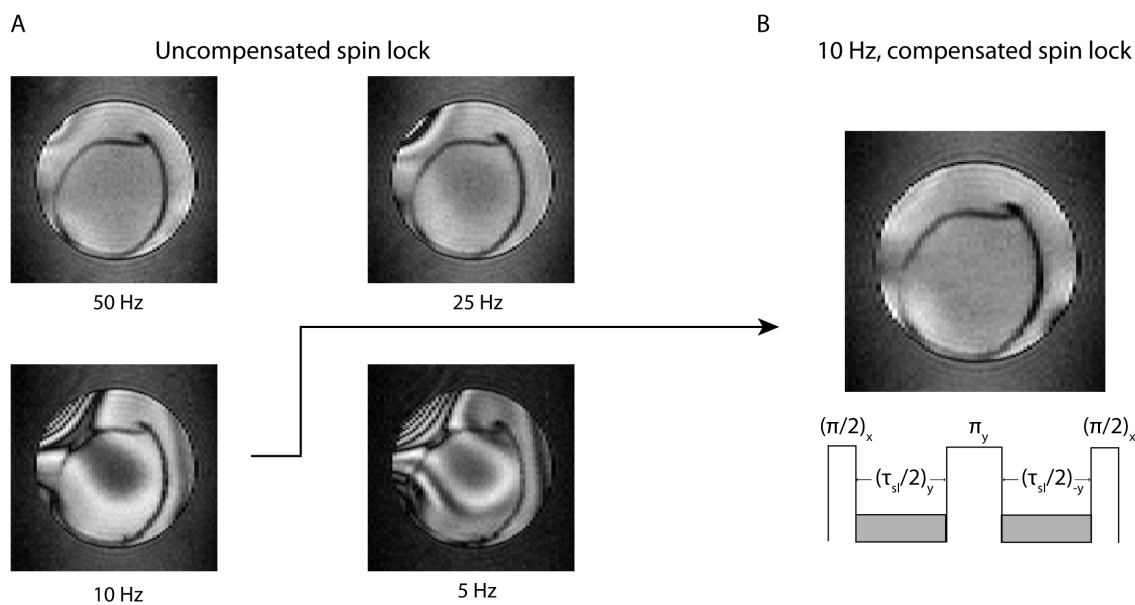
Figure 2.14: 2D images illustrating the characteristic banding artifacts caused by B_0 and B_{sl} inhomogeneities at weak spin lock powers. In (a), we see control images taken with spin lock powers resonant to 50, 25, 10, and 5 Hz (no current is applied). In (b), the 10 Hz experiment is repeated using a phase-compensated spin locking sequence $(\frac{\pi}{2}_x - \frac{\tau_{sl}}{2}_y - \pi_y - \frac{\tau_{sl}}{2}_{-y} - \frac{\pi}{2}_x)$, leading to near-complete elimination of artifacts.
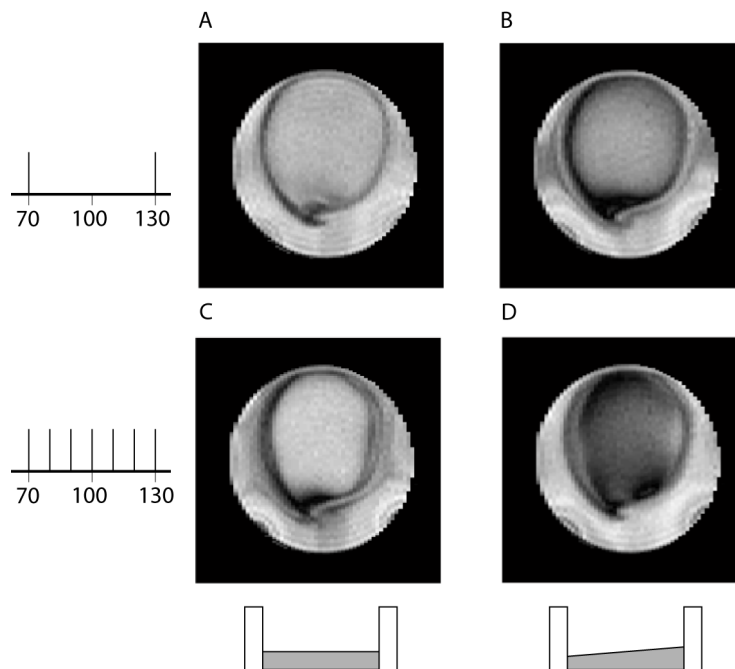
Figure 2.15: 2D images taken with multi-tone current signals ($V_c = 1.5$ mV). Two illustrative situations are shown: the top row shows images taken with a current pulse containing 70 Hz and 130 Hz frequencies, both with (a) the standard constant-amplitude spin lock at resonance and with (b) a ramped spin lock which increases from 70% to 130% of the resonant power ($\tau_{sl} = 100$ ms). The bottom row shows images taken with a current pulse containing frequencies from 70 Hz to 130 Hz, in 10 Hz increments, again (d) with and (c) without a ramped spin lock.

Images using a current excitation spectrum containing several frequencies were also explored in order to approximate the effect of incoherent neuronal currents. The current signal (a sum of sine functions with randomly assigned phase, i.e. $\sum_i a_i \sin(\omega_i t + \varphi_i)$) was comprised of a series of frequencies spanning the resonance condition (but not necessarily containing the resonant frequency). In addition to the typical constant-amplitude spin lock, images were taken with a ramped spin lock in which B_{sl} is linearly increased from 70% to 130% of the resonant power. As shown in Figure 2.15 for a signal containing 70 Hz and 130 Hz frequencies, the addition of the ramped spin lock (b) shows a marked improvement over a spin lock with constant 100 Hz amplitude (a). Figures 2.15c and 2.15d show images taken with a signal containing frequencies from 70 Hz to 130 Hz in 10 Hz increments. While the ramped version is dramatically enhanced, it should be noted that a constant resonant spin lock power still produces substantial resonance effects when multiple frequencies are present within a signal.

2.4.4 3D Images & Frequency Selectivity

Figure 2.16a shows a 3D image of the resonance effect with 500 μV current at 100 Hz in a single loop, with contours denoting the intensity of saturation. Images such as these are an extraordinarily simple way to visualize the full spatial extent of the magnetic field, and could easily be combined in a τ_{sl}-incremented series to form a complete 3-dimensional map of

A   B

0.3 cm
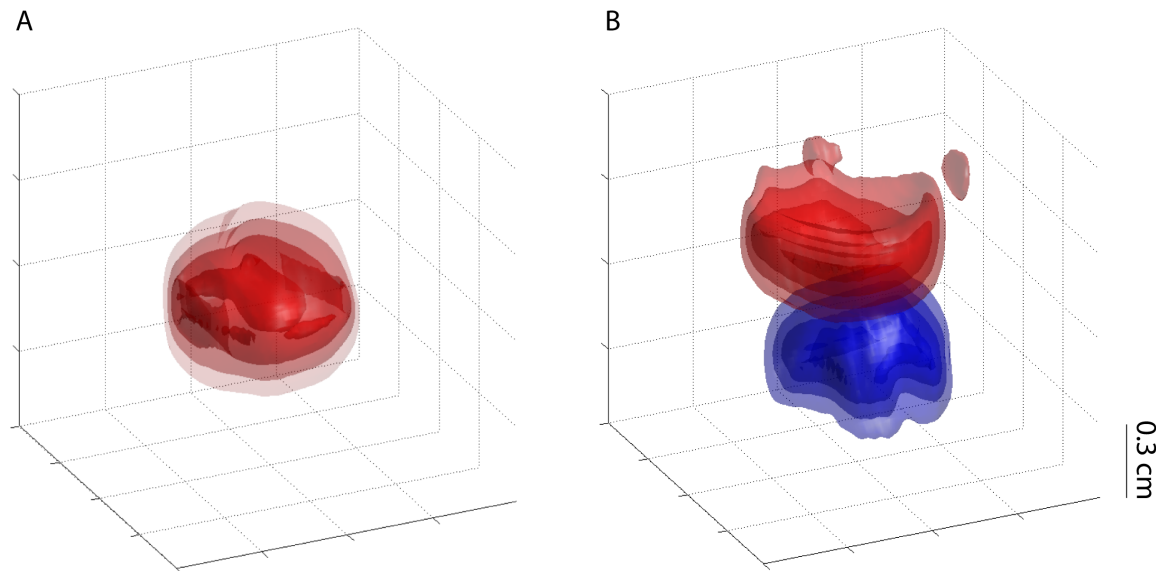
Figure 2.16: 3D images of the saturation effect at $V_c = 500$ μV. In (a), the single loop phantom is imaged with $\tau_{sl} = 50$ ms and $\omega_c = 100$ Hz. In the double loop phantom of (b), current ($\tau_{sl} = 160$ ms) is applied simultaneously in each loop at different frequencies, while the spin lock power is switched between resonance conditions to selectively image only one loop (the figure shows an overlay of the two separate experiments). The top loop (red) has $\omega_c = 100$ Hz, while the bottom loop (blue) has $\omega_c = 250$ Hz. Contours are shown at 30%, 50%, 70%, and 90% saturation (increasing in opacity) with respect to controls.
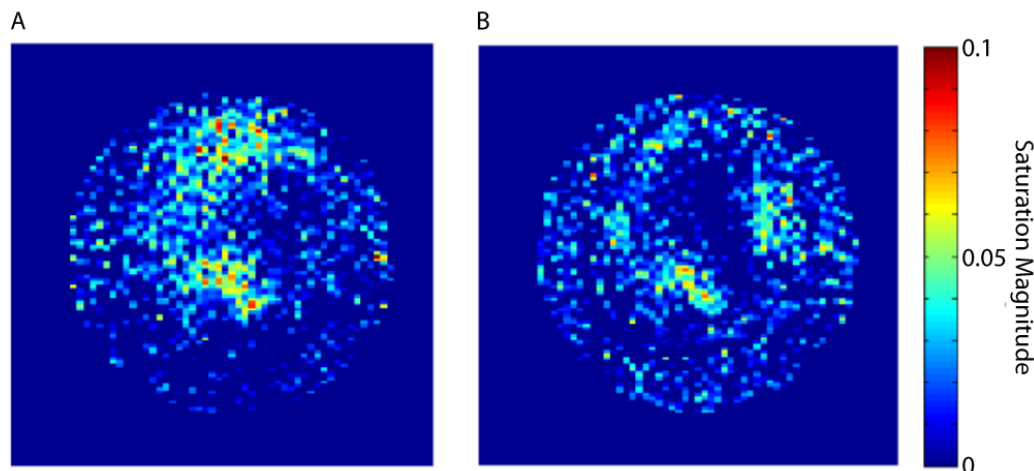
Figure 2.17: Images of a single loop at very low driving voltages. The voltage of the audio-frequency currents are approximately (a) 4.74 μV and (b) 2.38 μV, with estimated field strengths at the center of the loop of (a) 0.92 nT and (b) 0.46 nT. Images were taken with $\omega_c = 100$ Hz, $\tau_{sl} = 160$ ms, and 8 averages. Voxel magnitude is displayed as percentage saturation with respect to a control.

the audio-frequency magnetic field strength throughout the sample. A related experiment, shown in Figure 2.16b, demonstrates the application of this technique in frequency-selective current-imaging. Two loops were axially aligned, each carrying simultaneous current pulses at different frequencies (but equal amplitudes) during the spin lock interval. By simply adjusting the power of the spin lock to match one of the two frequencies, the rotary resonant effect in each loop may be imaged independently.

2.4.5 Sensitivity

The limits of detection are determined by the angle of rotation that the y-magnetization is able to traverse during the spin lock period, which is limited by the strength of the current-induced field and the duration of the current burst (since $\omega_c = -\gamma B_c$, $\phi_{rot} = -\gamma B_c \tau_{sl}$). Because the spin lock module ends by projecting the y-magnetization, the first point of maximum saturation will occur when the audio-frequency field rotates the spins through an angle of $\pi/2$. When very small magnetic fields are being imaged (small B_c), the correspondingly slow rotation of the transverse magnetization means that relaxation will govern the sensitivity. Thus, samples with long relaxation constants will permit longer spin lock times (and therefore larger angles of rotation) before the image degrades.

Figure 2.17 shows two images with audio-frequency current voltages of (a) 4.74 μV and (b) 2.38 μV using a 160 ms spin lock in a sample of 20% H2O and 80% D2O doped with ~ 0.5 mM GdCl$_3$ ($T_1 = 463$ ms, $T_{1\rho} = 336$ ms at 100 Hz spin lock). Comparisons of the average signal (in a region containing noticeable current effects) to the RMS noise give signal-to-noise ratios of ~ 2.5 and ~ 2.0, respectively. The magnetic field generated at the center of the loop in (b) is calculated to be approximately 0.46 nT, based on the level of attenuation and comparison with the current voltage and calculated field strength from the field map

experiment shown in Figure 2.11. Previous characterizations of the SIRS method [159] found sensitivity on the order of 1 nT, which is in excellent agreement with these experiments.

2.4.6 Imaging of Externally Applied Currents *in vivo*

While the detection of neuronal currents remains the most important goal in the development of a direct current detection methodology, there are other applications which should not be overlooked. As discussed earlier, knowledge of the distributions of externally applied current within tissue could prove to be extremely valuable in calibrating imprecise techniques such as defibrillation and electroconvulsive therapy (and could also aid in the design and characterization of materials with specific electrical properties). To this end, we have initiated a collaboration with Professor Kamil Ugurbil at the University of Minnesota Center for Magnetic Resonance Research to begin exploring *in vivo* applications using externally applied current sources.

The goal for our experiments was to perform direct current imaging on lab rats, which would be accomplished by implanting electrodes on opposite sides of the cranium, applying a very small current, and performing the normal spin lock-based resonant detection sequence. Our initial experiments were performed using an agar gel phantom, made to have relaxation properties comparable to brain tissue. Using a primitive MASTER-8 programmable voltage source (A.M.P.I., Jerusalem, Israel) to output an oscillating signal (limited to an oscillating step function rather than a sinusoid), we were able to perform a sweep of the spin lock power, determining an approximate match for the resonant condition. A gradient-echo multi
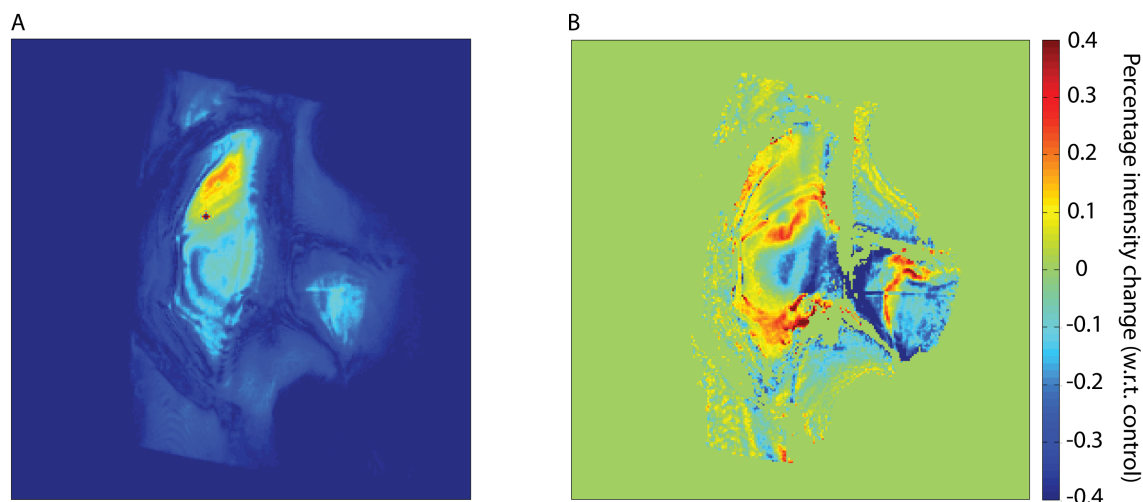
Figure 2.18: Preliminary demonstration of resonant current imaging within a brain-like agar phantom. A GEMS image of the agar phantom is shown in (a), after the application of the spin lock module but with no applied current. In (b), we show a difference image illustrating the percentage change in image intensity between an experiment with 20 V applied current ($\omega_c = 250$ Hz) and a control. The severe inhomogeneity of the available surface coil resulted in nonuniform image intensities and difficulties in matching the rotary resonance condition throughout the sample.

slice (GEMS) imaging sequence was decided upon after testing several options, and a very preliminary demonstration of observed saturation effects from current encoding can be seen in Figure 2.18. In (a), we see a GEMS image taken with the spin lock present but in the absence of applied current. A complementary experiment with applied current of 20 V was then performed, which can be compared with the control to give the image shown in (b), illustrating the percentage change in intensity with the applied current. A similar experiment performed at 10 V gave an identical pattern, but with decreased percent differences, confirming that these effects can be correlated with the applied current.

While the initial results are promising, experimental capabilities were limited due to the lack of an encoding coil with adequate RF homogeneity (at the time, we had use of a surface coil, which provides adequate homogeneity for planar areas near the coil, but increasingly poor homogeneity in deeper regions). This can be seen in Figure 2.18a, which shows highly nonuniform image intensity across the agar phantom. Furthermore, the RF inhomogeneities in the excited volume compromised the uniformity of our spin lock pulse and made it very difficult to achieve proper excitation and inversion pulses. Thus, our ability to meet the resonant condition throughout the sample was quite poor in these initial experiments, despite efforts to find effective adiabatic pulses and to compensate the spin lock [15] in a manner similar to Section 2.4.3. Fortunately, we have secured the use of a homogeneous volume coil for future experiments, and can easily bring our own function generators to take the place of the MASTER-8.

2.4.7 Remote Detection

While we have already demonstrated that this method can detect current distributions of biologically relevant magnitudes, we recognize that the conditions of any in vivo current imaging experiment would be far less ideal. There, the experiment will be principally limited by non-idealities and incoherence in the signal source as well as low filling factors, compromising the sensitivity necessary to elucidate neuronal currents with physiologically informative spatial resolution. The former may be mitigated by appropriately compensated spin lock sequences, as discussed earlier; in order to address the latter problem of detecting very small volumes of resonant spins, we have explored the use of remotely detected MRI [98] (for a more comprehensive discussion of remote detection and its applications, please refer to Chapter 3).

In a remote detection sequence, the encoding and detection portions of the experiment are spatially separated and individually optimized. This approach has been applied to flows in microfluidic systems and porous materials (see Chapters 3, 4, and 5), and is now being applied to study biological microvasculature, including blood flow within the brain. In the case of a remote current detection experiment, the encoding region contains the oscillating currents of interest and nuclei flowing through it are subjected to an analogue of the normal phase-encoded, resonant current detection sequence that has been adapted for flow. The magnetization is stored longitudinally and is detected elsewhere in a coil whose filling factor is matched to the voxel size of interest. When the detector is an optimized microsolenoid or surface coil, and the encoding coil is a volume coil or large surface coil, the approach yields a sensitivity enhancement of several orders of magnitude over conventional detection (see [41], Section 1.1.5, and Chapter 3 for further discussion and examples of the sensitivity
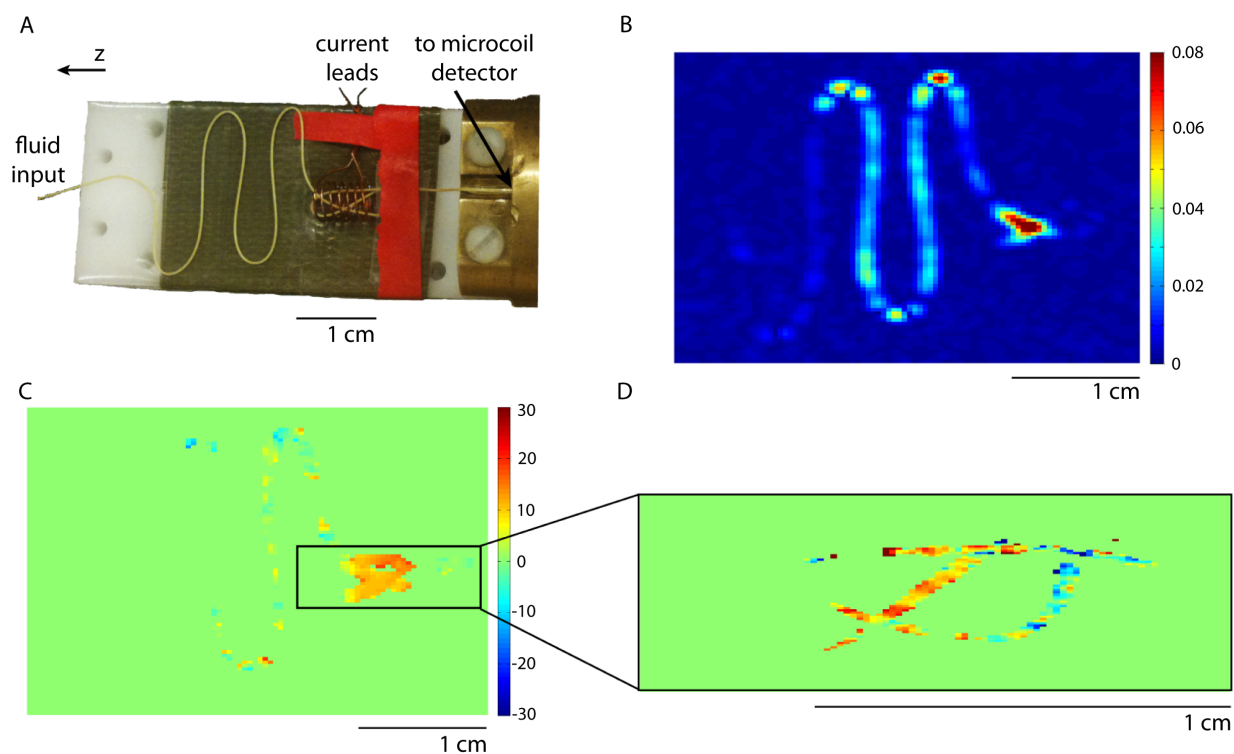
Figure 2.19: Remotely detected current imaging experiments in (a) a serpentine flow phantom. Water flows in 150 μm PEEK tubing laid out in s-shaped curves, travels through a solenoid in which audio frequency current encoding takes place, and then flows into an optimized microsolenoid NMR detector. (b) A single time-of-flight image from a control experiment without current excitation. Images illustrating the phase accrued during current excitation and due to a resonant mechanism, relative to a control, are shown for: (c) a non-selective experiment with $FOV_y = 2.41$ cm and $FOV_z = 3.62$ cm, and for (d) a "zoomed in" experiment which isolates a slice containing the coil, giving $FOV_y = 0.48$ cm and $FOV_z = 1.45$ cm. Images were taken with $\omega_c = 400$ Hz, $\tau_{sl} = 20$ ms, and $V_c = 1.6$ mV. All images have resolution 90×90 after zero-filling by a factor of 2 and have comparable signal to noise.

enhancement).

Figure 2.19a shows the flow phantom constructed for this experiment. Water flows (at $\sim 160\ \mu\text{L/min}$) through a length of 150 μm ID PEEK tubing fashioned into a planar serpentine structure and secured to a flat support by means of double-sided adhesive film. It then enters a solenoid ($\sim$ 0.5 cm diameter) used for current-encoding, is looped to increase the transit time in the current excitation region, and finally travels to a microsolenoid detector of $\sim$ 150 nL volume (approximately matched to voxel size). The remote detection sequence consists of excitation into the transverse plane (with optional slice selection), current encoding via a synchronous current burst and resonant spin lock pulse sequence, velocity-compensated phase encoding along two spatial axes, and, finally, a pulse to store all encoded magnetization along the z-axis for transport to the detection coil (see Section 2.3.3 and Chapter 3 for more details). Data are acquired from the flowing system by stroboscopic acquisition in the detector microcoil, yielding all encoded information together with a correlated time-of-flight parameter that reflects transit to the coil. Figure 2.19b shows a 2D time-of-flight image from a control experiment with no application of current. In Figure 2.19c, we show the phase difference (in degrees) between a control and a current encoding experiment with 1.6 mV current at 400 Hz and $\tau_{sl} = 20$ ms, which clearly shows detection of resonant phase effects localized to the region of the solenoid (some residual phase remains in the serpentine region due to minor deviations in data between experiments). Furthermore, because the remote detection experiment is optimized when the voxel volume is matched to the detector volume, the image field of view can be narrowed (or alternatively, a smaller slice can be selected) without the dramatic loss in sensitivity associated with the comparable set of directly acquired experiments. Figure 2.19d shows a phase contrast experiment in which the coil region has been isolated and "zoomed in" by applying a slice selective pulse and narrowing the field of view. The features of the coil are resolved with far greater clarity at no cost to experiment duration or sensitivity.

2.5 Discussion

Our experiments demonstrate the substantial benefits of resonant current imaging as compared to non-resonant alternatives. The difficulties associated with using phase contrast MRI to image oscillating currents at higher frequencies significantly limit the utility of conventional techniques, especially given the likely importance of high gamma activity (60-250 Hz) in brain function. Using the resonant method, low-intensity currents can be detected at any chosen frequency, allowing for frequency-selective imaging across the full spectrum of neuronal activity. In the case of neuronal current imaging, this technique could be applied to independently localize different types of brain activity in a set of experiments. In addition, the resonant method is unaffected by other factors that may diminish or eliminate the conventional phase contrast MRI signal, including the position of the current source within an imaging voxel, and the degree of coherence of the exciting waveform.

Sensitivity has been a primary focus in the development of current imaging techniques, largely due to the emphasis on pushing the method towards the regime of neuronal currents. Estimates of the magnetic field from synchronized neuronal activity range from the pT scale [21] to 0.1 - 1 nT [13]. While the authors of the former estimate acknowledge that the

corresponding simulations were performed at a neuronal density several factors less than is realistic, it is certainly clear that sub-nT sensitivity is necessary for direct neuronal current imaging to become viable. To assess whether or not our method is a realistic candidate, we note that the T_1 of water in grey matter ranges from approximately 1 - 1.8 s (depending on the external field) [132], while the $T_{1\rho}$ for grey matter at 1.5 T is approximately 100 ms with a 500 Hz spin lock field [15]. Thus, it is the latter factor which provides the primary limitation on the angle of rotation that may be accrued in the transverse plane without allowing unacceptable signal degradation. The experiments described above demonstrate sub-nT sensitivity for a current burst of 160 ms, although additional images taken with τ_{sl} comparable to $T_{1\rho}$ yield very acceptable images. While a slight reduction in sensitivity would be expected with a decrease in τ_{sl}, it could be more than compensated by additional averaging or further optimization of the instrumentation. However, to fully investigate the bounds of sensitivity, further care with instrumentation and coil design would need to be taken in order to generate a clean signal at extremely low voltages and also to eliminate the effects of RF inhomogeneity throughout the sample.

The resonant mechanism proved very effective even when using one current cycle at 5 Hz, provided that a phase-alternating spin lock is implemented to compensate for RF inhomogeneities in B_0 and B_{sl}. Frequencies below 5 Hz may begin to pose some difficulty, as they require increasingly long spin lock durations for meaningful oscillatory behavior to take place (alternatively, direct phase imaging may be viable at these frequencies due to the extremely slow variation in signal and decreased cancellation of accumulated phase). However, with regards to biological applications, the entire frequency range of neuronal activity fits comfortably inside the range of our method, and may easily be probed via resonant current imaging. Furthermore, currents with multiple constituent frequencies do not preclude application of the technique, allowing robust current imaging suited to a wide range of possible signals.

In addition to the obvious applications in the development of neuronal current imaging, the resonant technique can easily be applied to selectively map other current distributions with high resolution in vivo. Current imaging techniques would be invaluable in the calibration of imprecise medical procedures such as defibrillation, electroconvulsive shock therapy, and deep brain stimulation, and the flexibility, sensitivity, and control of the resonant spin lock technique would add a great deal to the existing work in this area [64][65][163][164], especially with regards to rapidly oscillating fields and samples containing multiple or incoherent frequencies. Our collaboration with Prof. Ugurbil at the University of Minnesota is ongoing, and we anticipate that the use of a homogeneous volume coil and a more robust function generator will allow us to overcome our early experimental difficulties. The theory of resonant current detection is fully applicable within materials as well as liquids, and continuation of our experiments will provide a clear and practical demonstration of resonant current detection within biological tissue.

Finally, we demonstrate the application of our technique to a remote detection experiment, in which we are able to detect significant phase contrast within very small volumes of flowing liquid. By separating the encoding and detection steps of the MRI experiment, remote detection allows the separate optimization of each. We are thus able to overcome filling factor, magnetic susceptibility, and other limitations to achieve high spatial and temporal resolution without sacrificing sensitivity. In this way, we can easily acquire high-resolution

images which display features of the phase distribution that may otherwise be compromised by spatial averaging when viewed at lower resolutions.

We are presently adapting remote detection to the imaging of microvasculature in vivo, an idea which is also well-suited to neuronal current detection. In this case, functionally relevant volumes of current-encoded blood must reach the detector before spin relaxation erases the encoding. Assuming that the encoded volume is the brain and that the detected volume is a segment of the jugular, typical physiological parameters and blood flow rates suggest that a remote experiment is within reach. As with any experiment involving flow, the resolution will be limited by the incoherent motion of the spins during the encoding time, arising from effects such as diffusion during the spin lock period. Spin motion during the image encoding is more easily ameliorated: rapid imaging sequences such as echo-planar imaging [133] can dramatically shorten acquisition times, and a number of techniques including breath-hold [83], cardiac synchronization [79], and motion compensation [4] are routinely applied under similar circumstances.

Chapter 3

Remote Detection Methodology

3.1 Introduction

In the eight years since it was first introduced [98], remotely detected (RD) magnetic resonance has evolved into a highly flexible modality that can enable previously impractical experiments at relatively low cost. Many applications of remote detection in dealing with very small volumes of flowing liquid have already been described in detail [51][40][54][95][50][41][6], and various evolutions of the experimental methods can be found [48] as the technique has matured. The goal of this chapter is to provide a unified description of the remote detection experiment, from probe design schematics to pulse sequences to data processing procedures, providing a complete set of tools for the application of this practical method.

As discussed in Section 1.1.5, the coil "filling factor" provides the largest limitation to the detection of small volumes of liquids (such as those found in capillaries, microfluidic chips, porous media, and so forth). The simplest way to enhance the detection sensitivity is to reduce the size of the detection coil so that the enclosed volume closely matches the amount of detectable spins. As the sensitivity of detection is directly proportional to the filling factor, a microsolenoid with diameter comparable to the capillary or microfluidic channel will offer significantly improved detection capability [154][41]. Thus, the ideal way to achieve high sensitivity would be to wind a microcoil around a specific region of interest inside of the column. While conceptually sound, this is clearly infeasible in practice. Remote detection bypasses these limitations by providing a general method that integrates the improved sensitivity of a localized coil into a robust platform capable of imaging entire microdevices.

This is accomplished by splitting the traditional magnetic resonance experiment into two components (encoding and detection), which are separated in both space and time. A schematic illustration of the basic setup for a remote detection experiment is shown in Figure 3.1. The first part of remote detection, referred to as encoding, occurs within a conventional inductive coil which encloses the sample of interest (e.g., a microfluidic chip or chromatographic column). This coil (and the enclosing gradient stack) can be used to encode spatial (RD-MRI), chemical (RD-NMR), and velocimetric information in the phase of the nuclear spin magnetization of the fluid.

Following encoding, the phase information is rotated back along the longitudinal axis for storage and transportation, where the comparatively long T_1 relaxation processes allow
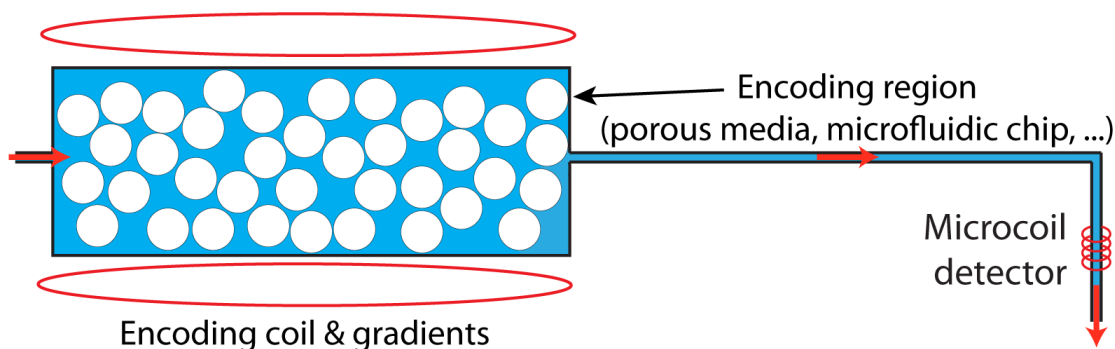
Figure 3.1: Illustration of the setup for a remote detection experiment. Fluid flows into the region of interest, where it is subjected to a series of encoding pulses from surrounding coils and gradients. Following encoding, the stored magnetization is carried through a capillary to a microcoil detector, where the closely matched filling factor provides significant gains in sensitivity.

the fluid time to travel through a connecting capillary and into an optimized microcoil detector. It is here that the second component, detection, takes place. Since the volume of this detector is matched to the volume of the microfluidic features of interest, a sensitivity enhancement of $2-3$ orders of magnitude may be achieved [41][6]. Fourier transformation of these data will yield any encoded spectroscopic or image data, as well as a correlated time of flight parameter that reflects transport of fluid from the encoding region to the detector. The implications of this time-of-flight dimension, as well as further details of the RD pulse sequence, are discussed below.

The latest generation of RD probes has evolved into an inexpensive, highly modular design that can be easily adapted to the system of choice. As the principle of remote detection lies in the physical separation of encoding (imaging, spectroscopy, velocity encoding, etc...) and detection steps, two separate probes are used for the experiment. The detection probe, typically built with a microcoil to enable experiments on extremely small volumes of liquid, is inserted from the top of the magnet, allowing it to sit within the homogenous region and mate with the gradient stack and, if desired, a commercial volume probe used for encoding. An alternative option, presented in Section 3.3.2, is the use of a small, custom-made surface coil probe which can be directly attached to the detection probe and which is an excellent solution for encoding planar sample volumes such as microfluidic chips at good sensitivity and very low cost.

The most recent pulse sequence for standard remote detection experiments has been expanded to include a variety of additional features. As shown in [6] and Chapters 4 and 5, the addition of phase-compensated velocity-encoding gradients allows the measurement of individual velocity components, and can be integrated with time-of-flight imaging to provide a comprehensive description of the flow field in both Eulerian and Lagrangian frames of reference. Additional modifications are also possible, including T_2 relaxation encoding, gradient shimming during detection, and changes in the gradient coordinate system. Finally, the relevant data processing techniques are outlined along with a brief introduction to the application of subsampling and compressed sensing to remote acquisitions. These
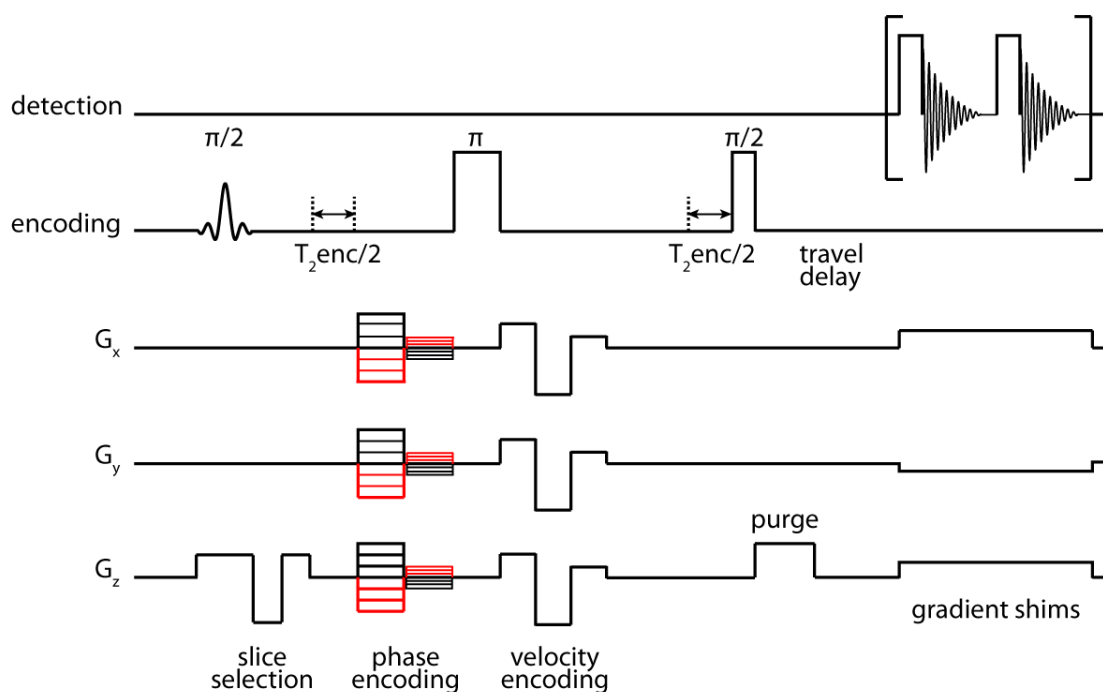
Figure 3.2: Pulse sequence for multidimensional remotely detected imaging experiments, shown with optional velocity and relaxation encoding steps and additional gradient shims. Following the initial slice-selective excitation, information regarding the position, velocity, and relaxation properties of the fluid may be encoded in the phase of the spins. Information is stored along the longitudinal axis for transport to a microcoil detector, where it is read off stroboscopically to provide an additional time-of-flight dimension.

techniques can dramatically shorten remote detection experiments, allowing collection of high-dimensionality datasets which would have been previously infeasible.

3.2   Pulse Sequences for Remote Detection

The essential components of a remote detection sequence (excitation, encoding, storage, and detection) form a simple framework upon which a wide variety of specialized pulse sequences can be built. A number of these modifications have been described in previous studies [6] as well as in Chapters 4 and 5, so the aim of this section is to provide a brief, practical survey of the current pulse sequence and its extensions in order to be of aid to those wishing to make use of the technique.

A schematic pulse sequence is shown in Figure 3.2. Each remote sequence is split into two parts, both physically and temporally, separated by translational flow. In the encoding segment, spins traveling through the region of interest are excited, either with a non-selective hard pulse or with a slice selective shaped pulse (such as a sinc function) in the presence of a gradient designed to null erroneous phase due to spin motion during its application (discussed *vide infra*). As described in Section 1.2.5, the width of the slice may be adjusted by changing either the shape of the pulse (through its power, duration, or functional form)
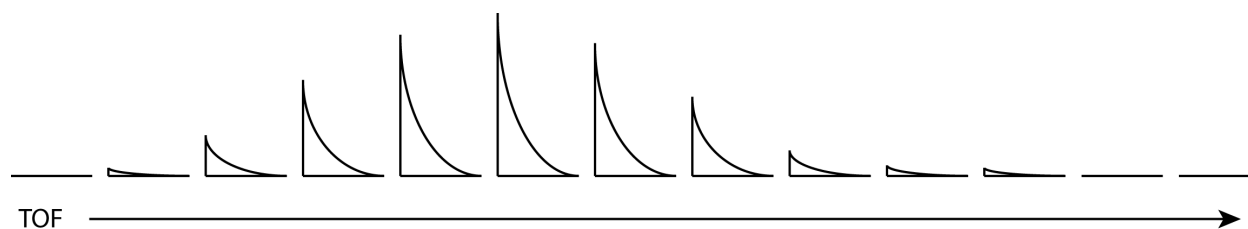
Figure 3.3: Illustration of a remote detection travel curve.

or the strength of the slice selection gradient.

3.2.1 Travel Curves

The simplest remote detection experiment practically eliminates the encoding portion, and consists only of an excitation, optional echo pulse, storage pulse, and detection. The effect of this, when combined with a phase cycle that cancels out signal from any unencoded spins (briefly discussed below), is to give a sequence of FIDs arrayed along the time-of-flight dimension as shown in Figure 3.3. Because the only remaining signal is from the originally encoded spins, one will see the FIDs grow in amplitude as the fluid arrives at the detector, and then trail off as the bulk of the encoded volume flows through (without the phase cycle, the travel curve will show a baseline height and a subsequent dip as the encoded spins pass through).

These experiments are invaluable first steps towards calibrating a remote acquisition. Adjustments to the flow rate will affect how long it takes fluid to reach and then flow through the detector, which is significant when trying to avoid excessive T_1 loss. Correspondingly, the total duration of the acquisition can be adjusted to avoid unnecessary data collection or to compensate for slow flow rates. Finally, the interval of the stroboscopic acquisition should be set to allow enough time for each packet to flow out before acquiring signal from the next (dictated by the coil residence time).

3.2.2 Phase Encoding

The encoding portion of the sequence is performed immediately following excitation. The basic components, such as phase encoding imaging gradients, are applied in a nearly identical way to a direct detection experiment. Images may be encoded through use of motion-compensated phase encoding gradients along all three dimensions, chosen with short durations (typically 500 μs $-$ 1.5 ms) in order to minimize displacement due to flow during encoding. These gradients may be square pulses, or, taking into account the limits on slew rate, can be generated with trapezoidal waveforms. The source of the encoding pulses is flexible, and may be chosen based on the design of the remote probe. While early remote detection experiments utilized a single, specialized probe with both encoding and detection coils, recent designs have shifted towards the more robust auxiliary probe, which contains only the detection coil and relies upon use of another, separate encoding coil such as a standard volume imaging probe or a modular surface coil probe. Design of these probes is discussed in Section 3.3.

In many cases, the sample of interest may be very difficult to properly align with respect to the lab frame coordinate system. For instance, a flexible microcapillary will be extremely sensitive to small rotations or adjustments in the probe position. To that end, it can be advantageous to rotate the coordinate system of the gradients themselves (which applies equally well to both phase and velocity encoding gradients), rather than attempting to blindly realign the sample. The procedure for doing this is particularly relevant to the chromatography experiments described later on, and is fully outlined in Section 5.2.5.

3.2.3 Velocity Encoding

Velocimetric measurements can be integrated into the sequence through the use of phase-compensated velocity-encoding gradient pulses. The theory of gradient moment nulling [113][11], as well as its application to remote velocimetry [6], has been described in detail elsewhere so the description here will be brief. The time-dependent phase of spins moving within a gradient field can be written as:

$$\phi(t) = \gamma \int \vec{G} \cdot \vec{r} \tag{3.1}$$

By expanding the position of the spin in a Taylor series, we can rewrite the accrued phase ($\Delta\phi$) as a sum of "moments," corresponding to position, velocity, acceleration, and so on:

$$\Delta\phi = \gamma z_0 \int G(t)dt + \gamma v_0 \int G(t)t\,dt + \frac{1}{2}\gamma a_0 \int G(t)t^2 dt + \dots \tag{3.2}$$

Careful choice of the gradient waveform allows selective nulling of these moments, with $n+1$ gradient lobes required for the nulling of n moments. Two- (position nulling) and three-lobe (position and acceleration nulling) velocity-encoding pulses have been successfully employed in remote detection experiments, with typical durations of $1-2$ ms.

By taking the phase difference between two experiments performed using gradients of opposite sign, the average velocity within each voxel can be calculated while phase due to spatial inhomogeneities is eliminated. In the case of a three-lobe velocity encoding gradient (most commonly used in subsequent experiments), the relative amplitudes of the lobes are chosen such that the first and third terms of Equation 3.2 integrate to 0. This can be accomplished with the waveform shown in Figure 3.4, which has relative gradient amplitudes of $1 : -1.5 : 0.5$. It is often wise to insert a small delay between each lobe, designated α (typically on the order of 150 μs), in order to allow for the rise time. This doesn't affect the nulling of position and acceleration moments, but does need to be accounted for when calculating the conversion between phase difference and velocity. For this gradient, an integration across $G(t)t$ gives the following conversion between phase difference (assuming the subtraction of two experiments using opposing waveforms) and velocity:

$$v = \frac{2\pi\Delta\phi}{360G\gamma}\left[\frac{\tau^2}{9} + \frac{\alpha\tau}{3}\right]^{-1} \tag{3.3}$$

where velocity is in cm/s, γ is Hz/G ($\gamma_H = 4258$ Hz/G) and G is in G/cm. If a wider range of velocity-encoding values is employed, one can sample the full velocity distribution
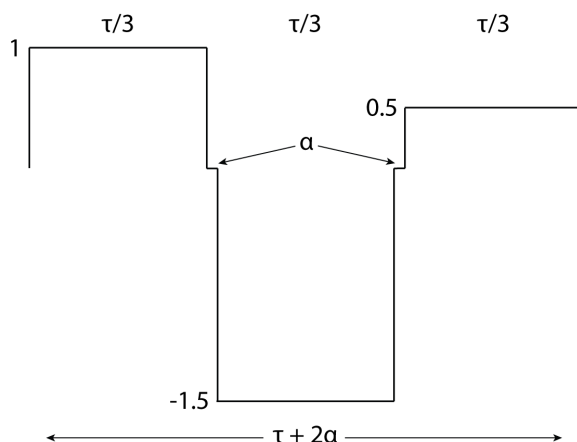
Figure 3.4: Position- and acceleration-compensated gradient, with appropriate lobe amplitudes and durations.

within each voxel by treating the velocity encoding as a Fourier dimension and transforming it to obtain the "q-space" velocity distribution [19]. Much like an imaging experiment, the increment of the velocity-encoding gradient will determine the field-of-view in q-space, and the number of sampled points will correspond to the resolution. This topic will not be discussed further here, but has seen successful application in remote velocimetry experiments using microfluidic channels [6].

3.2.4 Relaxation Encoding

The T_2 relaxation parameters of spins within the encoding region may be measured as well. By inserting an additional incremented T_2-encoding delay into the encoding portion of the sequence and performing several remote detection experiments across a range of delay values, one obtains a set of images with intensities reflecting the transverse relaxation. During processing, the intensity of each voxel is fit to a decaying exponential across this indirect dimension, yielding relaxation parameters either for the bulk sample (without imaging) or for each voxel (with imaging). If a π-pulse is used in the sequence to generate an echo, the delay should be split evenly across either side. However, in the case of fluids with very low T_2 values (below a few milliseconds), the delay required for the imaging gradients may result in dephasing of the signal prior to the storage pulse. Remote encoding of relaxation values can measure physical properties within traditionally inaccessible systems (for instance, susceptibility broadened materials or extremely small volumes of flowing liquid), and has recently been applied within microporous bead packs, as detailed in Section 4.2.

3.2.5 Detection

After encoding has been completed, the spin magnetization is rotated back to the z axis for storage (the storage of each magnetization component requires two steps, and is accounted for in the phase cycle). Following the $\pi/2$ storage pulse, the fluid is allowed to

travel to the detector and a crush gradient along $\hat{z}$ may be used to dephase any unstored magnetization remaining in the transverse plane. Detection occurs stroboscopically in the microcoil using a train of $\pi/2$ pulses and acquisitions timed to the residence time of the fluid packet within the coil. The residence time may be estimated by a simple arrayed 1-dimensional experiment within the microcoil ($\pi - \tau - \pi/2 - $ acquire). As the value of τ is arrayed, the packet of initially inverted spins will display an exponential growth back to their steady-state value. This recovery would be linear in the absence of T_1 relaxation, since it would be dictated only by the outflow of inverted spins. However, because the residence time is much smaller than T_1, the dominant characteristics of the recovery are related to flow and an approximate calculation of the residence time can be made (which should be when the recovery reaches $\sim 90\%$ of the steady-state value). Typical acquisition (and, thus, residence) times for remotely detected experiments are $50 - 100$ ms, with the total volume of encoded liquid taking $1 - 3$ s to flow through the microcoil detector.

One important consequence of detecting flowing fluid is the possibility of spectral broadening. For slowly moving liquid, with coil residence time longer than the detected FID (governed by T_2^* processes), flow broadening will not be an issue. However, higher flow rates may lead to truncation of the detected FID due to shorter coil residence times. In the corresponding spectrum, this will manifest itself as an additional level of line broadening (and possibly ringing artifacts if the truncation is more severe). Because of this, it is worthwhile to fine tune the flow rate to minimize this broadening while still allowing timely transport of spins from the encoding region to the detector. In some cases, this can be a bit of a challenge and some sort of compromise should be found.

An additional challenge presents itself when it comes to shimming. Due to the physical separation between encoding and detection regions, it is necessary to position the probes in such a way that each area is within the sweet spot of the magnet. However, this compromise also implies that neither region will be directly in the center of the homogeneous field, and each will have a slightly different set of optimized shim values. Rather than employing an iterative shimming procedure (in which one makes incremental adjustments by switching back and forth between each coil), additional small gradient pulses can be added during acquisition in order to refine a shim set optimized only for the encoding coil. Thus, an array of gradient shim values can be quickly sampled to determine optimized detection parameters, and may be turned on only during acquisition, greatly simplifying efforts to achieve field homogeneity in both coils.

The last relevant component of the pulse sequence is the phase cycle, which serves to cancel out any detectable signal which might be present from unencoded spins. While the details of phase cycling will be left to more complete descriptions [82], the basic idea can be quickly mentioned. A typical remote detection experiment consists of a four-step phase cycle, which can be thought of as two nested two-step cycles. The innermost of these serves to alternate which component of the phase is stored along the longitudinal axis, as both are needed in order to reconstruct the encoded information. Thus, steps 1 and 3 may store M_x, while steps 2 and 4 store M_y. The outermost loop serves to repeat the first two steps, but with the phase of echo, storage, and receiver pulses shifted by $180°$. In doing so, the signal of successfully encoded spins will remain (since the combination of these phase shifts will not cancel out), but any detected spins subjected to the phase shift in receiver (but not the shift in echo and storage) will vanish, leaving only signal from properly encoded spins.

3.3 Probe Design

3.3.1 Microcoil Detection Probe

Using a modular probe design, auxiliary probes for remote detection can be constructed easily and at low expense, and may be used for a wide range of applications. The latest probe design builds upon the concept of an auxiliary probe discussed in previous works [48][49], in which the body houses the detection coil but relies upon a second probe to provide the encoding pulses. This can be either a clear bore imaging probe or an attachable surface coil probe. The design and application of the latter is discussed below. In both cases, the microcoil detection probe is inserted from the top of the magnet, and adjusted for height such that the encoding and detection regions lie within the sweet spot of the magnet.

Both single- and double-resonance variants of the auxiliary remote detection probe have been constructed for use in an assortment of remote detection experiments. Illustrative views of the single-resonance detection probe are shown in Figures 3.5 and 3.6, with detailed schematics given in Appendix A.1. The probe body shown here is designed to be compatible with a 40 mm imaging probe, but the design can be easily modified to accommodate other
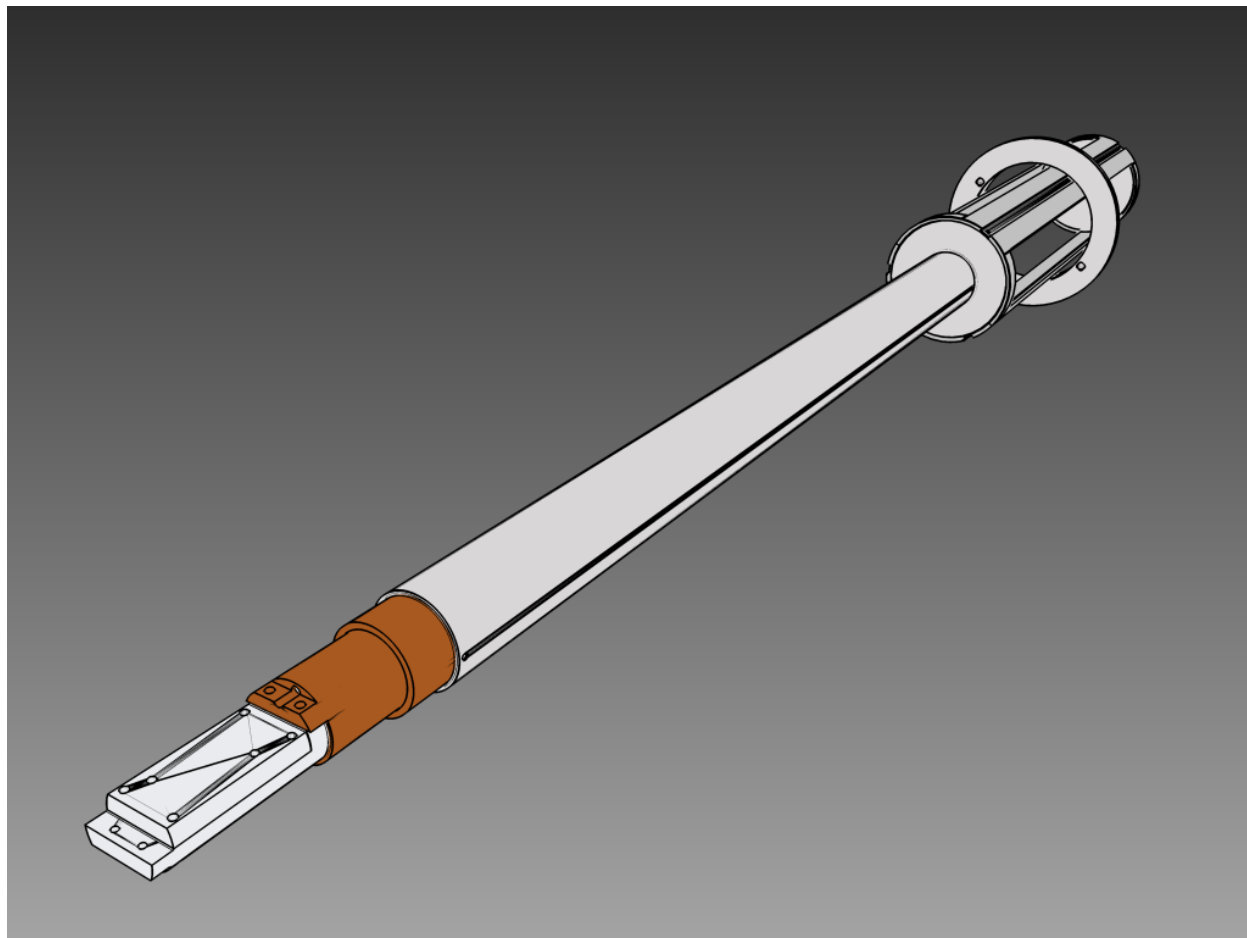
Figure 3.5: Illustrated CAD rendering of the standard auxiliary microcoil detection probe.
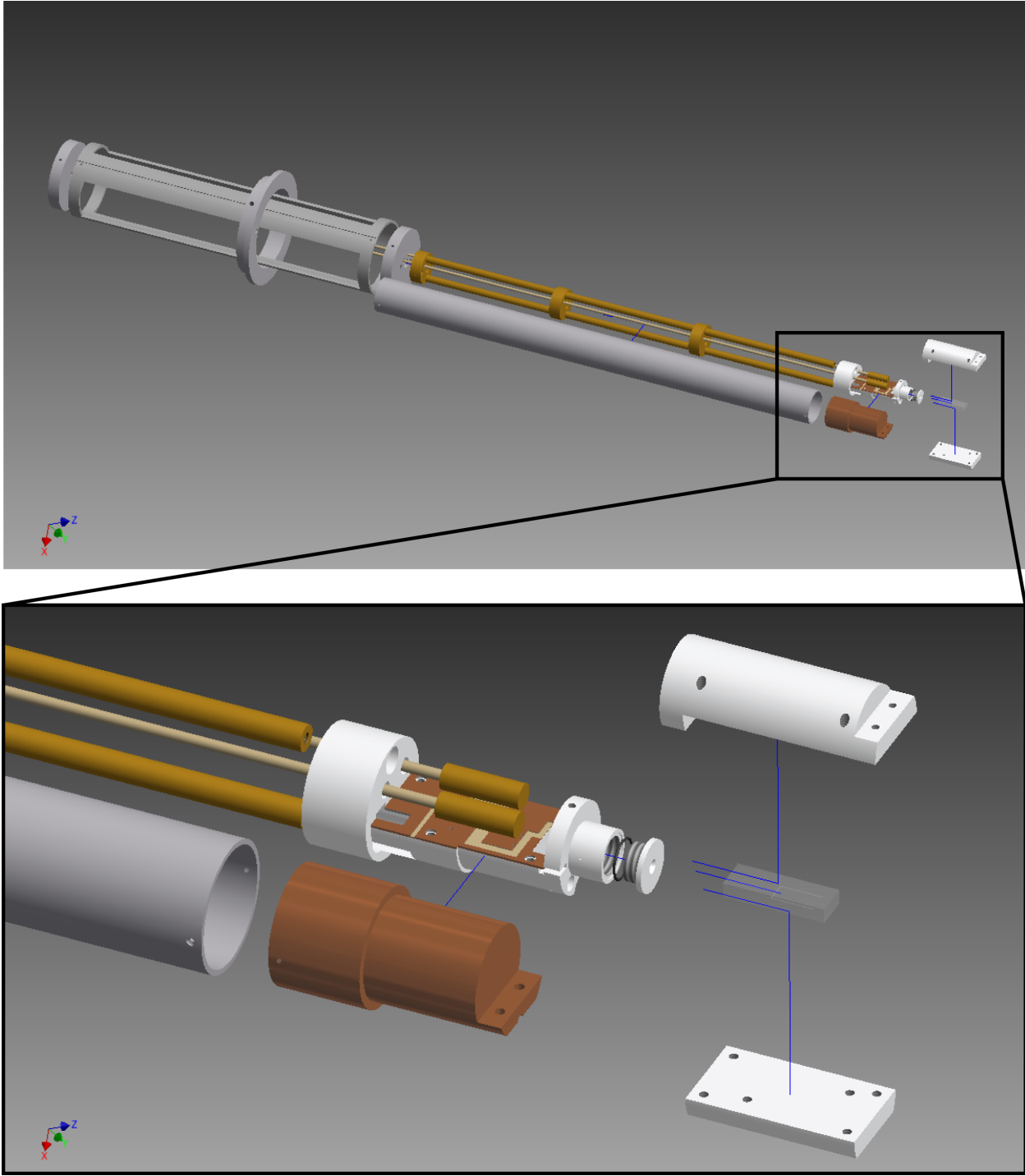
Figure 3.6: Exploded view of the auxiliary microcoil detection probe.

encoding probes.

The main components of the probe are the body, circuitry module, detection coil enclosure, and detachable sample holder. The body consists of a long cylindrical tube and internal support structure, which is inserted from the top of the magnet and can be positioned (via an adjustable aluminum spacer) to place the detection coil and sample holder near the sweet spot of the magnet. An open "cage" sits on top of the main shaft, allowing easy access to the tuning and matching rods as well as the coaxial cable and fluid capillaries.

The circuitry module is connected to the end of the body, and is made up of a plastic support (Delrin or Teflon) to which the circuitboard is attached. The circuitry described here uses two non-magnetic 1 - 30 pF variable capacitors (Johanson) to form the simple resonant circuit shown in Figure 3.7. Typically, one must add additional capacitance (1 - 5 pF) in series with the inductor in order to bring the resonance tuning close to the desired frequency. The detection coil enclosure sits near the top of this support, with the entire assembly housed within a copper shield. The detection coil enclosure is a small cylindrical container, which is sealed to allow immersion of the coil within susceptibility matching fluid (FC-43, 3M), greatly improving the achievable linewidths from the microcoil [134]. The coil itself is supported on a polyimide sheath (Cole-Parmer) running laterally through the container, allowing for easy insertion of capillaries with no need to unseal the enclosure. Finally, some form of sample holder is attached. The holder shown here is designed to provide support and connections for a microfluidic chip (the holder can easily be modified to suit the sample of interest). More detailed schematics for the probe body, circuitry holder, probe circuitry, microcoil container, shield, and microfluidic chip holder are included in Appendix A.1.
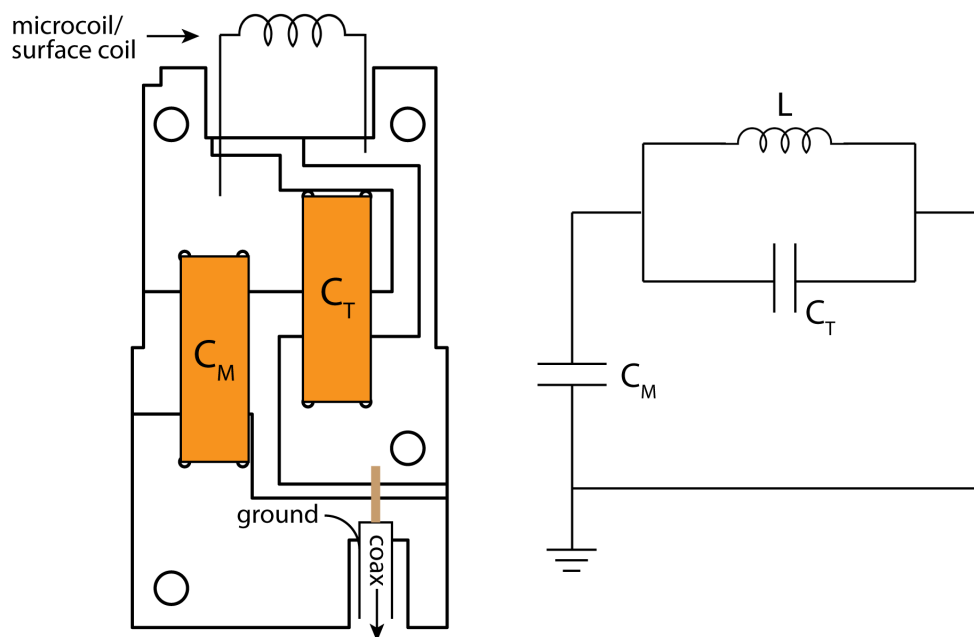
Figure 3.7: Schematics for a resonant probe circuit.

3.3.2   Modular Surface Coil Encoding Probe

The design and construction of a modular surface coil probe is a new contribution to the previously existing hardware and methodology for remote detection experiments. The attachable surface coil, shown in Figures 3.8 and 3.9 (with detailed schematics provided in Appendix A.2), provides an inexpensive alternative to a commercial encoding probe. This option is particularly well suited to remote experiments involving flow through a microfluidic chip, as the coil provides excellent homogeneity for planar regions [94]. Example 2D remote detection images (of a serpentine microfluidic mixing chip) taken using this encoding coil are shown in Figure 3.10. These data demonstrate that high-resolution remotely detected imaging may be performed using low-cost probes for both encoding and detection. While these images suffer somewhat from a lack of sensitivity (and artifacts from fluid within the capillary connected to the outlet of the chip), they are intended to serve only as a proof of principle for the encoding coil, which could be greatly optimized in future experiments.

The choice of surface coil shape and design is simple and easily adaptable. For the probe described here, copper was plated onto a PTFE-based substrate (PolyFlon) to form a rectangular loop with dimensions comparable to our microfluidic chip holder. The probe circuitry is identical to the microcoil circuit in Figure 3.7 (here, a 0.6 - 10 pF variable capacitor was placed in series with the inductor to facilitate the process of tuning the circuit to an appropriate resonance). A semi-rigid coaxial cable (Micro-Coax) extends from the bottom of the magnet, along with two G10 Garolite rods (McMaster) for tuning and matching of the circuit through adjustment of the variable capacitors. A circular platform is held several inches below the bottom of the probe with threaded rods, serving to stabilize and position
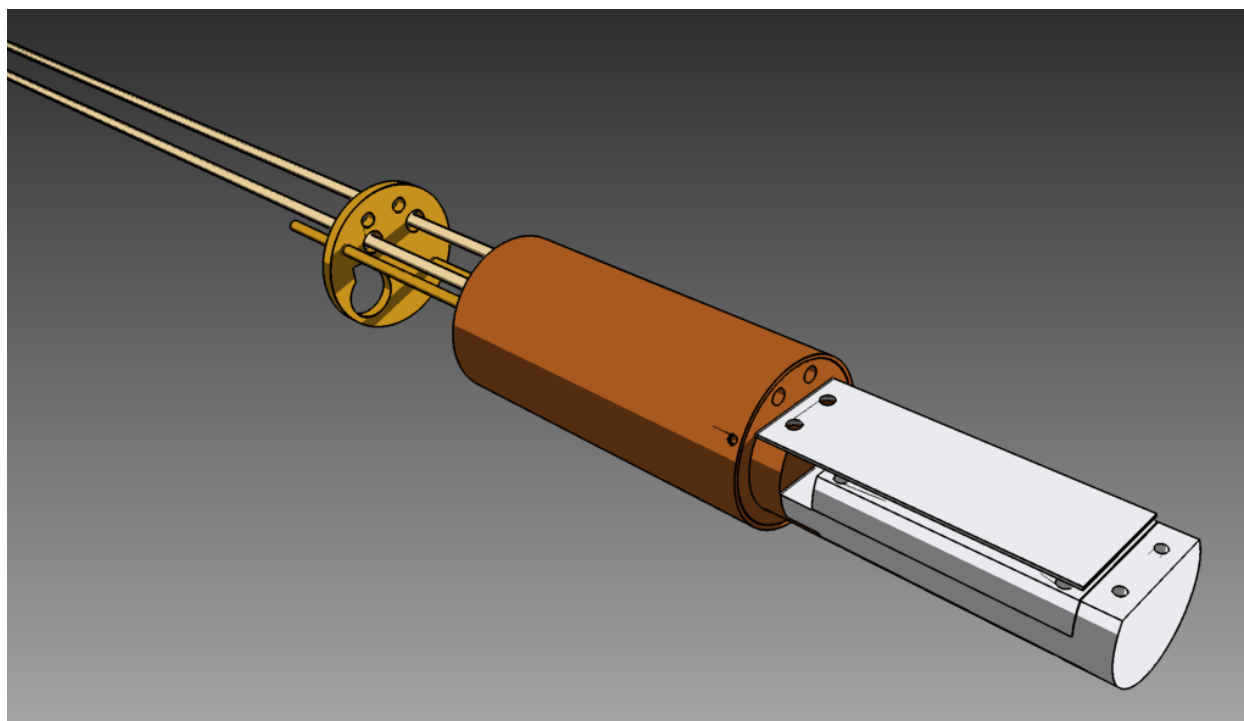
Figure 3.8: Illustrated CAD rendering of the surface coil encoding probe.
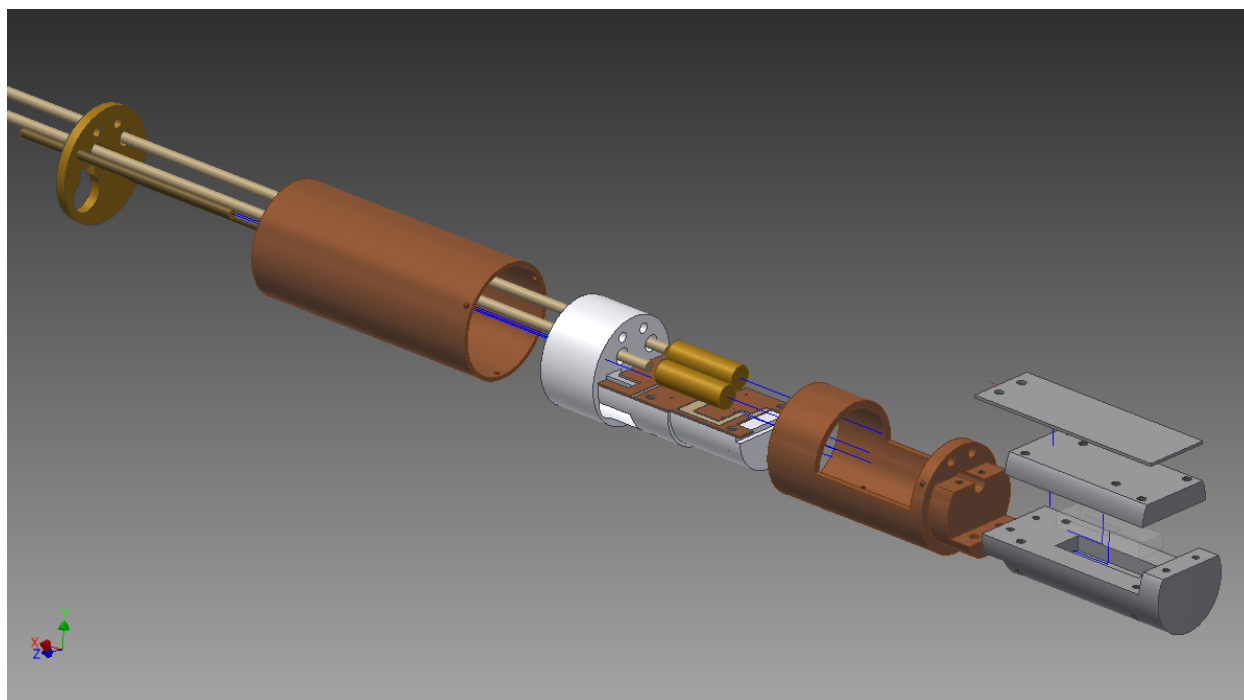
Figure 3.9: Exploded view of the surface coil encoding probe.

the cable and rods. The surface probe shield is designed to attach directly to the microfluidic chip holder component of the remote detection probe, and the outer shield can be easily removed to provide access to the circuit for any necessary adjustments. In conjunction with the microcoil detection probe, the surface coil probe allows one to construct an inexpensive, fully integrated system for both encoding and detection in remote experiments.

3.4   Data Processing

Data acquired with a remote detection sequence can have large dimensionalities, depending on the chosen pulse sequence. For instance, a 3-dimensional velocity encoded experiment will have 5 dimensions: spatial, velocity, and time-of-flight. In order to properly process and visualize these data we make use of a suite of customizable Matlab scripts which perform some variant of the following procedure.

First, the raw data file is loaded into an array and reshaped according to the dimensionality of the experiment. If desired, the direct dimension (FID) of each acquisition may be apodized by a decaying exponential prior to application of the complex Fourier Transform. A sum is carried out across the peak of the direct dimension (now the spectrum) in order to obtain the complex-valued intensities for every point of the indirect dimensions (time-of-flight, phase encoding, velocity encoding). In the case of an image, the data now consist of multidimensional k-space data for each TOF point. These data may be apodized with a Gaussian function centered at $k = 0$, and then subjected to a multidimensional Fourier Transform to yield the image at each TOF. The image data may then be visualized at each TOF point as 1D profiles, 2D images (or slices), or 3D isosurface plots, depending on the

TOF $\longrightarrow$ Sum
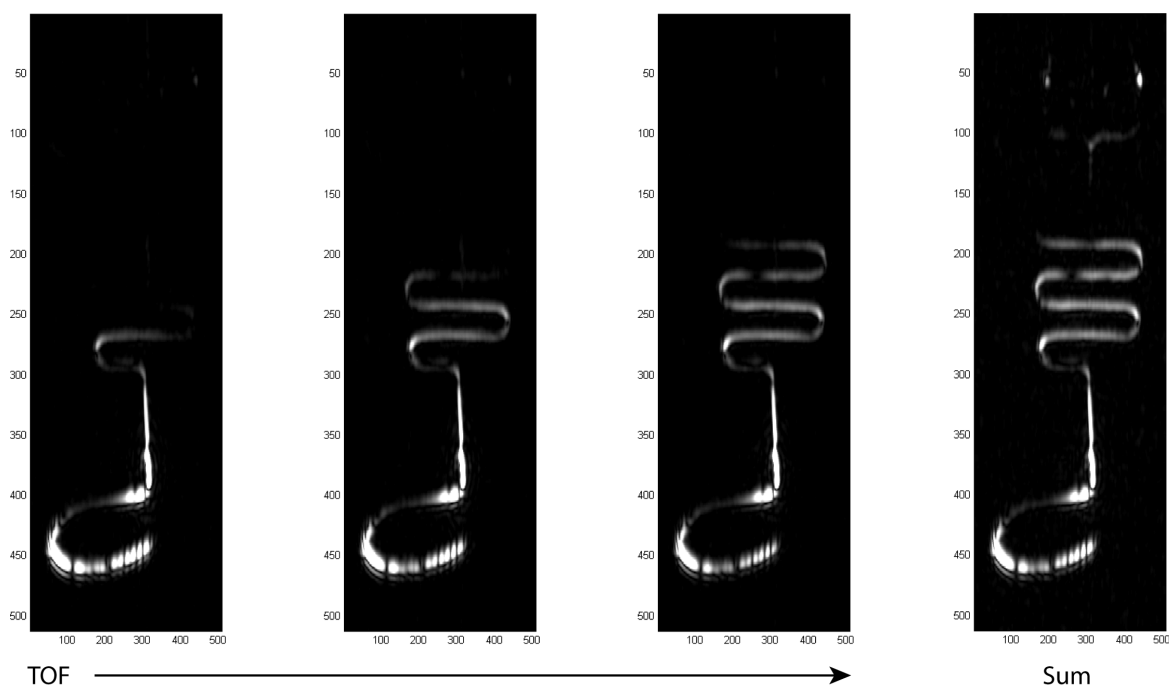
Figure 3.10: 2D remotely detected time-of-flight and sum images encoded with the modular surface coil probe and detected with the auxiliary microcoil probe. Images are taken at 256×256 resolution, with 8x subsampling.

dimensionality of the phase encoding. To obtain the combined image from all encoded spins, a sum may be carried out across the TOF dimension. An example of a 2D TOF-resolved remote detection image of a serpentine mixing chip is shown in Figure 3.10, illustrating the additional insight that can be gained from the time-of-flight dimension, as well as showing the sum image representing all encoded spins. Further remote detection images can be found in Chapters 4 and 5.

An additional dimension will be present in a typical velocity encoded data set, containing two experiments carried out with opposing velocity-encoding gradients. The phase difference between these two experiments is determined for the complex points at each voxel, and is then used to directly calculate the velocity components of interest. If the velocity-encoding gradient is sampled in steps, an additional Fourier Transform across this dimension (q-space) will yield the velocity distribution within each voxel.

If the T_2 encoding delay is used, an indirect dimension will contain each increment of the delay. Following the typical data processing, the intensity of each point can be fit along this dimension with an exponential decay corresponding to T_2 relaxation, yielding decay constants for each voxel in an image or for the bulk sample as a whole (no phase encoding performed).

3.5 Subsampling & Compressed Sensing

While there are many notable advantages of remotely detected experiments, speed has traditionally not been one of them. In typical imaging experiments, a read-out gradient can be applied along one of the dimensions, greatly reducing the acquisition time. Unfortunately, the nature of remote detection requires point-by-point acquisition of k-space, which can be extremely time-consuming. In the case of an experiment with a 3 s travel curve, a 32×32 resolution image will take 3 seconds $\times 32$ (points) $\times 32$ (points) $\times 4$ (phase cycles) ≈ 3.4 hours. For 3-dimensional images or velocimetry experiments, these lengths can become prohibitive. One way to approach this problem is to consider the idea that not all k-space points are created equal, and that we may be able to find a way to reduce the number we sample and still obtain a nearly-perfect image at the original resolution.

To this end, a great deal of recent work [110][6][145] has focused on the application of subsampling and compressed sensing techniques to remote detection experiments. While the mathematical details of this procedure are beyond the scope of this work (see the previously cited references as well as ref. [89] for a more detailed explanation), the basic concept is as follows.

Data from MRI experiments are typically considered in two conjugate domains: real space and k-space. The data within each domain are represented by a series of coefficients, which give a value for each point in that space. In real space, these coefficients simply give the intensity at each point in the image. In k-space, they correspond to the complex data point we obtain from each remote acquisition. The trick to compressed sensing is to find a domain where these coefficients are sparse, meaning that a significant fraction of them do not end up contributing much to the image. If we find one of these domains to represent our image in, there is a good chance that subsampling and compressed sensing can be applied.

For remote subsampling experiments, sparsity can often be achieved in the wavelet domain. Wavelets are oscillatory functions with finite durations. These functions can take a wide range of forms, and the choice of wavelet basis is a detailed topic in itself. Suffice it to say, data can be represented in a wavelet basis, with low-frequency wavelets corresponding to slowly-varying parts of the image, and higher-frequency wavelets filling in the detail. Once a sparse domain has been identified for the data, compressed sensing experiments become viable.

The first step in performing these experiments is to determine which points to sample. While a random distribution of k-space points is an option, a better choice is a sampling schedule that retains random selection but is weighted to favor points near the center of k-space. This is usually accomplished by finding a Gaussian function or, more commonly, a sum of two Gaussians, where one is sharp and narrow near k = 0 and the other is more diffuse, giving some additional weight toward high-frequency points. An example sampling mask for an image with 256×256 resolution and 16x subsampling is shown in Figure 3.11.

Once the subsampled data has been acquired (in k-space) it can be transformed to the sparse wavelet domain. There, a reconstruction algorithm is applied, which minimizes the l_1-norm of the sparse representation (the sum of the sparse coefficient magnitudes) while attempting to keep the subsequent image transformation of these data consistent with the actual experimental data. The algorithm continues to minimize the l_1-norm until the optimized data agree with the collected data to within a specified tolerance. For further details
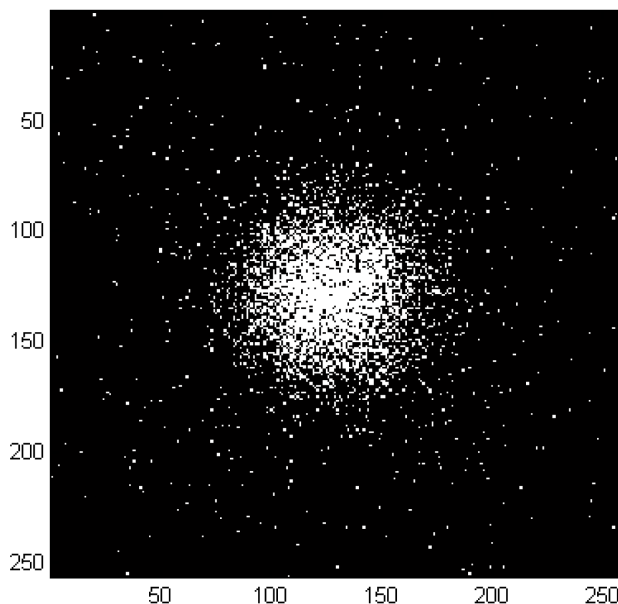
Figure 3.11: Subsampling mask for a 2-dimensional image with 256×256 resolution and 16x subsampling. As discussed, the random sampling is Gaussian-weighted toward the center of k-space.

on the selection of the sampling schedule and the sparse reconstruction process, please refer to [110] and [109].

By using subsampling and sparse reconstruction, remotely detected experiments can be carried out with dramatic reductions in length. As described in the previously cited works, high-quality reconstructions can be performed at subsampling factors up to 8x or beyond (particularly if one incorporates prior knowledge of the spatial extent of the image, as described in [145]). Armed with these tools, the 3.4 hour experiment mentioned above can be accomplished in 25 minutes (at 8x subsampling) with only minimal loss in quality. Experiments which would have been infeasible without compressed sensing (such as the 3-dimensional velocimetry experiments of Section 4.3.2, which would have taken over a week for full data collection) can now be performed in a practical amount of time, providing unprecedented high-resolution insight into microscale flow dynamics.

Chapter 4

Remotely Detected MRI Velocimetry in Microporous Bead Packs

This chapter contains material previously published in reference [47], which has been reproduced here with the consent of its co-authors.

4.1   Introduction

Nuclear magnetic resonance spectra of liquid samples are profoundly sensitive to both coherent and incoherent motion of the constituent spins [44][2]. Further, through their dependence on the average local molecular environment, NMR spectra can directly encode information about chemistry and chemical dynamics in multiphasic or multicomponent ensembles without labeling or perturbative modification of the analytes. Finally, NMR, in combination with spatially varying magnetic field gradients, provides chemically rich images deep within optically opaque structures, materials, and organs. These advantages of MRI over other dynamical fluid imaging techniques [1][3][67] explain why MRI remains a vital technique in applications as diverse as clinical angiography and oil well logging.

A wide variety of NMR methods have been developed in order to probe fluid properties within macro- and mesoporous materials. The majority of these studies report ensemble properties of the flow, including diffusion, relaxation, and the flow propagator [19][131], averaged over the extent of the macroscopic sample. While these studies have provided information about dispersion [126][68][61], surface relaxivity [60], wettability [58], permeability [7][105], pore size [84][91][130], and velocity [126], they typically cannot directly localize features of the flow within the larger sample, because the fraction of the enclosing detector volume occupied by the sample is so small. Efforts to spatially resolve flowing fluids [32][63][76][122][121] in porous media are thus limited in their resolution, necessitating the use of larger representative model systems and often employing voxel sizes on the order of or larger than the pores themselves. These difficulties act to conceal the intricate pore distributions and flow properties found in complex porous samples at relevant scales.

Our particular interest is to expand the capabilities of MRI flow imaging to a regime of microscopic detail for which the inherently low sensitivity renders it poorly suited. The microscopic details of a macroscopic object might be most sensitively imaged if one could
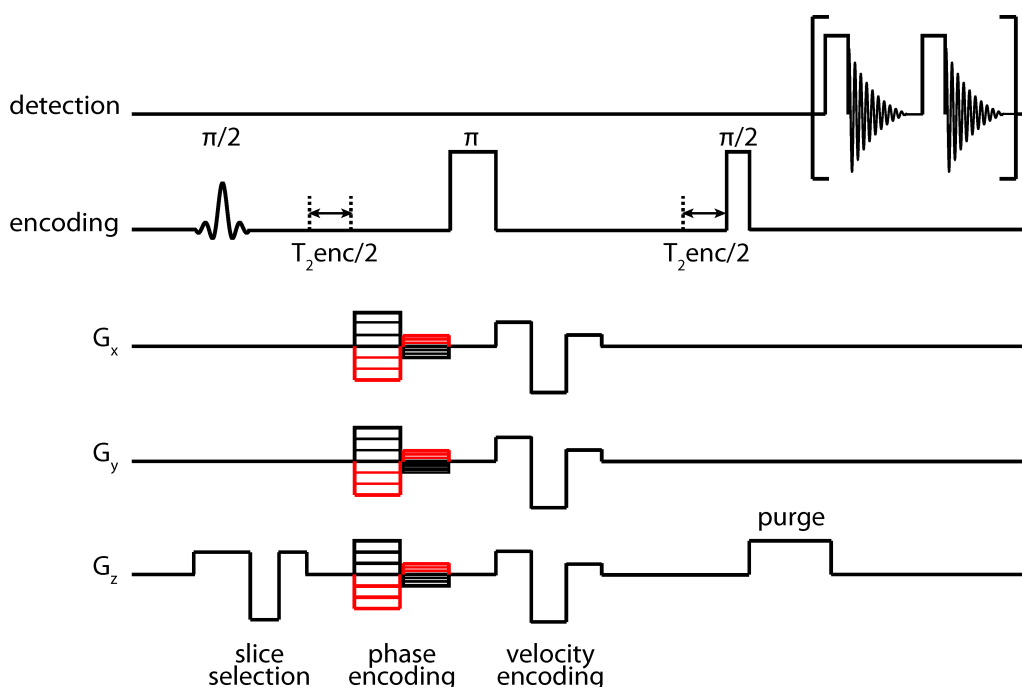
Figure 4.1: Pulse sequence for multidimensional remotely detected imaging experiments, with optional velocity and relaxation encoding steps, as described previously in Section 3.2.

implant, within it, NMR detectors that precisely enclose each feature of interest. This is, however, impractical in most cases and impossible in systems whose internal structures are intrinsically inaccessible to a local detector. We instead employ remote detection [98][40], a technique that spectroscopically mimics the implantation of a volume-matched detector around a microscopic feature [6].

While the background of remote detection has been covered in detail in Chapter 3, a quick, relevant description will be given here. In remotely detected MRI, conventional MRI phase encoding sequences are applied to encode velocimetric, chemical, and spatial information into the spin degrees of freedom of the flowing analyte using an encoding coil that contains the entire sample. Next, the information is stored as longitudinal magnetization (intensity along the applied field) for travel to an optimized microsolenoid detector at the sample outflow. Within the detector, the information is read out stroboscopically and the data reconstructed by simple Fourier transformation, yielding not just an image but also a correlated time-of-flight dimension that reflects fluid transport from the encoding region to the detector. The order of arrival of the fluid packets is independent of spatial encoding and therefore does not influence the appearance of the image. Because the volume of the microcoil is approximately matched to the volume of the voxels in the imaging experiment, we realize a dramatically enhanced filling factor for detection; further, because we detect the fluid in an environment free from magnetic susceptibility broadening, we obtain excellent linewidths. Combined, these improve the sensitivity by up to several orders of magnitude compared to conventional imaging in a similar geometry [41].

In other studies, we have applied remote detection in flow imaging and velocimetry of

liquids within microfluidic devices [6][54][95][51][52] and membranes [146], as well as gas flow within macro- [123] and meso-porous [50] materials (including the monolithic chromatography columns of Chapter 5). Here, we extend the method to flow imaging, velocimetry, and relaxometry of liquid flow within porous bead packs, an initial application of remotely detected velocimetry techniques outside the realm of regular microfluidic flow. In addition to their use as microreactors, such bead packs are ubiquitous model systems for many investigations of flow in porous media, including rocks, sand, membranes, and biofilms. We acquire images of water flowing through packed beads with diameters ranging from 150 to 600 μm, obtaining spatial resolutions as low as 45 μm, smaller than in any previous porous media MR imaging experiment. To record these images, we employ MRI experiments that measure flow and diffusion through the application of magnetic field gradient pulses that render the NMR phase sensitive to position or velocity alone [19]. A series of such experiments with velocity encoding gradients applied along orthogonal axes reconstructs a Eulerian vector flow field. Since the spatial resolution of all MRI images is limited by the nonrefocusable dispersion during the encoding time, we use gradient moment nulling methods to compensate for the deleterious effects of spin motion (see ref [113] and Section 3.2.3).

An example of a remote detection pulse sequence with velocity encoding is shown in Figure 4.1. In the context of a spin echo sequence, our experiment begins with slice selective excitation, which is followed by spatial phase encoding, optional velocity or T_2 encoding, storage along the longitudinal axis, transport to the microcoil detector, and stroboscopic detection. For a detailed explanation of remote imaging and velocimetry experiments, as well as a schematic of the remote detection experiment, see Chapter 3 as well as the supporting material for ref [6].

4.2 Experimental Methods

4.2.1 Bead Pack

The packed bead flow systems were contained in enclosing Teflon cylinders with microfluidic connectors on each end (Upchurch Scientific). The diameters of the coarse and fine bead pack bores were approximately 2 and 1.6 mm, respectively. The bores were filled with glass beads (Sigma-Aldrich) with diameters ranging from 150 to 212 μm for the fine pack and $425 - 600$ μm for the coarse pack. While the beads were not fixed by sintering or chemical adhesion, our relatively slow flow rates ensured that they were not fluidized and that they reached equilibrium positions in a very short time. Following passage through the porous encoding region, fluid traveled to the microcoil detector through a short length of 150 μm ID PEEK microcapillary tubing, driven by regulated, pressure-based flow. For the high-resolution experiments with dimensions of $64 \times 64 \times 64$ (16-fold subsampled, as described in Sections 3.5 and 4.2.4), we attained a voxel size of 54 μm $\times$ 54 μm $\times$ 89 μm for the coarse bead pack (FOV$_{x,y}$ = 3.45 mm, FOV$_z$ = 5.72 mm) and 45 μm $\times$ 45 μm $\times$ 53 μm for the fine bead pack (FOV$_{x,y}$ = 2.90 mm, FOV$_z$ = 3.40 mm).

4.2.2 Experimental Setup

The remote detection experiments were performed with a 7.05 T Oxford Instruments wide bore magnet and a Varian imaging console. Excitation and storage pulses were performed with a 40 mm Varian volume imaging probe, while gradients were applied using a Varian triple-axis gradient system producing up to 100 G/cm on all three axes. The detection probe was a custom-built microcoil probe (with schematics given in Appendix A.1) connected to the capillary tubing via commercially available connectors (Upchurch Scientific). Water flowed through the system at constant pressures of 18 and 50 psi (coarse and fine bead packs, respectively), driven by a nitrogen gas ballast system and monitored by a proportional control setup (Omega Engineering).

4.2.3 Pulse Sequence

The pulse sequence for remote detection (shown in Figure 4.1) consisted of a slice selective $\pi/2$ excitation (typically, a sinc pulse with 5 kHz bandwidth), followed by two- or three-dimensional phase encoding $(1 - 1.5$ ms). Slice selection and phase encoding gradients were balanced in order to cancel phase evolution due to motion of the spins [113]. Refocusing of transverse magnetization occurred via a π pulse, and a final $\pi/2$ pulse was applied after the proper echo delay in order to store the encoded magnetization along $\hat{z}$ for transport to the detection coil. When used, two- or three-lobe velocity-encoding gradients, designed to null the phase accrued due to the position (and, if three-lobed, the acceleration) of spins and encode only the velocity, were applied before the storage pulse, with a total duration of $1 - 1.5$ ms. T_2 encoding was performed via a set of experiments with an additional delay symmetrically incremented about the refocusing pulse. Phase cycling was employed to store each component of the magnetization and to filter out any signal from spins outside of the encoding region.

4.2.4 Subsampling

Compressed sensing methods were used in the acquisition of the three-dimensional data sets, following a methodology detailed in a previous work [110]. In brief, k-space sampling took place according to a predetermined subsampling mask, chosen to give an accurate representation of the data after transformation and reconstruction in a sparse wavelet domain. Experiments with 32 μm $\times$ 32 μm $\times$ 32 μm resolution used a k-space mask with 8-fold subsampling ($\sim$ 12 h acquisition time), while the data taken with 64 μm $\times$ 64 μm $\times$ 64 μm resolution were subsampled by a factor of 16 ($\sim$ 55 h). For further details regarding the generation of subsampling masks, transformation between k-space, real, and sparse domains, and reconstruction, please see [109], [110], and Section 3.5.

4.2.5 Data Processing

For a more general treatment of the remote data processing procedure, please see Section 3.4. All data were processed using Matlab (Mathworks). Following apodization and Fourier
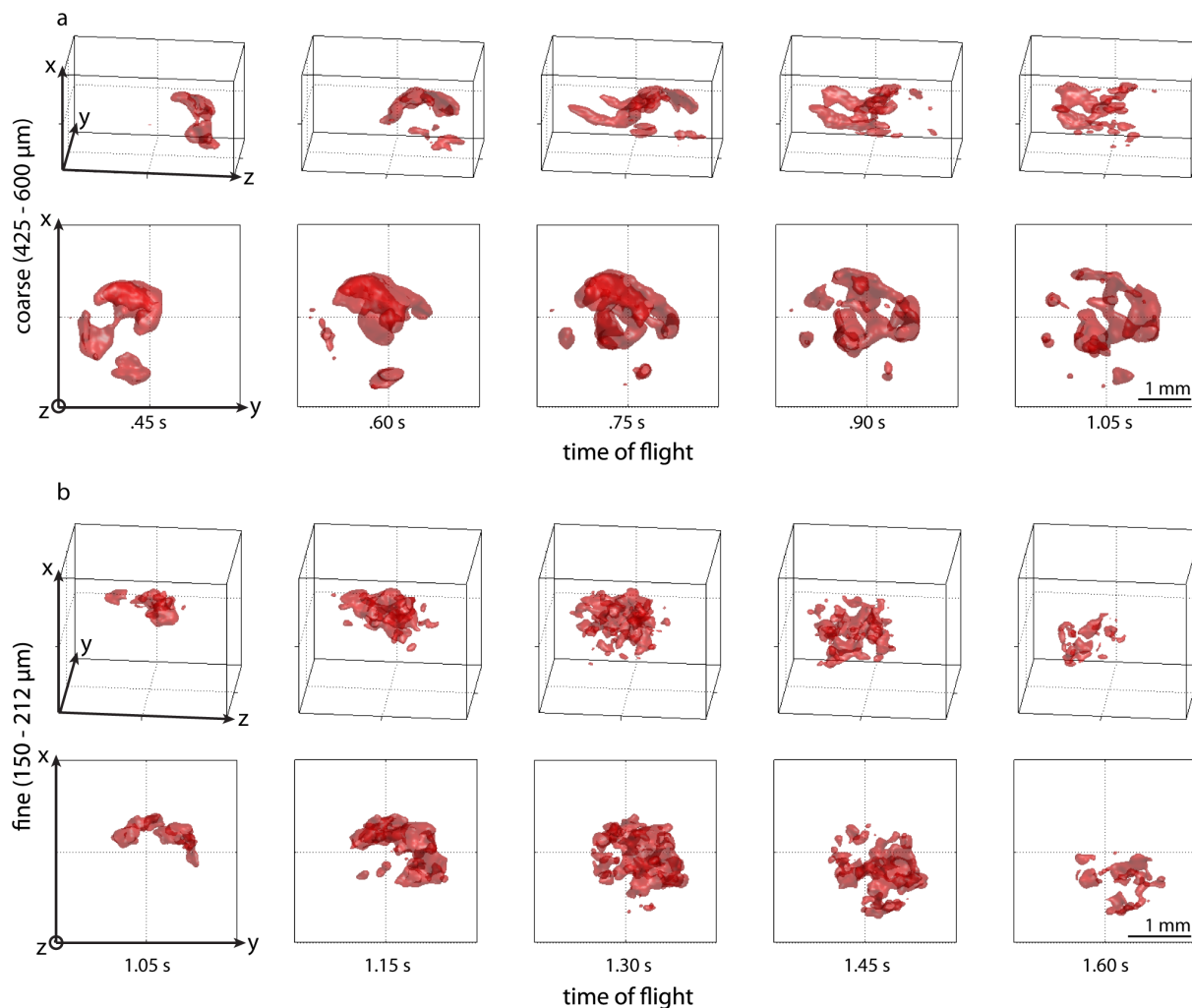
Figure 4.2: High resolution time-of-flight images of flow through both coarse (a) and fine (b) bead packs. 3D isosurfaces of signal intensity are shown at five representative TOF points, in both isometric and axial points of view. The imaging resolution was $64 \times 64 \times 64$ with 16-fold subsampling, yielding voxel dimensions of 54 μm $\times$ 54 μm $\times$ 89 μm for the coarse bead pack ($\text{FOV}_{x,y} = 3.45$ mm, $\text{FOV}_z = 5.72$ mm) and 45 μm $\times$ 45 μm $\times$ 53 μm for the fine bead pack ($\text{FOV}_{x,y} = 2.90$ mm, $\text{FOV}_z = 3.40$ mm).

transformation of the direct dimension, the water resonance is integrated to obtain complex-valued data for the indirect phase-encoded dimensions of the experiment. For data acquired with compressed sensing, the images are first reconstructed by a nonlinear L1 minimization scheme that seeks to maintain the agreement of the image model with experimental data and maximize the sparsity of the image model that agrees with the experimental data [89]. All of the acquired data sets are apodized by Gaussian functions centered at the origin of k-space, zero-filled by a factor of 3, and transformed by a multidimensional Fourier transform to obtain the complex image.

Images containing a velocity-encoding dimension were processed as described above, followed by determination of the phase difference between two images taken with velocity gradient pulses of opposite sign, to yield velocity data. The repetition of this procedure along three orthogonal axes yields a Eulerian (vector) flow field in each voxel. All image information is also correlated to a Lagrangian description of the flow, expressed in the particle frame by the correlated time-of-flight dimension. T_2 values were obtained by fitting a monoexponential decay in each voxel to a series of experiments with incremented T_2-encoding delay. Velocity and T_2 data were masked by eliminating voxels with signal intensity less than the maximum intensity multiplied by a cutoff value.

4.3   Results

4.3.1   Time-of-Flight Images of Flow

We obtained high-resolution time-of-flight images of flow through both coarse ($425 - 600$ μm diameter) and fine ($150 - 212$ μm diameter) bead packs at 64 μm $\times$ 64 μm $\times$ 64 μm resolution (with 16-fold subsampling). Surface plots of the fluid distribution within coarse (Figure 4.2a) and fine (Figure 4.2b) bead packs are shown in isometric and head-on views for five representative time-of-flight points. Fluid flows from left to right, with liquid closest to the bead pack outlet, or liquid following comparatively rapid flow lines, arriving first at the detector. As longer TOF points are sampled, we see flow from regions farther from the outlet and from areas with slower or more restricted flow. Fluid from stagnant flow regions may not reach the detector before spin-lattice relaxation erases the encoding information, and therefore, our time-of-flight images may understate their contribution to the overall flow dynamics. The void space within the remote images may correspond either to the beads themselves or to areas with slow-moving flow. The beads themselves do not contribute to the flowing signal, and therefore, their positions cannot be directly inferred.

4.3.2   Velocity-Encoded Images

MR images can be sensitized to motion by the addition of magnetic field gradient waveforms that cause signal phase to depend on velocity, while nulling its dependence on position or acceleration. This has been previously demonstrated in remote detection experiments performed with micro-fluidic devices [6]. The phase generated by motion of nuclei through these gradients allows for direct measurement of each velocity component, when normalized to a control experiment in which the sign of the gradient lobes has been inverted. In Figure
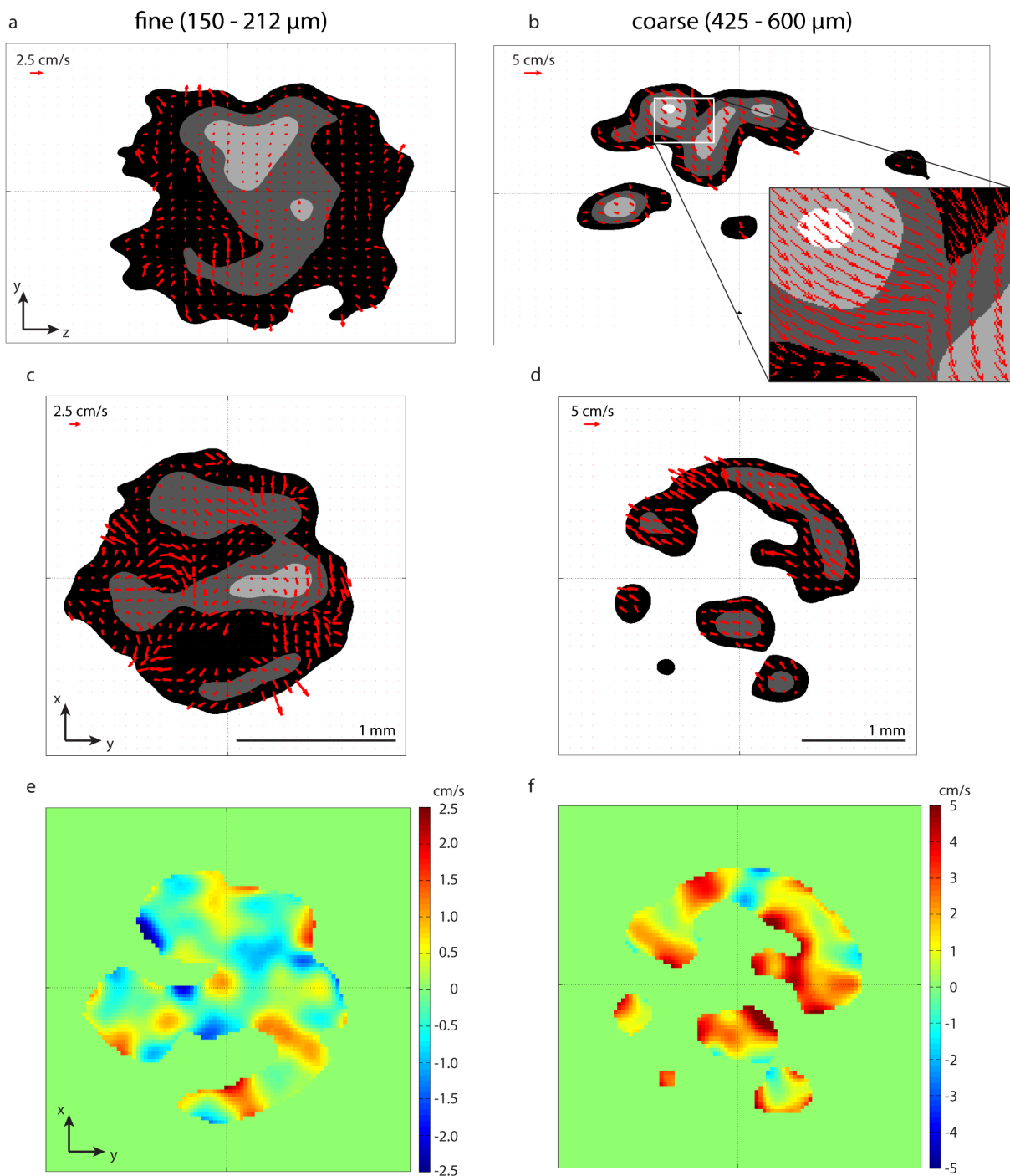
Figure 4.3: Selected 2D slices of the 3D velocimetric data for each bead pack. Intensity contours are drawn parallel (a, b) and orthogonal (c, d) to the direction of flow for a selected time-of-flight point in each data set, and overlaid with 2D in-plane velocity vectors. The velocity component along the direction of flow (V_z) is shown for the chosen axial slices in parts e and f.
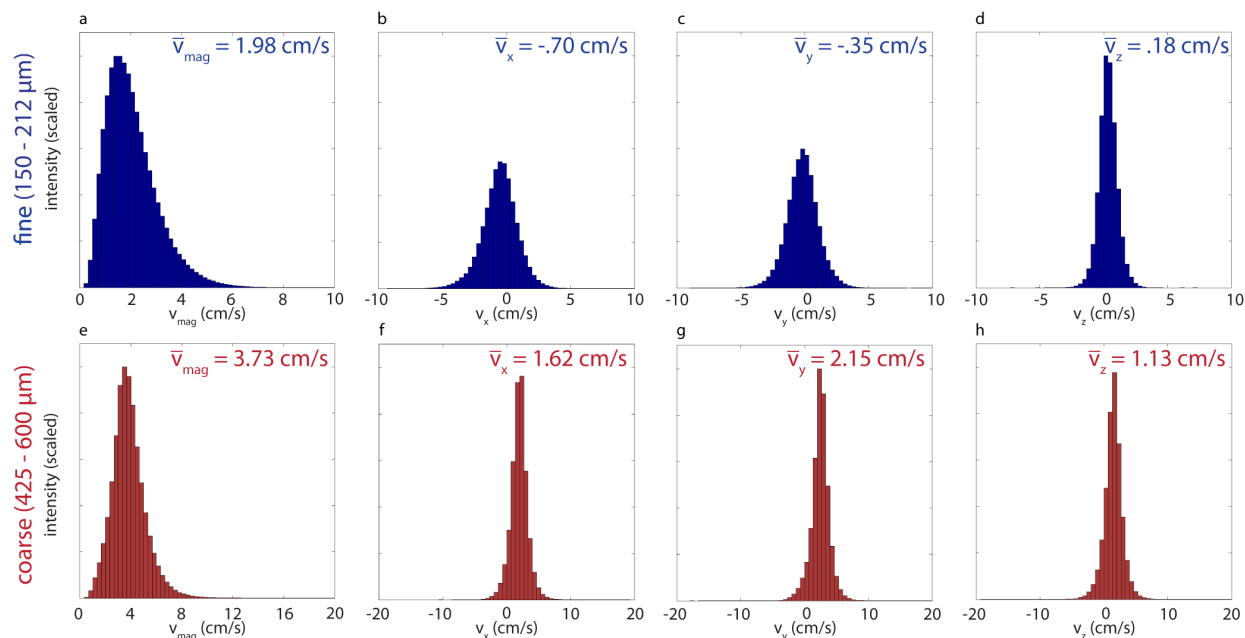
Figure 4.4: Intensity-weighted histograms for each velocity component and the overall velocity magnitude, for fine (a-d) and coarse (e-h) bead packs. Average velocities for each histogram are noted, and the overall intensity of each bin is scaled to the maximum bin within its respective bead pack. Weighting each velocity by the signal intensity in that voxel serves to correct inaccuracies due to variations in fluid density.

4.3, we show several two-dimensional velocity plots for a single time-of-flight, in both coarse and fine bead packs. In parts a and b, we see contour plots chosen so that the slice is in the xz-plane, parallel to the direction of flow, with two-dimensional in-plane velocity vectors. Axial (xy) slices from the same time-of-flight are shown with transverse velocity vectors in parts c and d, while the z-component of velocity is shown in parts e and f.

While the velocity vectors are generally inclined toward the direction of flow in both bead packs, the distribution of flow in the fine bead pack is far more complex. The axial V_z plot shows substantial regions of retrograde flow, while the parallel plot illustrates large regions of circulatory flow. By contrast, flow through the coarse bead pack is quite straightforward and is primarily confined to several large flow paths. Due to the irregularity of the bead structure, the flow pathways are not necessarily symmetric about the axis of flow. As can be seen in Figure 4.2, fluid in the fine bead pack undergoes a net displacement along the x-axis while the distribution in the coarse bead pack clearly shifts along the y-axis, observations which are confirmed and characterized by examining per-voxel distributions of velocity.

In Figure 4.4, we show histograms of velocity distributions for both coarse and fine bead pack data. The complex velocity-encoded images were summed over the time-of-flight dimension (for points containing encoded spins), and the phase difference was found for each voxel. Finally, the data were weighted by the signal intensity for each fluid-containing voxel. The amplitudes of the velocity component histograms are scaled to the largest bin for their respective bead pack. In the coarse bead pack (red, bottom row), the distributions for V_x (f) and V_y (g) are noticeably shifted toward a nonzero mean, consistent with asymmetric

flow pathways discussed above. The distribution of flow pathways in relevant porous media samples is likely to be similarly nonuniform, and the combination of velocity data (Eulerian) and time-of-flight images (Lagrangian) is particularly well-suited to elucidate irregular flow pathways.

In parts d and h, we show the fine and coarse bead pack velocity histograms for V_z, the component along the flow direction. The nonzero mean corresponds to a net movement of spins in the direction of flow, although the distributions also include negative velocities which may indicate the effects of reversed flow and recirculation [76], dispersion, and tortuosity.

The histograms of velocity magnitude are shown in parts a and e. When comparing the widths of the histograms relative to their means, the fine bead pack histogram demonstrates a wider range of relative velocities, as would be expected for the increased dispersion within the smaller pore network. However, further conclusions regarding the comparative velocities within each porous region cannot be easily drawn in these circumstances, due to the differences in phantom construction and experimental conditions.

4.3.3 T_2-Encoded Images

A separate series of three-dimensional experiments involved an incremented T_2-encoding delay applied symmetrically about the refocusing pulse, as indicated in Figure 4.1. We fit the T_2 decay curves for each voxel using experiments with additional T_2 encoding delays of 0, 3, 6, and 9 ms (on top of the $2-4$ ms remote encoding period), shown in Figure 4.5 for three slices within a single time-of-flight in both coarse ($425 - 600$ μm diameter) (a) and fine ($150 - 212$ μm diameter) (b) bead packs. The T_2 values typically vary from 1 to 20 ms, and are generally smaller within the fine bead pack. While our goal is to demonstrate that the remote detection experiment is well-suited to measure T_2 relaxation, analysis of the underlying factors and their relative significance is not straightforward, and our discussion below will be limited to a short overview of these concerns.

4.4 Discussion

Previous studies of flow within porous media have established that there is a large heterogeneity in fluid and velocity distributions. Some pores exhibit evidence of stagnant flow, while others contain fluid flowing with velocities several times greater than the bulk flow [32][122]. A relatively small fraction of pores may conduct a significant fraction of the fluid [121]. Variations in fluid channeling and velocity distributions within porous media arise from a combination of the effects of local pore structure and the overall topology of the porous network. Because of these channeling effects, the fluid shown in Figure 4.2 may, in the extreme case, represent only the primary pathways which allow for rapid, relatively unobstructed flow. Fluid trapped in obstructed or stagnant regions may not travel to the detector in a time shorter than the phase memory of the spins, making it difficult to distinguish between stagnant regions, from which encoded flow never reaches the detector, and the glass beads, from which flow is excluded. Thus, our inability to apply direct imaging at this scale restricts us from obtaining a void-space image of the bead pack.

However, it is impossible to apply conventional MR imaging methods with pore-scale
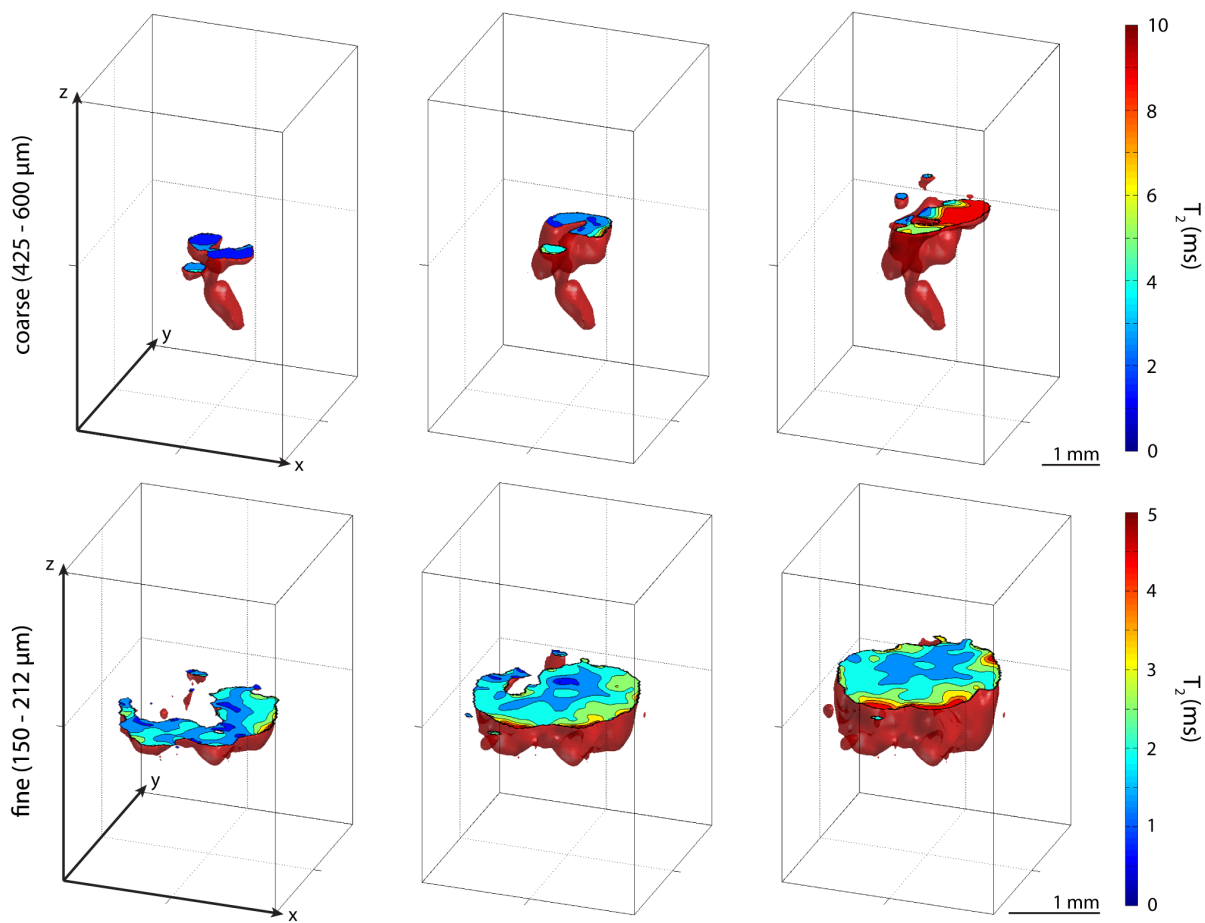
Figure 4.5: T_2 relaxation data for fluid flow within coarse and fine bead packs, as indicated adjacent to the figure axis labels. Isosurface contours of the flow volume are shown for a single time-of-flight, truncated at three representative planes within the sample in order to illustrate the relaxation values within the pore structure. Relaxation values were obtained by performing a per-voxel fit of signal intensity for a series of images with incremented T_2-encoding delays.

resolution in many interesting porous media. Most porous media and the flows they conduct are far less homogeneous and regular than any model bead pack, both in structure and fluid composition. While the dynamics of monophasic flow through a stationary bead pack scale with the dimensionless Reynolds number, multiphasic flows obey more complex scaling laws; experimental models, therefore, that simply scale their dimensions to the point where conventional MRI can be applied will fail to capture the relevant fluid dynamics. Further, many materials for which MRI might be useful, such as microporous rocks, membranes, or aerogels, either occur naturally or are synthesized with a pore scale that is relevant for their function and cannot be emulated by a model system. Remotely detected MRI allows us to avoid these tenuous scaling conversions by performing experiments directly upon the sample of interest (although the efficiency of the experiment may be compromised when examining very slow flow within naturally occurring porous media). Even in systems with larger pores, in which direct imaging can be applied, remote detection is able to provide a complementary time-of-flight (Lagrangian) view of the flow field.

In microporous systems, ours is one of the few methods that can provide simultaneous and correlated descriptions of the flow field in terms of Eulerian local velocities and Lagrangian times of flight. Statistical analyses of the velocity distributions show that fluid within the fine bead pack has a wider distribution of velocities (relative to the distribution mean), consistent with a greater level of dispersion within the more tightly packed phantom. The velocimetry data indicate the significant presence of dispersive and retrograde flow, particularly in the fine bead pack. This behavior is clearly illustrated by the large regions of negative axial flow in Figure 4.3f, the circulatory behavior of the flow vectors in Figure 4.3d, the increased relative histogram widths, and the significant number of negative velocity components in the histograms.

In addition to the advantages in scale and flexibility already described, remotely detected velocimetry is less susceptible to inaccuracies in measured data. Specifically, partial volume effects can arise when the size of an imaging voxel is comparable to the pore size or even larger [32]. In that case, the phase accrued in each voxel is the intensity-weighted, phase space geometric sum of all components within the voxel and not the average velocity in the voxel. Remote detection allows us to use much smaller imaging voxels and is additionally sensitive only to flowing spins, with the result that the experimentally determined phase contrast more accurately reflects the mean velocity of flowing fluid within each voxel. In our measurements, for example, the velocities within the coarse bead pack should be largely free of partial volume effects, as the voxel dimensions are at least a factor of 2 lower than the bead radii. However, average velocities may be slightly overestimated in situations where there are stagnant or very slow moving volumes of flow which do not reach the detector in a reasonable time.

Finally, in addition to obtaining velocimetry data within the porous bead packs, we demonstrate the acquisition of transverse relaxation data. We depict these not as T_2-weighted images but as images in which we have fit the T_2 in each voxel through a series of measurements. There are two primary causes of T_2 relaxation in porous media: surface relaxation due to dipolar interactions [8] and paramagnetic impurities [72], and dispersion through gradients in the internal field caused by the solid-liquid interface throughout the sample [92][156][59][124][29][5][135][157]. In situations where surface relaxation dominates, T_2 can be used as a direct probe of the surface area-to-volume ratio of the pores, and thus a

measurement of the pore size distribution [153]. It should be noted that the effects of magnetic susceptibility heterogeneity increase in proportion to the static magnetic field strength. Therefore, after a certain point, diffusion through the internal field can substantially interfere with the determination of pore size distributions [167]. While a detailed analysis is beyond the scope of our work, we observe several trends. First, T_2 within the fine bead pack is, on average, smaller than in the coarse bead pack. This might be related both to an increase in surface relaxation with smaller pore size as well as to larger magnetic field gradients within the finer porous structure. Similarly, the T_2 map within the coarse bead pack indicates larger T_2 values within larger regions of flow, which could be related to a decrease in the influence of surface relaxation as well as weaker internal field gradients near the pore center and a smaller flow rate through these gradients. Since we performed these experiments at relatively high field, susceptibility gradients are likely to dominate. While a direct (i.e., not remotely detected) measurement of the spatially resolved T_2 values within these bead packs would be a worthwhile comparison, such an experiment would take a prohibitively long time due to the severely reduced filling factor in this microporous sample. However, previous bulk experiments using a saturated sandstone core (with pore sizes of 50 μm or less) have shown discrete T_2 distributions ranging from 0.2 to 32.6 ms [152], in good agreement with our remotely detected values. We further note that remote detection can permit T_2 measurements at arbitrary field strengths (*vide infra*) because the flowing analyte can be polarized in a high magnetic field before it enters the sample chamber, in which it can then be encoded in any given magnetic field.

We have demonstrated a generic method for magnetic resonance velocimetry and imaging of flow within microporous materials. We are presently applying the technique to study multiphasic flow and small molecule separations within microchromatographic columns (Chapter 5), and anticipate its extension to multicomponent systems including microreactors and confined combustion devices [33]. In these experiments, chemical shift information may be encoded in indirect spectral dimensions or detected in the direct dimension after flow to the microcoil, allowing the flow volumes associated with each signal component to be isolated and localized within the porous structure. More importantly, because remote detection separates the polarization, detection, and encoding steps of the experiment, it will enable a new variety of portable flow profiling devices for use in rock core sample characterization and online industrial process monitoring. For example, prepolarization of the fluid can occur in the inhomogeneous field of a permanent magnet, and the fluid can be then transported to a region of arbitrary magnetic field in which spatial and other encoding can take place, after which the result can be detected inductively or by a microfabricated magnetometer that operates without a magnetic field [117][144]. Such a geometry would also provide greater sample access and thus lend itself to multimodal (X-ray computed tomography, optical) imaging schemes.

4.5 Conclusions

We have applied remotely detected imaging, velocimetry, and relaxometry to microporous bead packs. The sensitivity enhancements characteristic to remote detection allow us to perform high-resolution experiments on porous media which would be inaccessible to typ-

ical detection techniques. The combination of time-of-flight and velocimetry data provides complementary views of the fluid flow within the pore structure, and allows for clear visualization of the dominant flow pathways and dispersive fluid behavior. Finally, we probe the T_2 relaxation of fluid within the bead packs, obtaining data which provides further insight into the properties of the complex porous environment.

Chapter 5

Remotely Detected NMR for the Characterization of Flow and Fast Chromatographic Separations Using Organic Polymer Monoliths

5.1 Background

5.1.1 Chromatography & NMR

Chromatography is an indispensable tool for the purification and analysis of complex mixtures, with applications in analytical chemistry, biochemistry, chemical synthesis, drug discovery, and industrial chemical manufacturing [129]. Fundamentally, a chromatographic process involves passing a mobile phase (which carries a mixture of analytes) over a porous stationary phase, facilitating the separation of compounds within the mixture. A diverse range of stationary phases have been developed which can separate solutes based on parameters including molecule size, hydrophobicity, and charge.

Although UV-visible spectroscopy is the most common method of monitoring chromatographic separations in real-time, this mode of detection is dependant upon the availability of well-resolved peaks and chemical standards in order to correlate species as they elute from the column. Mass spectrometry can also be utilized for real-time detection, providing an additional method to confirm peak assignments. However, the chemical information provided through mass spectrometry is limited to the mass-to-charge ratio of the individual compounds, unless secondary processes (i.e. fragmentation) are utilized. While these secondary processes can yield great insight, they do not provide chemical details of the intact molecules in a non-charged state. Additionally, neither detection method is able to perform multidimensional imaging of flow or separations directly on the column.

One powerful alternative to these detection methods is magnetic resonance, which has been used for imaging [9][28][45] and spectroscopy under both stopped [147][85] and continuous flow in-line detection modes [154][155]. At its simplest level, an in-line hyphenated experiment using chromatography and NMR can provide a sensitive look at analyte com-

position after it has traveled through the column. The NMR detection coil is typically positioned at the outlet of a chromatographic column, allowing for continuous monitoring of the effluent. Since any columns placed near the magnet must be free of metal components, fused silica capillaries are usually the preferred format. In contrast to relying on a simple absorption measurement, the use of chemical shift can greatly enhance the resolution and characterization of compounds and mixtures, and examples of hyphenated experiments on larger particle packed columns have been successfully demonstrated within the literature [155][42][78][115]. Further insight can be gained with the pre-existing library of flow-based magnetic resonance experiments, which allow one to perform measurements of properties including velocity, diffusion, and exchange kinetics [140][141][142].

Concurrently, MRI has been used to image the interior of particle based chromatographic columns in order to identify flow inefficiencies, suggest improvements in column design, and visualize separations as they occur on the columns [9][28][45][166]. Although insightful, these studies remain limited due to the low sensitivity and poor temporal resolution of MRI, precluding their application toward the analysis of microscopic flows (such as those exhibited in capillary liquid chromatography [151] or on-chip chromatography [80]). In order to analyze separations and flow properties within microscale chromatographic devices, changes need to be made to the detection scheme.

5.1.2 Microcoil Detection Experiments

Section 1.1.5 has already discussed the sensitivity enhancement that can be achieved by using an optimized microcoil detector with very small volumes of sample. If the experimental needs only require characterization of the analytes following chromatographic separation, this coil can be used for both encoding and detection and can monitor the products of the separation as they flow through a capillary. Previously, Webb and co-workers have used

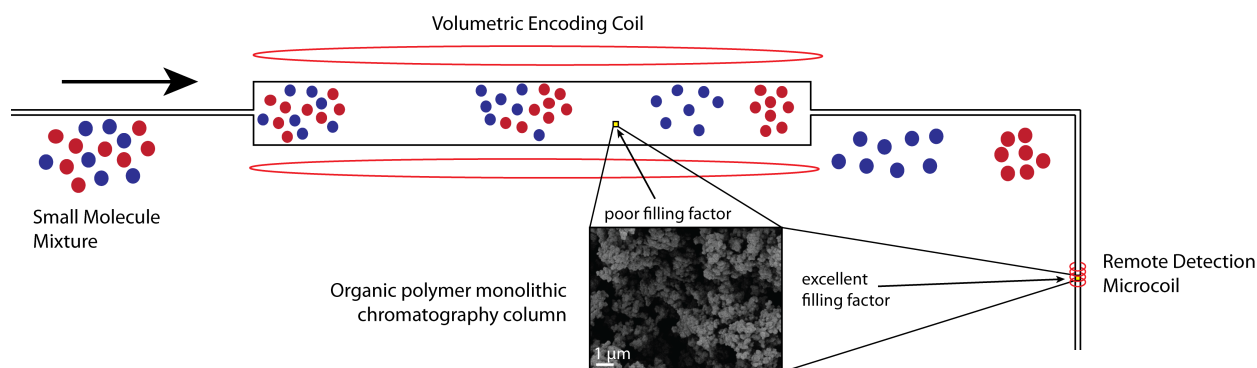Figure 5.1: Illustration of the remote detection experiment, as applied to an organic polymer monolith. The encoding coil, indicated on both sides of the column, encloses the entire volume of the monolith. The microsolenoid detector is wrapped around a capillary connected to the outlet of the column, and provides a sensitivity increase due to greatly enhanced filling factor for a given voxel (shown in yellow).

particle packed columns to demonstrate the in-line monitoring of microscale separations [155][154] with excellent temporal and spectral resolution. Application of these techniques to separations within organic polymer monoliths will be described in Section 5.3.2.

While the aforementioned NMR experiments can be performed by direct measurement with a microcoil detector, they do not provide a way to examine the flow dynamics or separation behavior within the column itself. To gain insight into these areas, the chromatography experiment can be readily adapted to a remote detection framework. This can be easily accomplished by connecting the chromatography column in-line with our remote microcoil detector and positioning the column within the encoding region of the magnet, as shown in Figure 5.1.

The main limitation in running these experiments is the T_1 of the encoded spins. For short T_1 nuclei (such as those used in this study), significant signal loss is observed approximately 5 s after encoding. In order to prevent decay of the stored magnetization, relatively fast flow rates must be used in order to quickly move the fluid from the encoding region to the detector. In spite of this restriction, the previously described gains in spatial and temporal resolution make this technique well suited for analysis of capillary chromatographic separations, provided that the required flow rates can be achieved.

The work described in this chapter makes use of an optimized microcoil detector, in both direct and remote experiments, to characterize monolithic microchromatography columns. First, we apply remote detection methodology toward imaging and velocimetric measurements within the mobile phase of the organic polymer monolith. Through these measurements, we are able to characterize the flow profile and velocity distribution across the column, providing a way to look inside the complex monolithic network and gain access to previously inaccessible information about the flow dynamics. Next, we make use of our microscale flow system to perform in-line monitoring of small molecule separations at very high flow rates. We are able to demonstrate clear, well-resolved separations of small aromatic molecules at conditions far beyond the norm. Finally, we describe ongoing work to apply remote imaging and velocimetry techniques to probe chromatographic separations as they are occuring within the column. Through this collection of experiments, we are able to demonstrate the unique power of magnetic resonance, both direct and remote, in studying organic polymer monoliths and microchromatographic separations.

5.1.3 Packed Particulate Chromatography

The standard way to create a porous stationary phase is to use a tightly packed, typically micrometer-sized, particulate material (such as silica) which mediates the separation through interactions with the dissolved analytes. Packed columns have been in wide use for over 100 years, and form the basis for the majority of modern commercially available chromatographic devices. While the analytical power and scope of application using packed columns should not be understated, there are a number of notable limitations to the technique.

Due to the particulate nature, the porous network of a packed column will have a large amount of interstitial void space (which can be visualized as the cavities created between spheres in an idealized packing scenario), as shown in Figure 5.2a. Mathematically, the minimum void space in a system of perfectly packed spheres is 25.952%, while values of 30% and above would be more accurate for standard packings of nonideal particles. Analytes
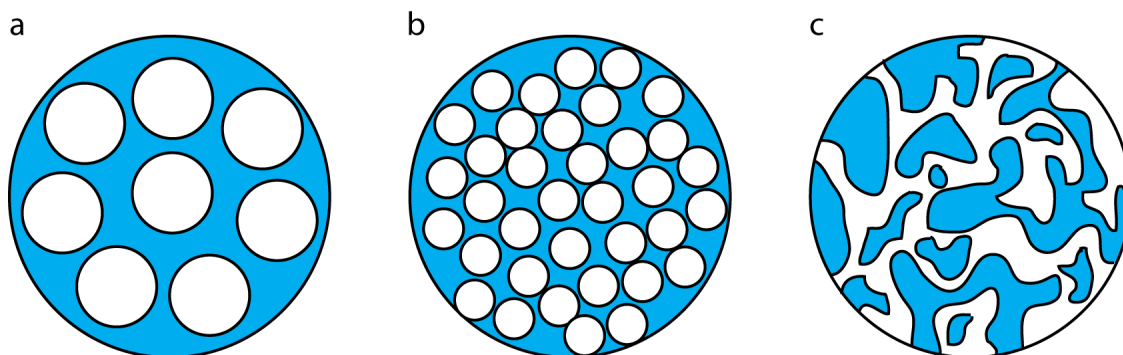
Figure 5.2: Comparison of cross sections between (a) particulate column with large particles, high permeability, and low efficiency, (b) particulate column with small particles, low permeability, and high efficiency, and (c) monolithic column with high permeability and high efficiency.

need to interact with the particulate stationary phase in order for separation to occur, which means that these void spaces (and thus a substantial fraction of the column volume) do not contribute to the separation of the analytes [138]. Additionally, diffusion between the interstitial voids and the porous structure of the stationary particles is often slow compared to flow through the void space itself [142], resulting in stagnant volumes of liquid within the intraparticle pore space, and broadened bands in chromatographic separations [56].

Furthermore, when studying larger molecules such as proteins and polymers, the limited diffusion rates may often necessitate the use of smaller particle size within the packed column (Figure 5.2b). This, in turn, causes a significant rise in backpressure through the column due to the diminishing interstitial volume and relatively low degree of interconnectivity throughout the porous structure [129]. While the problem can be mitigated by turning to chromatographic pumps capable of operating at extremely high pressure with small particle sizes, a more elegant alternative can be found with monolithic chromatography columns.

5.1.4 Monolithic Chromatography

Rather than forming a porous structure through the close packing of a large number of particles, monoliths rely on a highly interconnected permanent network of pores within a single structure (Figure 5.2c). The resulting porous media have an exceptionally high level of connectivity, and can possess very high levels of porosity, up to 80% [138]. Unlike packed particulate columns, the idea of "interstitial void space" is no longer relevant. Rather, fluid flowing through these structures is constantly in contact with the porous material, providing very high available surface area and allowing for very efficient mass transfer between the mobile and stationary phases. Furthermore, the high level of connectivity in monolithic structures allows one to achieve efficient separations at relatively low backpressures. Comparison between particulate and monolithic columns in one study demonstrated that a silica-based monolith with permeability (and, correspondingly, backpressure) similar to an 11 μm particulate column had an efficiency equal to that of a column using 3.5 μm beads [17]. Thus, monoliths provide an attractive alternative to particulate columns, and a way to
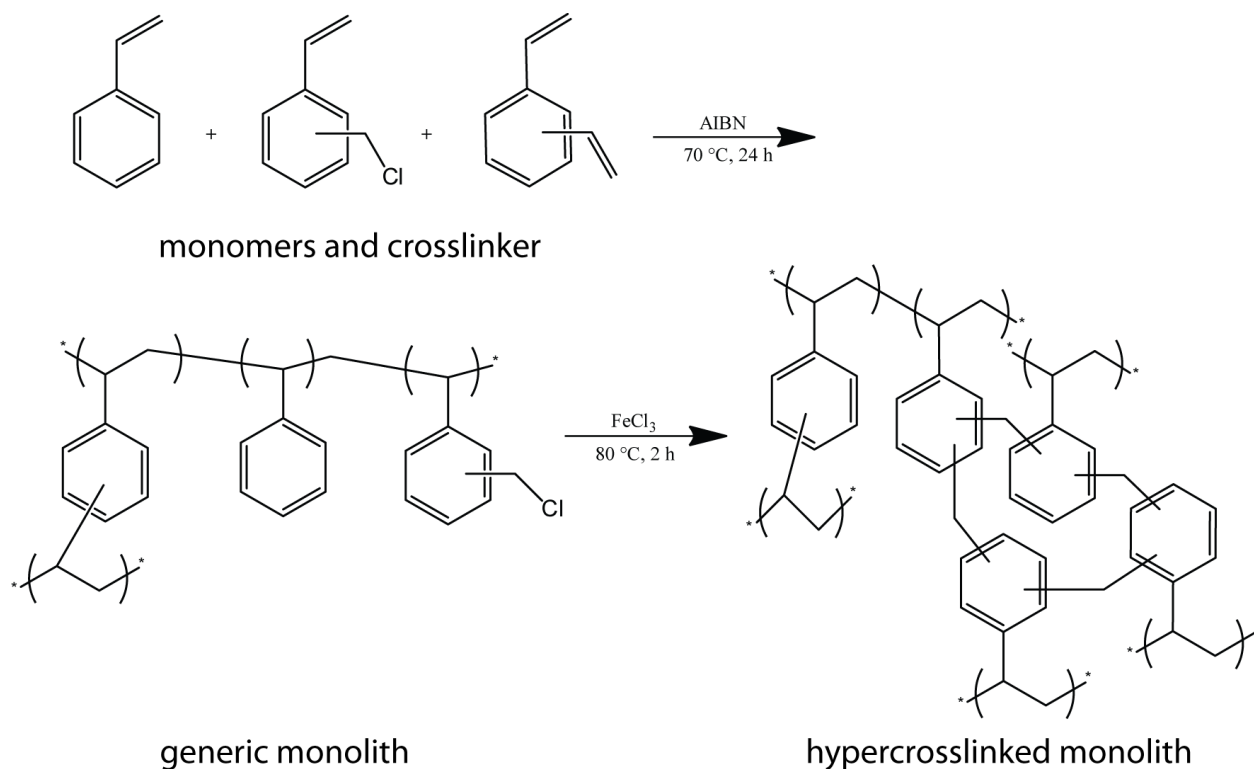
Figure 5.3: Polymerization and modification reactions to form hypercrosslinked organic polymer monoliths. Adapted, with permission, from [36].

achieve very high exposure to a porous network without requiring extremely small particles and correspondingly large backpressures.

While this work focuses on the chromatographic applications of porous monoliths, the uses for these fascinating materials are numerous and widespread. Examples of novel applications for porous monoliths include the usage of these materials as microfluidic mixers [116][90] and valves [88], supports for protein immobilization and digestion [75], bioreactors [34], electroosmotic pumps [148], and as media for pre-concentration and solid-phase extraction [136] as well as hydrogen storage [36][35]. The development and application of these materials is an area of extremely rapid growth, and, while progress has been made, a large part of their characteristics and functionality remains unknown or poorly understood.

Porous monoliths can be divided into two distinct classes, based on composition. The first of these are silica-based [18], which contain both macropores (on the order of 2 μm) and mesopores (on the order of 10 nm) [17]. Due to the presence of nanometer-scale mesopores, these columns are particularly valuable in the separation of small molecules, although they are less adept at separating large molecules [138] and can involve complicated methods of preparation [111]. The second class of porous monoliths is based upon the usage of organic polymers [137][128]. Typically, organic polymer monoliths have a much smaller proportion of nanometer-scale mesopores than their silica-based analogues, resulting in significantly better separation of large molecules (particularly biomacromolecules and polymers), but inferior performance when dealing with small molecules [111]. These limitations could provide one reason why, despite their ease of preparation, cost effectiveness, high connectivity, and ready
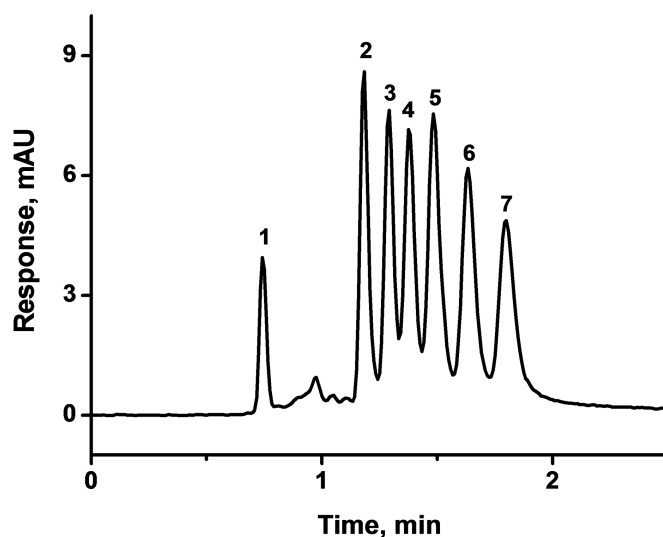
Figure 5.4: Efficient separation of small molecules using a hypercrosslinked organic polymer monolith (monitored by UV absorption). Analytes: uracil (1), benzene (2), toluene (3), ethylbenzene (4), propylbenzene (5), butylbenzene (6), pentylbenzene (7). Reprinted with permission from [150].

availability, a detailed study of the internal flow dynamics within polymer monoliths remains unavailable.

Recent developments in the modification of organic polymer monoliths [149][150] have greatly enhanced their separation efficiency when dealing with small molecules, resolving many of their previously discussed limitations and extending their scope well within the domain of silica-based monoliths. The formation of organic polymer monoliths with significant mesoporous networks is carried out via two steps (Figure 5.3): an initial polymerization reaction to form the generic monolith and an *in situ* hypercrosslinking reaction.

First, a thermal or photo-initiated radical polymerization process is carried out, typically using vinylbenzene and several of its derivatives as the monomers and crosslinkers which make up the polymer. As with the majority of organic polymer monoliths, the resulting porous structure consists primarily of micrometer-sized macropores, and, due to the minimal surface area, exhibits limited effectiveness in the separation of small molecules. Following the initial polymerization, a hypercrosslinking modification promotes the formation of a highly interconnected structure with a significant proportion of nanometer-scale pores [35]. Further details of this procedure can be found in Section 5.2.2.

Hypercrosslinked organic monoliths exhibit large surface areas due to their mesoporous structure, and have demonstrated very high efficiency in the separation of small molecules (Figure 5.4) [149]. Furthermore, the separation efficiency can be easily varied by changing the monolith preparation conditions (to alter the pore size distribution) and the experimental parameters (such as mobile phase and temperature), allowing excellent control of the chromatographic separation [150]. Through the use of a microcoil detector, we are able to perform a range of experiments, both directly and remotely detected, allowing us tremendous analytical insight into the properties and behavior of these promising new materials.

5.2 Materials & Methods

5.2.1 Chemicals and Materials

Styrene (99%), vinylbenzyl chloride (mixture of 3- and 4-isomers, 97%), divinylbenzene (80%, technical grade), 2,2-azobisisobutyronitrile (98%), acetonitrile (HPLC grade), water (HPLC grade), 1,2-dichloroethane, benzyl alcohol, uracil, benzene, and butylbenzene were all obtained from Sigma-Aldrich (St. Louis, MO, USA). The monomers (styrene, vinylbenzyl chloride, and divinylbenzene) were purified by passage through a bed of basic alumina to remove the inhibitors. Ferric chloride was purchased from Fisher Chemical (Fair Lawn, NJ, USA). Polyimide-coated 530 μm I.D. fused silica capillaries were purchased from Polymicro Technologies (Phoenix, AZ, USA). The commercial particle packed capillaries used for the ruggedness studies (Acclaim Phenyl-1, 50 mm $\times$ 250 μm I.D., with 3 μm particles and 120 $\mathring{A}$ average pore diameter) were obtained from Dionex (Sunnyvale, CA, USA).

5.2.2 Preparation of Monolithic Columns

The inner surface of the fused-silica capillary was first activated with 3-(trimethoxysilyl)-propyl methacrylate prior to formation of the monolith. The capillary was rinsed with acetone and water, then flushed with 0.2 mol/L sodium hydroxide for 30 min at a flow rate of 0.25 μL/min using a syringe pump (KdScientific, Holliston, MA, USA). The capillary was then rinsed with water. Next, 0.2 mol/L hydrochloric acid was pumped through the capillary for 30 min at a flow rate of 0.25 μL/min, followed by a rinsing with water and 95% ethanol. A 20% w/w solution of 3-(trimethoxysilyl)propyl methacrylate prepared in 95% ethanol with an apparent pH adjusted to 5 using acetic acid was pumped through the capillary at a flow rate of 0.25 μL/min for 90 min. The capillary was then washed with acetone, dried in a stream of nitrogen, and left at room temperature for 24 h.

The monolith preparation and hypercrosslinking reactions are outlined in Figure 5.3, and a detailed procedure can be found in [150]. In brief, generic monoliths were prepared in capillaries using in situ polymerization of mixtures of 21% styrene, 7% vinylbenzyl chloride, and 12% divinylbenzene dissolved in binary porogen solvent containing 19% toluene and 41% 1-dodecanol. 2,2-azobisisobutyronitrile (1%, w/w, with respect to monomers) was used as the initiator. The polymerization mixtures were purged with nitrogen for 10 min and then filled into the vinylized capillaries. Both ends of the capillary were sealed with rubber stoppers and the capillary was placed in a water bath. Polymerization was carried out at 70°C for 20 h. Both ends of the capillary were then cut to adjust its length and the monolithic column was washed with acetonitrile.

To perform the hypercrosslinking modification, the monolithic columns were flushed with 1,2-dichloroethane at a flow rate of 0.25 μL/min for 2 h. A filtered solution of 1 g of FeCl$_3$ in 20 mL of 1,2-dichloroethane was pumped through the columns at a flow rate of 0.25 μL/min for 2 h. The hypercrosslinking reaction was then allowed to proceed at 90°C for 2 h. The modified columns were washed with water overnight and tested.

5.2.3 Experimental Apparatus

LC experiments were performed using an Agilent 1100 system (Agilent, Santa Clara, CA, USA), equipped with a pump, auto-sampler and injector. The monolithic capillary column was connected to the injector via an empty 250 cm × 50 μm I.D. connection capillary. The monolith was attached in series with the NMR system described below. Typically, separations were performed isocratically in the reversed-phase mode, using a mixture of 90% acetonitrile (ACN) and 10% water as the mobile phase.

NMR experiments were performed on a 7 Tesla Oxford Instruments (Oxford Instruments, Oxfordshire, UK) superconducting magnet mated to a Varian console (Varian, Palo Alto, CA, USA). The system is equipped with an SGRAD 88/55/HD/S combined shelf-shielded gradient for micro-imaging and 18 channel room-temperature shim set. For RD-MRI experiments, the monolithic column was centered in a 40 mm Varian volume imaging probe, which served as the encoding coil. The outlet of the column was then connected to the remote microcoil detector by a 5 cm × 150 μm I.D. PEEK capillary (Idex Health & Science, Oak Harbor, WA, USA). The microcoil detector was a 360 μm I.D. 12 turn solenoid encased in a cell filled with FC-43 Fluorinert (3M, Maplewood, MN, USA) for susceptibility matching. The same microcoil was used for both encoding and detection during the small molecule separation experiments.

5.2.4 Remotely Detected Flow Imaging & Velocimetry

The mobile phase for these experiments consisted of 100% ACN pumped at a volumetric flow rate of 50 μL/min. The remote detection pulse sequence is shown in Figure 5.5 and further details of the remote detection experiment can be found in Chapter 3. Initial excitation consisted of a 5 kHz slice-selective sinc pulse. Following excitation into the transverse plane, velocity-compensated phase encoding gradients are applied such that the imaging plane is
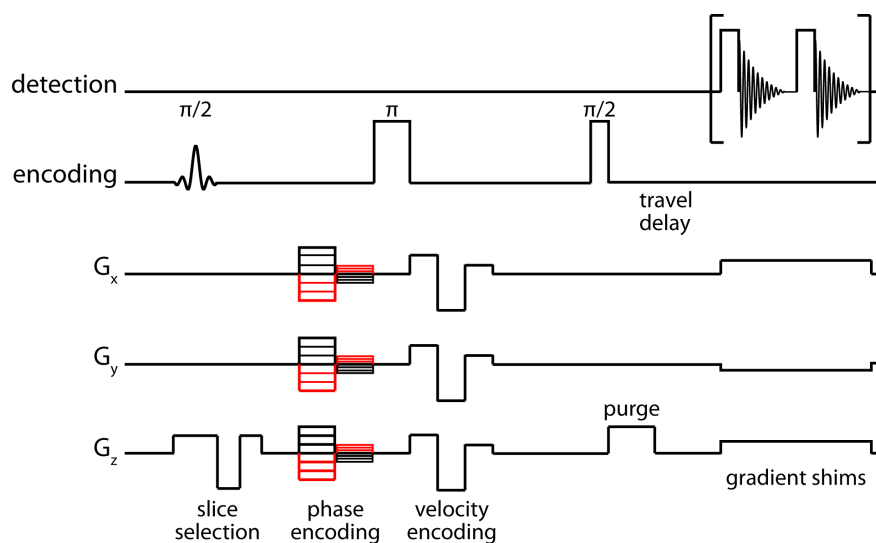

Figure 5.5: Pulse sequence for multidimensional remotely detected imaging experiments, with optional velocity encoding, as described previously in Section 3.2.

orthogonal to the direction of flow. The encoded information was then refocused with a π-pulse and stored along $\hat{z}$ with a $\pi/2$ pulse. The flowing mobile phase then carried the encoded information to the microcoil detector at a flow rate fast enough to avoid decay of the stored magnetization. For the flow rates and monolith sizes (530 μm I.D.) used, it often took up to 5 s for the encoded volume to flow through the detection coil. A series of $\pi/2$ pulses were applied stroboscopically during this interval, breaking the encoded fluid into discrete packets and providing a correlated time-of-flight dimension which reflects transit time to the detector. The duration of each acquired free induction decay (FID) was correlated to the coil residence time, which was $\sim$ 80 ms. A total of 50 time-of-flight acquisitions were collected during the course of remote acquisition.

The entire encoding and detection sequence was repeated for each phase encoded point of the image. The images discussed here had a dimensionality of 19×19 (361 k-space points), a field of view of $\sim$ 760 μm, and a resolution of $\sim$ 40 μm. A three-lobe position- and acceleration-compensated velocity-encoding gradient was added after the refocusing pulse in order to perform high resolution velocimetry experiments, as discussed in Section 3.2.3. Thus, velocity-encoded experiments contained an additional dimension (due to the necessity of obtaining data with opposing velocity gradients), doubling the total number of acquired points.

Velocity calibrations were used to identify the volumetric flow rate at which fluid flowing through an empty capillary had comparable linear velocity to the fluid flowing within the monolith. To do this, the velocity gradient was first incremented across a wide range of strengths. FIDs were collected at each gradient value (as well as across the 50-point time-of-flight dimension). Fourier transformation of these FIDs yielded spectra at each velocity encoding value (and time-of-flight point). Following this, the phase for each spectrum was determined, giving a plot for each time-of-flight point (showing acquired phase versus gradient strength). The slope of the linear region is indicative of the linear flow rate in the column. These plots were averaged across the linear region and over all of the time-of-flight points to give a characteristic phase at the chosen flow rate. This procedure was carried out for the monolith, after which the capillary flow rate was incremented until the averaged linear phase was approximately equal. A match in linear velocities was found between a 50 μL/min volumetric flow rate in the monolith and a 135 μL/min flow rate in the capillary.

5.2.5 Alignment Considerations

The disparity between column diameter and length in microcapillaries is typically at least 2-3 orders of magnitude, resulting in hugely different fields-of-view between axial and transverse dimensions. Therefore, images are often extremely sensitive to small errors in alignment, and a tilt of only a few degrees can appear quite dramatic in the final data (particularly so if it is using a distorted FOV to allow for easier visualization). Most importantly, if one is interested in obtaining a 2D axial slice through the column, alignment errors may cause the images to appear as ovals, and the velocity components obtained will be in a different frame of reference than is present in the column. While 3-dimensional velocity data could be processed to find the projection in the direction of flow, it is far simpler to ensure that the frames of reference of the gradients and the column are aligned.

Rather than try to align the column physically through a lengthy process of trial and error,

one can modify the pulse sequence to produce linear combinations of gradients according to angles which define the new, rotated frame. Because the capillary is cylindrically symmetric about its length, we can describe a coordinate system aligned along it using two angles, θ and ϕ, rather than the three Euler angles traditionally used to describe the orientation of a rigid body (if this reorientation were to be used for a non-cylindrical object, three angles would be necessary).

An example of a misaligned capillary and the relevant angles for the coordinate system transformation are shown in Figure 5.6. The first angle, θ, describes an axis in the xy plane, defined as the angle from $\hat{x}$ in a positive direction (towards $\hat{y}$). The second angle, ϕ, gives a rotation of the z-axis in the vertical plane containing this new axis. Two examples are shown in Figure 5.7. In the first case, where $\theta = 0$, a rotation of ϕ will tilt the coordinate system in the yz plane. In the second, where $\theta = \frac{\pi}{4}$, the rotation will tilt $\hat{z}$ straight backwards, maintaining an equal angle between $\hat{x}$ and $\hat{y}$. Negative values of θ will simply cause ϕ to tilt the system in the opposite sense.

In order to properly determine the new gradient values, the correct rotation matrix needs to be determined. In the case of the symmetric capillary, one simple way to do this is with the Rodrigues Rotation Formula, which gives the matrix for a rotation ϕ around a fixed axis specified by the vector $\hat{\omega} = (\omega_x, \omega_y, \omega_z)$. It is straightforward to define $\hat{\omega}$ in terms of θ: $\hat{\omega} = (\sin \theta, -\cos \theta, 0)$, resulting in the following matrix:

$$\mathbf{R}_{\hat{\omega}}(\theta) = \begin{bmatrix} \cos \phi + \sin^2 \theta (1 - \cos \phi) & -\cos \theta \sin \theta (1 - \cos \phi) & -\cos \theta \sin \phi \\ -\cos \theta \sin \theta (1 - \cos \phi) & \cos \phi + \cos^2 \theta (1 - \cos \phi) & -\sin \theta \sin \phi \\ \cos \theta \sin \phi & \sin \theta \sin \phi & \cos \phi \end{bmatrix} \tag{5.1}$$

To rotate the gradients, we simply multiply this matrix with the general gradient vector (G_x, G_y, G_z), giving the linear combinations for the gradient strengths in the new, rotated frame. Note that, since this matrix describes a rotation ϕ about the axis defined by θ, the
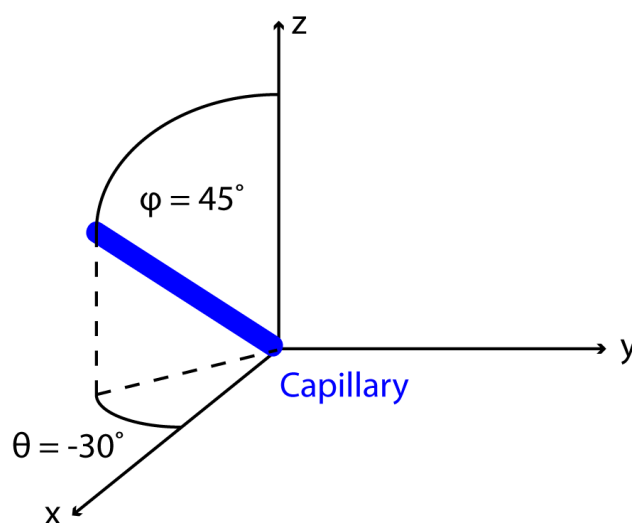

Figure 5.6: Example of a misaligned capillary and the relevant angles for the coordinate system transformation.
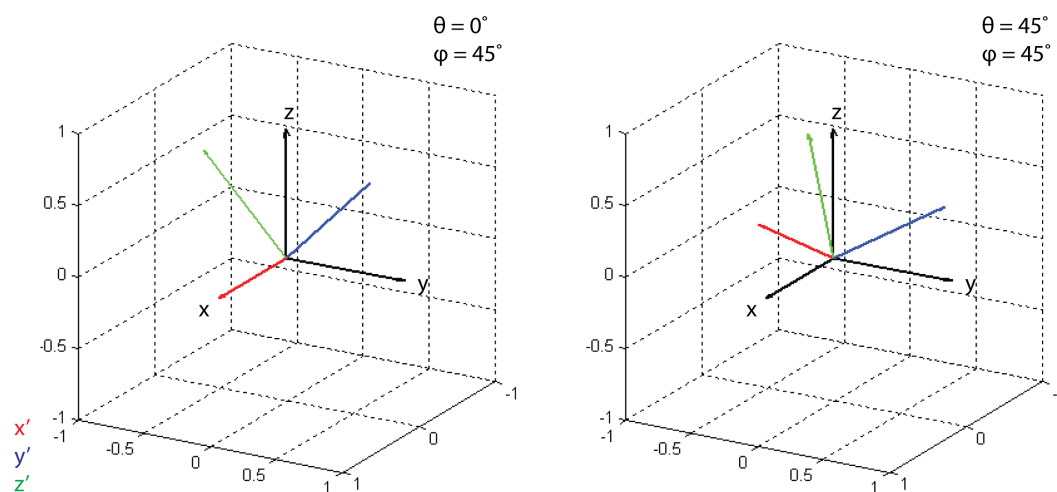
Figure 5.7: Examples of possible axis rotations and corresponding angles.

only way to accomplish a rotation of $\hat{x}$ and $\hat{y}$ while maintaining $\hat{z}$ along the longitudinal axis is to use $\phi = \pi$ (or change the rotation matrix itself).

The basic sign that the capillary is misaligned will be in the observation that the position of the slice along $\hat{x}$ or $\hat{y}$ is not constant across the TOF dimension. When the angles have been determined, the only motion of the signal should be along $\hat{z}$, the direction of flow. The procedure for determining the angles ϕ and θ is not as intuitive as one might hope, due to the difficulty of using planar images to determine the orientation of a 3D body. Still, there is a basic procedure which should yield acceptable results.

1. Take a series of 2D xz or yz images, either using a simpler version of the pulse sequence which only rotates $\hat{x}$ and $\hat{y}$ (i.e. $G'_x = G_x \cos\theta$ and $G'_y = G_y \sin\theta$), or set $\phi = \pi$ in the 3D sequence. Vary θ until the image is straight along $\hat{z}$. The fact that the projection of the capillary onto this plane is straight means that this plane now orthogonal to the plane formed by the angled capillary and $\hat{z}$ (in which the capillary would appear maximally bent). Alternatively, 1D z-images can also give a good indication of when the capillary is straight (the "peak" will become sharp) vs. angled (broad).

2. Set θ to the value which describes the plane containing the angled capillary and $\hat{z}$. In the case of the previous step, this would be orthogonal to the value of theta which gives the straightest capillary, meaning that one should add (or subtract, it doesn't matter) 90° from the previously determined value of theta. In situations where you're moving from a pulse sequence using a 2D angle rotation to one with 3D angle rotation, take care that theta is defined in a consistent way (this should be the case in the most recent versions of these sequences, in which theta is defined as a positive rotation from $\hat{x}$, towards $\hat{y}$).

3. Vary ϕ in small increments about 0, taking images in xz or yz (it doesn't always matter which, although you want to make sure you're not doing a plane that's orthogonal to the direction of the tilt, as you'd only see the projection of the tilted capillary, which
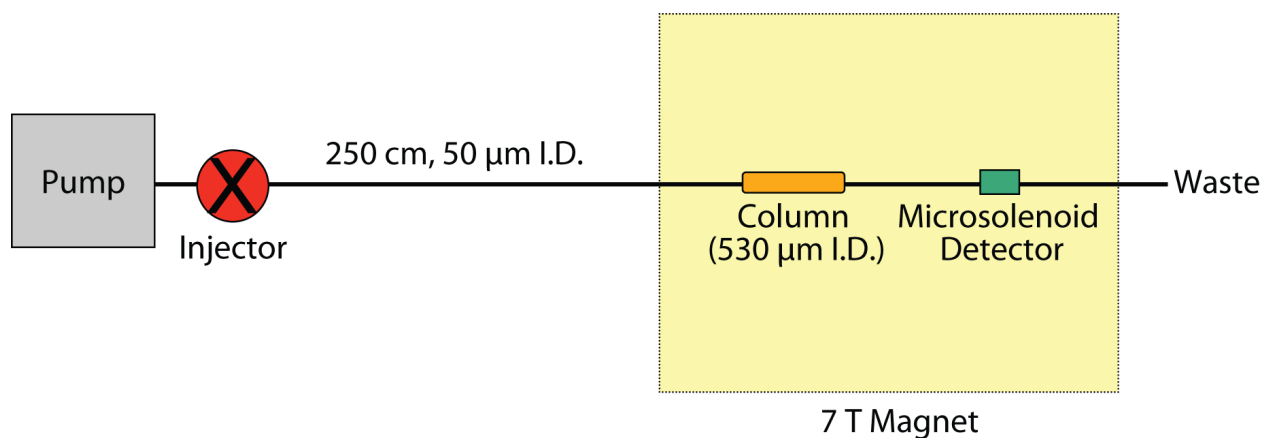
Figure 5.8: Schematic of the remote detection chromatography-NMR setup. The pump and injector are connected to the column inside the 7 Tesla magnet via a long capillary. Fluid flows through the column, which is enclosed in the encoding volume coil, and into the microsolenoid detector.

> wouldn't show much evidence of it straightening out). It is unlikely that ϕ will be very large.

4. Once the system is aligned, the capillary will straighten out in the 2D images, such that the only motion across the time-of-flight dimension is along $\hat{z}$.

5.2.6 Direct NMR Spectroscopy of Small Molecule Separations

The small molecule separation experiments integrated the built-in HPLC injector into the remote detection flow setup, as shown in Figure 5.8. The separations were carried out at a flow rate of 35 μL/min, using a mobile phase of 90% ACN and 10% H_2O. The 0.5 μL injection consisted of benzyl alcohol, benzene and butylbenzene at a ratio of $1:1:7$. Upon injection, the spectrometer was triggered (via a TTL pulse) to acquire spectra every 250 ms after a preliminary 35 s delay to account for travel through the 250 cm capillary from the injector to the column. Using the autosampler, this sequence was repeated 16 times to increase signal the signal to noise ratio. An extended sequence of 60 injections was also conducted to examine the injection reproducibility (discussed in Section 5.3.3).

5.3 Results & Discussion

5.3.1 Remotely Detected Flow Imaging & Velocimetry

Although magnetic resonance studies of mobile phase flow dynamics in particle-based columns have been performed [9][28][139][140], there are no comparable studies of fluid flow within monolithic columns (as well as no imaging experiments performed on columns of similar dimensions). While both of these column formats enable chromatographic separations, they possess fundamentally different pore structures and may not produce the same flow profile.
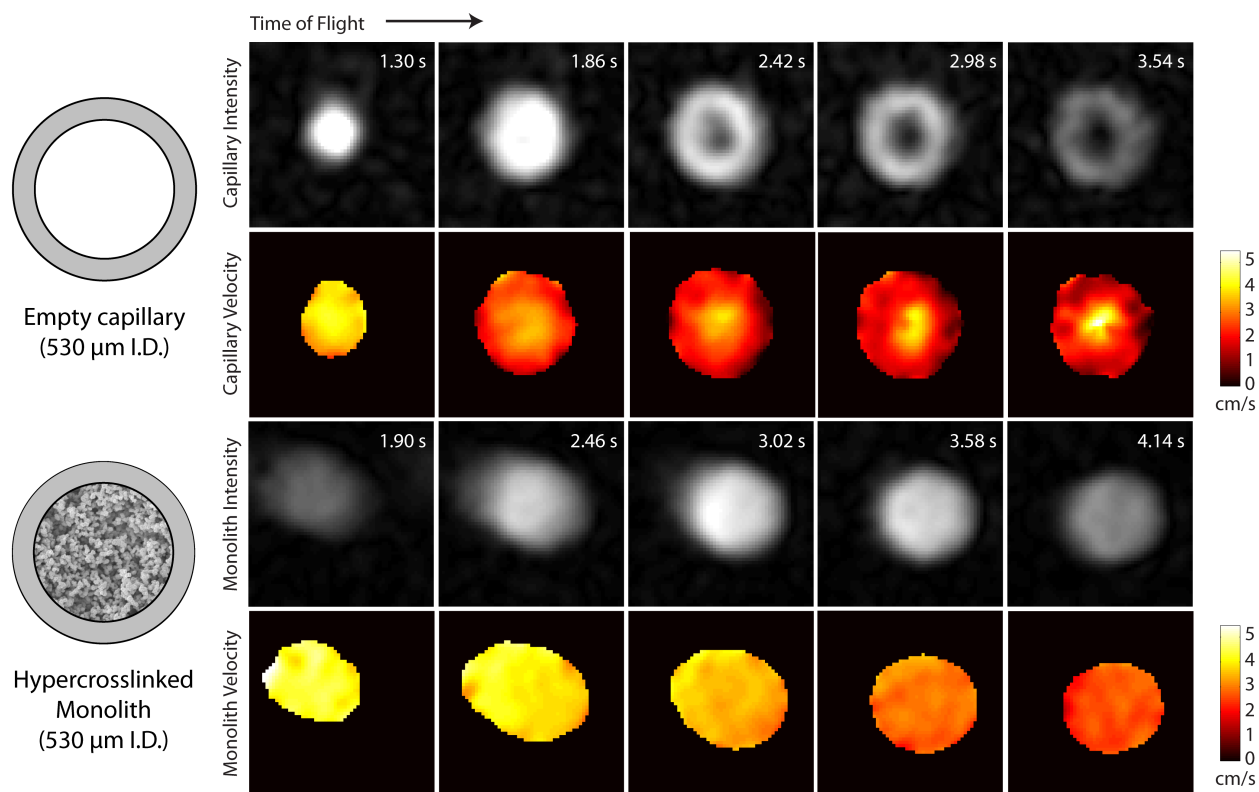
Figure 5.9: Axial images illustrating intensity and velocity for acetonitrile flowing through the capillary (top) and monolith (bottom). Five characteristic time-of-flight points were selected and the corresponding images are ordered by their travel time. These experiments were performed in an empty capillary and a hypercrosslined organic polymer monolith, both 90 mm × 530 μm I.D.. The mobile phase, consisting of 100% ACN, flowed at 50 μL/min in the monolith and 135μL/min in the capillary.

Ideally, a particle packed column with a similar diameter to our monoliths (530 μm) would be available for comparison (in addition to an empty capillary). Unfortunately, the selection of nonmagnetic particle-based columns is somewhat limited. While we were able to find a 250 μm I.D. column (see Sections 5.2.6 and 5.3.3) and a comparable monolith (the monoliths are easily prepared at any dimension), the decrease in diameter resulted in poor signal during remote acquisition and an inability to draw meaningful conclusions from the cross-sectional flow images. In spite of this, our ability to examine the monolithic flow behavior remains largely unaffected (the dynamics within particle beds are well-studied and would only provide an additional control).

A series of 2-dimensional remotely detected images in an empty capillary and an organic polymer monolith (both 530 μm I.D.) are shown in Figure 5.9. These experiments show both intensity and velocimetry data within axial slices through the two systems, and serve to illustrate a number of differences in flow behavior. Images are shown at five separate time-of-flight points, labeled by the time from storage pulse to arrival in the microcoil. The progression of images gives a view of the flow profile and dispersion within each system, and therefore insight into the overall flow behavior.
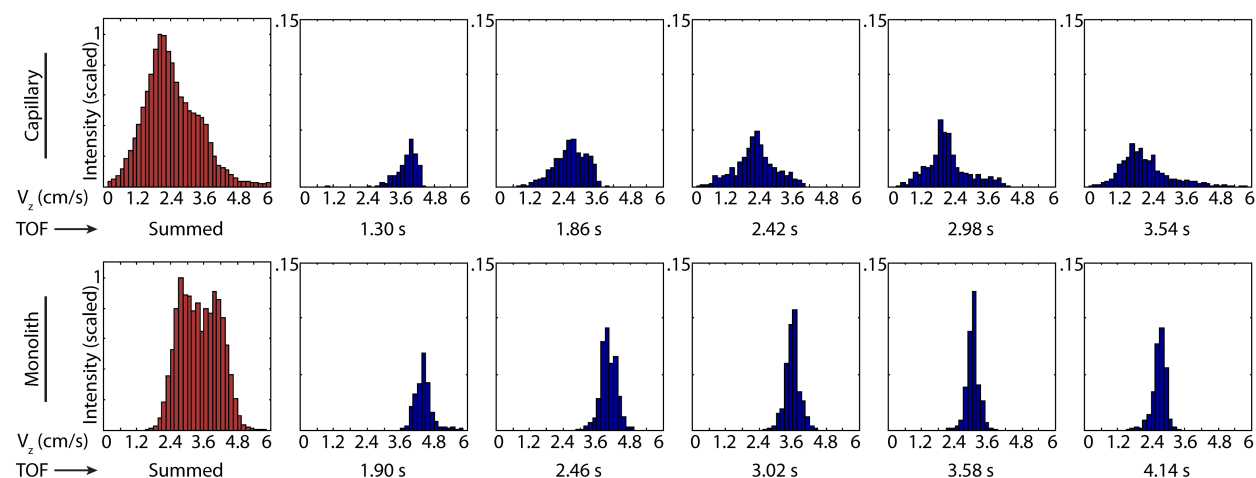
Figure 5.10: Histograms of the velocity data for both capillary and organic polymer monolith. Unlike the bead pack histograms, no weighting has been applied (due to the size of the pores, each voxel should contain approximately the same amount of liquid). Summed and individual time-of-flight histograms are shown, corresponding to the same data and conditions found in Figure 5.9.

The hypercrosslinked monoliths have a reduced interstitial volume (compared to the open capillary). As a result, the linear flow velocity within the monolithic column is higher than for the empty capillary at the same volumetric flow rate. To provide an equivalent comparison, the volumetric flow rate of the open capillary was increased in order to match the linear velocity to the flow inside of the monolith (as described in Section 5.2.4). As would be expected, the first encoded packet of fluid takes longer to arrive in the monolith experiment (1.30 s for the capillary and 1.90 s for the monolith) since the flow is slower in the capillary connecting the column to the detection region. The time for the entire encoded region to travel through the microcoil detector was typically $3 - 5$ s.

Because flow of the mobile phase is non-turbulent, the early time-of-flight points can be attributed to fluid which was closest to the detector at the time of encoding (and which therefore arrived at the detector first). This is quantified in the velocity images, which show that fluid in earlier time-of-flight points exhibits higher linear velocities in both the monolith and capillary. The average linear velocities decrease along the time-of-flight dimension from ~ 4 cm/s in early time-of-flight points down to ~ 2 cm/s at later points.

The most significant differences between the two experiments can be seen in the flow profile. As expected, a parabolic profile is observed in the open capillary, with fluid in the center of the capillary appearing earlier and with higher velocity than fluid near the boundaries. This behavior is characteristic of laminar flow and a no-slip boundary condition. The observed profile is substantially different in the monolith, which has a nearly plug-like distribution across the entire radial dimension of the column. These differences indicate that the unique monolithic pore structure serves to disrupt flow and evenly distribute the mobile phase across the column. Despite a general lack of evidence, it has been widely believed that the tortuous morphology in monoliths can negatively impact the radial distribution of

the mobile phase across the column. These data run contrary to this view, showing that the monolith instead acts as a continuous natural frit, distributing the mobile phase evenly.

Histograms of the velocity along the direction of flow (Figure 5.10) can add further quantitative insight into the flow behavior. The histograms are shown for the same time-of-flight points as in Figure 5.9, as well as for the sum of all time-of-flight points. The individual time-of-flight histograms are scaled with respect to their respective summed histogram, which has its largest bin set to a value of 1.

The summed histogram for the empty capillary data shows a clear peak and a significant number of pixels with velocities far from the mean. The additional shoulder seen in this distribution is representative of the large quantity of rapidly moving fluid at the center of the capillary, which retains a noticeably higher velocity than the fluid at the edges (as can be seen in Figure 5.9). The range of velocities observed for the empty capillary is significantly wider than with the monolithic column, which exhibits a relatively flat distribution of velocities that rapidly drops off on both sides of the histogram. This is consistent with uniform flow across the monolithic column and is unlike the open capillary flow, where wall interactions lead to significant drag and a wider velocity distribution. The open capillary also shows a maximum velocity that is approximately twice as large as the average, a feature which is characteristic of laminar flow. The individual time-of-flight points show far narrower distributions (and thus, more uniform velocities) in the monolith, further reinforcing these conclusions.

Another difference between the two sets of histograms can be seen in the mean velocity, which shifts position much more rapidly in the capillary than in the monolith. For the open capillary, this can be explained by considering the dramatic difference in velocities between fluid at the center of the capillary and at the edge. Due to the no-slip boundary condition of laminar flow, liquid at the boundaries of the capillary walls moves much more slowly than at the center. The arrival of this slow-moving fluid will be skewed toward later time-of-flight points, where it will have a significantly lower velocity than fluid which is delayed simply by virtue of a more distant initial position. The net effect of this will be a decrease in the mean velocity for these later time-of-flight points. In the plug-like flow of the monolith, dispersion is much less significant, and the attrition of slow-moving components into later time-of-flight points will be minimal. These results are consistent with a relatively uniform flow distribution within the monolith, promoted by homogeneous interactions with the high surface area of the nanoporous material. The characteristics which lead to plug-like flow within hypercrosslinked polymer monoliths (namely, the enhanced surface area and connectivity) are also the features which allow these materials to accommodate fast, efficient separations of small molecules at relatively high concentrations.

5.3.2 Direct NMR Spectroscopy of Small Molecule Separations

Having successfully demonstrated the application of RD-MRI to monolithic columns, we investigated whether or not we could achieve meaningful separations under the unusual flow conditions required for the imaging experiments. As mentioned previously, a rapid flow rate is required to transport the material from the encoding region to the detection coil before the encoded information is lost to relaxation. These conditions run contrary to what is typically required to produce efficient chromatographic separations, making the successful
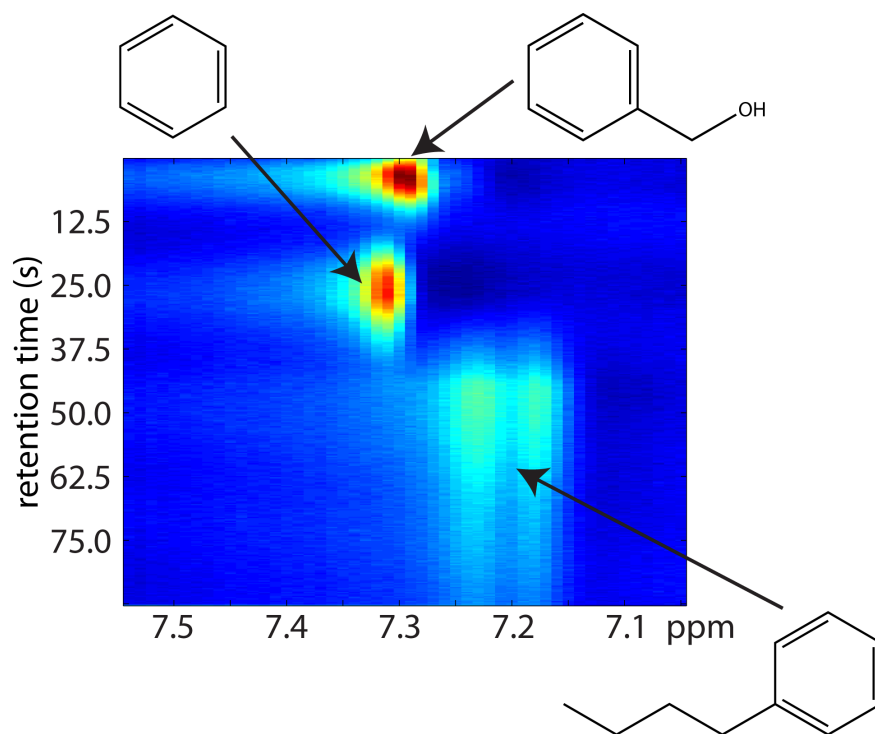
Figure 5.11: Two dimensional plot illustrating the separation of benzyl alcohol, benzene, and butylbenzene on a monolithic chromatography column. The horizontal axis corresponds to the NMR chemical shift while the vertical axis represents the retention time of compounds undergoing chromatographic separation (determined by the time until detection in the micro-coil). These experiments were performed in a 90 mm $\times$ 530 μm I.D. hypercrosslinked organic polymer monolith. The mobile phase, consisting of 80% ACN and 20% water, flowed at 40 μL/min at a pressure of $\sim$ 245 bar. The sample injection was a 0.5 μL volume of benzyl alcohol, benzene, and butylbenzene $(1 : 1 : 7)$.

demonstration of high flow-rate small molecule separations a noteworthy accomplishment.

Part of the challenge in monitoring a chromatographic separation with NMR comes from the experimental setup. Most notably, metallic components of the HPLC must be placed at a distance from the superconducting magnet, as they can cause inhomogeneities in the magnetic field and lead to potential physical hazards. As a result, an extended length of empty capillary is required between the HPLC and column, which adds undesirable dispersion to the bolus. Additionally, our home-built solenoid detector is not fully optimized for sensitivity and requires signal averaging and relatively large injections to achieve adequate signal-to-noise. However, injecting a large volume or a concentrated sample can lead to overloading of the stationary phase.

In spite of these challenges, we are able to demonstrate a fully resolved separation of benzyl alcohol, benzene, and butyl benzene using a 0.5 μL injection at a comparatively high flow rate. A 2-dimensional plot showing the aromatic region of the detected NMR spectrum versus the time until detection (indicative of the column retention time) is shown in Figure 5.11. While signal is observable from these compounds after a single acquisition, the data shown here are averaged over 16 repeated experiments. By using NMR detection,
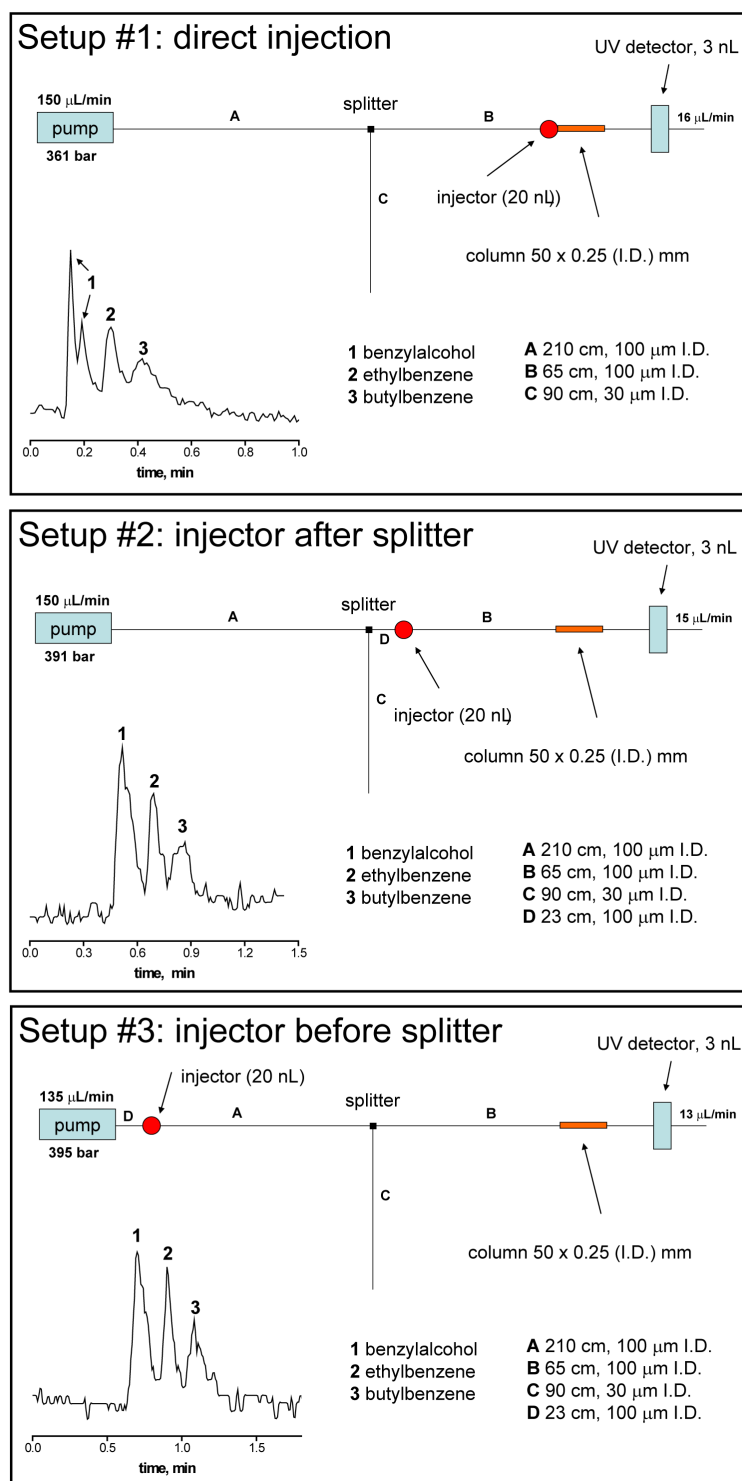
Figure 5.12: Effects of injector placement on separation efficacy within a hypercrosslinked organic polymer monolith. The configurations shown here make use of a split flow pathway to regulate the pressure (this is not done in the previously discussed experiments). All three configurations produce clear, well-resolved separations of the three aromatic compounds (benzyl alcohol, ethylbenzene, and butylbenzene), as monitored by UV-visible spectroscopy.

exact assignment of the eluting compounds can be made based on the chemical shifts of the protons. This is particularly advantageous in situations where multiple components fully or partially co-elute, causing overlap in the time-of-flight dimension which may still retain distinguishable peaks in the spectral axis. Combining NMR detection with chromatography allows users to observe the identity and quantity of each component as it elutes, and can be a powerful tool when optimizing conditions for fast, efficient separations. The detected spectra indicate a clear separation of the three compounds, where the doublet with the largest upfield shift is characteristic of the butylbenzene protons and the two earlier peaks belong to the benzene and benzyl alcohol protons (for these two, the time-of-flight is a better indication of identity).

5.3.3 Injector Placement & Repeatability

A variety of injector placements were tried in the course of determining the optimal flow setup for the separation experiments. Three configurations of the injection setup are shown in Figure 5.12, along with a UV absorption plot of the analytes (benzyl alcohol, ethylbenzene, and butylbenzene) as they emerge. All three cases show a well-resolved separation, even when the injector is placed at the pump, far away from the column. While the finalized apparatus does not make use of a splitter (for pressure control), these experiments still serve to confirm the robust separation performance of the hypercrosslinked monolith and to validate our placement of the injector away from the column.

In addition to their separation capabilities under nonideal flow conditions and alternate configurations, the monolithic columns showed excellent ruggedness under repeated injections and long-term use. To test this, a series of 60 sequential sample injections (~ 300 column volumes) were performed (using a 0.5 μL volume of 1 : 1 benzyl alcohol and butylbenzene), each of which triggered a pulse sequence to collect a series of spectra during outflow of the effluent. Integration was carried out across the aromatic protons, providing a measure of when the two compounds arrived in the microcoil detector. As shown in Figure 5.13, these data exhibit less than 2.1% relative standard deviation in the travel time from injector to detection coil.

These results are particularly notable in that the monoliths were subjected to flow rates of greater than 20 μL/min and pressures in excess of 240 bar for several weeks of continuous use. For comparison, two commercial columns (50 mm $\times$ 250 μm I.D.) packed with 3 μm silica particles were subjected to the same flow and pressure conditions as monoliths of comparable dimensions. After only three days of use, the particle packed columns showed visible voids at the head of columns while the monoliths showed no physical signs of degradation. While this instance cannot prove a general rule, it is well in line with the difficulties commonly reported by chromatographers when dealing with columns packed with very small particle sizes. Through their combination of ruggedness and low cost, flexible preparation in nonmagnetic microcapillary formats, polymer monoliths present themselves as an appealing alternative to particle packed columns, and an excellent choice for hyphenated NMR techniques.
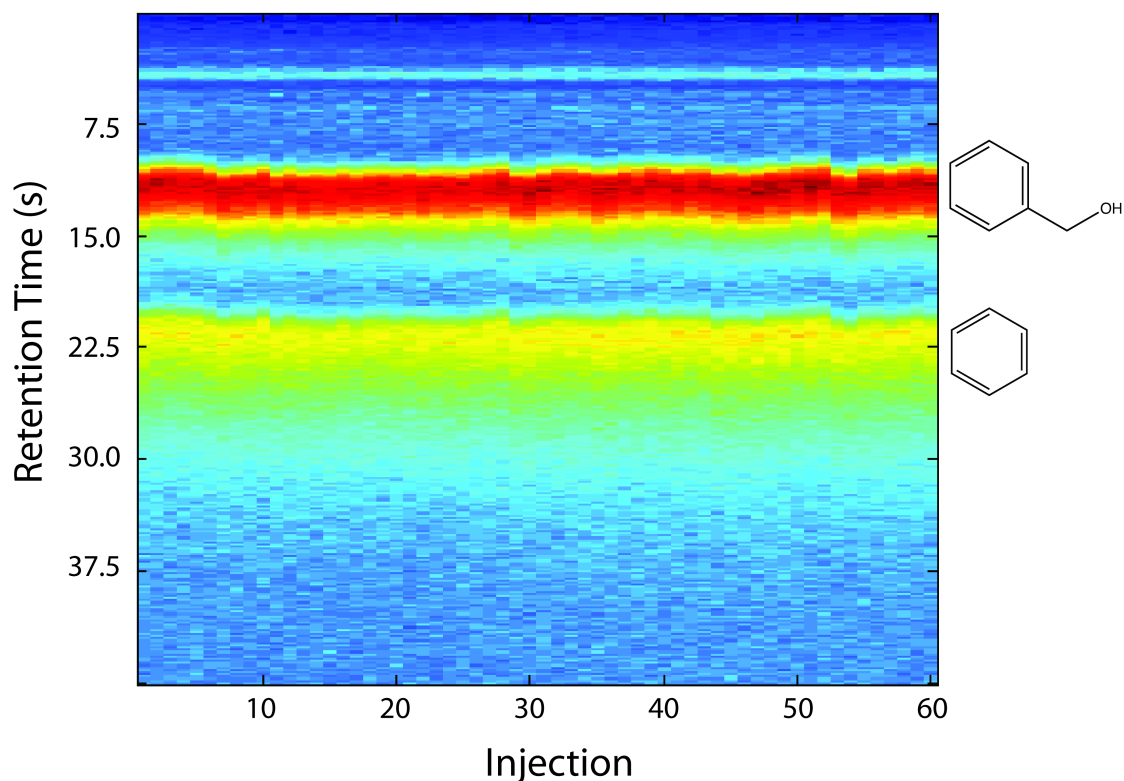
Figure 5.13: Reproducibility of triggered injections, with respect to arrival time of compounds in the detection coil. Integration was carried out across the aromatic peaks, and the resulting sum is plotted against the time of detection (indicative of retention time) for each injection. Analysis of the variation in the benzyl alcohol peak gives less than 2.1% RSD in the travel time from injector to detection coil.

5.4 Prospects for Remotely Detected Separations

One of the primary initial goals of this project was the application of remote detection to in-progress chromatographic separations. The general idea was to encode a mixture of analytes on the column, at which point their location or velocity would be stored and recovered later during detection. In this way, one could acquire a snapshot of a microchromatographic separation as it happened, a feat which could only be accomplished via remote detection. While there are a number of significant obstacles to overcome in this experiment, many of its features are within reach and under active investigation.

Several of these challenges have already been addressed. First, a remote detection experiment requires acquisition of numerous data points, which can be related to a sampling of k-space, velocity gradients, or the four-step phase cycle. When dealing with a chromatographic separation, this results in a requirement for highly repeatable, precisely timed injections, in which the in-progress separation must be nearly the same for each data point. This daunting requirement has proved to be quite manageable through the use of TTL triggering between the injection sequence on the HPLC and the pulse sequence on the spectrometer.

As discussed in Section 5.3.3, the deviation in separations from one experiment to the next is remarkably small. However, there is no escaping the added length to these experiments, as each injection and subsequent separation takes at least a minute (due in part to the long capillaries that are necessary to place the injector outside of the stray field). While these remote detection sequences are long, they are certainly feasible.

Other challenges lie in the choice between conditions that are optimal for chromatography and those that are optimal for remote detection. Quite often, these are diametrically opposed. The following list gives a summary of these factors, and the various trade-offs that should be considered when making adjustments.

1. Flow rate. Fast flow rates are necessary to bring the encoded spins to the detection region before T_1 decay, but usually worsen the quality of the separation. The most relevant limitation on flow rate is often the pressure on the monolith, which can rapidly surpass the tolerance levels of the experimental hardware (namely the pump and microfluidic connections).

2. Injection volume. Small injection volumes prevent overloading of the column and ensure better separation resolution, but they also diminish the signal to noise in the detection coil. This can be alleviated by repeating the experiment using triggered injection, but this signal averaging adds to the experimental time.

3. Column diameter. Separation efficiency and detectable signal can both be enhanced by increasing the column diameter, but the resulting travel times through the column are dramatically lengthened, causing loss of signal from T_1.

4. Column length. Likewise, long columns also enhance separations but increase the time until detection.

5. Transport capillary. Long transport times can be mitigated by reducing the diameter of the capillary between column and microcoil, but this often results in unacceptable signal loss due to decreased coil filling factor.

The numerous factors listed above may now reinforce the significance of our three compound separations discussed earlier. Even though we must find a balance between flow rate, column diameter, column length, capillary diameter, and injection volume, we are still able to carry out a highly effective, well-resolved chromatographic separation.

Because of the robust nature of hypercrosslinked organic polymer monoliths, remote monitoring of in-progress separations is an ongoing area of interest. The main trick to these experiments, besides the necessity of highly reproducible triggered injections, is to apply the encoding pulses to the analytes at the right time and at the right location. For a non-selective excitation, this presents little challenge. By incrementing the delay between the injection and application of the encoding pulses, one can take a series of travel curves that will begin to show spectra containing analyte peaks when the proper delay has been found. The compounds will often take a fair amount of time to travel through the column, so there is often a generous window for encoding. If slice selective experiments are desired (to zoom into a specific region of separation), the timing gets trickier (due to the narrowed encoding region), but the general idea is the same. Fortunately, estimates of the timing are quite

possible with knowledge of the time between injection and detection, volumetric flow rate, and capillary diameter.

In practice, remotely detected separations would provide a great deal of insight into the dynamics of compounds on the column. Using slice-selective excitation, the mixtures could be caught at a variety of different points in their separation, and further insight could be gained into their relative velocities and rates of dispersion through the column. High-resolution imaging across the axial dimension of these columns is unrealistic due to their scale. However, 1-dimensional imaging along the direction of flow is well within any resolution limits, and would provide nearly all of the desired insight. Further experiments could use velocity encoding to determine the retention time of these compounds, and q-space experiments could probe their relative velocity distributions. All told, a great deal of insight may yet be gained from this unique combination of techniques.

Bibliography

[1] ABBISS, J. B., CHUBB, T. W., AND PIKE, E. R. Laser Doppler anemometry. *Optics & Laser Technology 6*, 6 (1974), 249–261.

[2] ABRAGAM, A. *The Principles of Nuclear Magnetism.* The International Series on Monographs on Physics. Oxford University Press, Oxford, 1986.

[3] ADRIAN, R. J. Particle-Imaging Techniques for Experimental Fluid-Mechanics. *Annual Review of Fluid Mechanics 23* (1991), 261–304.

[4] ATKINSON, D., HILL, D. L., STOYLE, P. N., SUMMERS, P. E., CLARE, S., BOWTELL, R., AND KEEVIL, S. F. Automatic compensation of motion artifacts in MRI. *Magnetic Resonance in Medicine 41*, 1 (1999), 163–170.

[5] AUDOLY, B., SEN, P. N., RYU, S., AND SONG, Y. Q. Correlation functions for inhomogeneous magnetic field in random media with application to a dense random pack of spheres. *Journal of Magnetic Resonance 164*, 1 (2003), 154–159.

[6] BAJAJ, V. S., PAULSEN, J., HAREL, E., AND PINES, A. Zooming In on Microscopic Flow by Remotely Detected MRI. *Science 330*, 6007 (2010), 1078–1081.

[7] BANAVAR, J. R., AND SCHWARTZ, L. M. Magnetic-Resonance as a Probe of Permeability in Porous-Media. *Physical Review Letters 58*, 14 (1987), 1411–1414.

[8] BARRIE, P. J. Characterization of porous media using NMR methods. *Annual Reports on NMR Spectroscopy 41* (2000), 265–316.

[9] BAYER, E., MULLER, W., ILG, M., AND ALBERT, K. Visualization of Chromatographic Separations by NMR Imaging. *Angewandte Chemie International Edition in English 28* (1989), 1029–1032.

[10] BENNETT, C. M., WOLFORD, G. L., AND MILLER, M. B. The principled control of false positives in neuroimaging. *Social Cognitive and Affective Neuroscience 4*, 4 (2009), 417–422.

[11] BERNSTEIN, M., KING, K., AND ZHOU, X. *Handbook of MRI pulse sequences.* Elsevier Academic Press, 2004.

[12] BLOCH, F., AND SIEGERT, A. Magnetic Resonance for Nonrotating Fields. *Phys. Rev. 57*, 6 (Mar 1940), 522–527.

[13] BODURKA, J., AND BANDETTINI, P. A. Toward direct mapping of neuronal activity: MRI detection of ultraweak, transient magnetic fields changes. *Magnetic Resonance in Medicine 47*, 6 (2002), 1052–1058.

[14] BODURKA, J., JESMANOWICZ, A., HYDE, J. S., XU, H., ESTKOWSKI, L., AND LI, S. J. Current-induced magnetic resonance phase imaging. *Journal of Magnetic Resonance 137*, 1 (1999), 265–271.

[15] BORTHAKUR, A., CHARAGUNDLA, S. R., WHEATON, A., AND REDDY, R. $T_{1\rho}$-weighted MRI using a surface coil to transmit spin-lock pulses. *Journal of Magnetic Resonance 167*, 2 (2004), 306–316.

[16] BURACAS, G. T., LIU, T. T., BUXTON, R. B., FRANK, L. R., AND WONG, E. C. Imaging periodic currents using alternating balanced steady-state free precession. *Magnetic Resonance in Medicine 59*, 1 (2008), 140–148.

[17] CABRERA, K. Applications of silica-based monolithic HPLC columns. *Journal of Separation Science 27*, 10-11 (2004), 843–852.

[18] CABRERA, K., LUBDA, D., EGGENWEILER, H.-M., MINAKUCHI, H., AND NAKANISHI, K. A New Monolithic-Type HPLC Column For Fast Separations. *Journal of High Resolution Chromatography 23*, 1 (2000), 1521–4168.

[19] CALLAGHAN, P. T. *Principles of nuclear magnetic resonance microscopy*. Clarendon Press, Oxford, 1991.

[20] CANOLTY, R. T., EDWARDS, E., DALAL, S. S., SOLTANI, M., NAGARAJAN, S. S., KIRSCH, H. E., BERGER, M. S., BARBARO, N. M., AND KNIGHT, R. T. High gamma power is phase-locked to theta oscillations in human neocortex. *Science 313*, 5793 (2006), 1626–1628.

[21] CASSARA, A. M., HAGBERG, G. E., BIANCIARDI, M., MIGLIORE, M., AND MARAVIGLIA, B. Realistic simulations of neuronal activity: A contribution to the debate on direct detection of neuronal currents by MRI. *Neuroimage 39*, 1 (2008), 87–106.

[22] CASSARA, A. M., AND MARAVIGLIA, B. Microscopic investigation of the resonant mechanism for the implementation of nc-MRI at ultra-low field MRI. *Neuroimage 41*, 4 (2008), 1228–1241.

[23] CASSARA, A. M., MARAVIGLIA, B., HARTWIG, S., TRAHMS, L., AND BURGHOFF, M. Neuronal current detection with low-field magnetic resonance: simulations and methods. *Magnetic Resonance Imaging 27*, 8 (2009), 1131–1139.

[24] CHARAGUNDLA, S. R., BORTHAKUR, A., LEIGH, J. S., AND REDDY, R. Artifacts in $T_{1\rho}$-weighted imaging: correction with a self-compensating spin-locking pulse. *Journal of Magnetic Resonance 162*, 1 (2003), 113–121.

[25] CHOW, L. S., DAGENS, A., FU, Y., COOK, G. G., AND PALEY, M. N. J. Comparison of BOLD and Direct-MR Neuronal Detection (DND) in the Human Visual Cortex at 3T. *Magnetic Resonance in Medicine 60*, 5 (2008), 1147–1154.

[26] CHU, R. N., DE ZWART, J. A., VAN GELDEREN, P., FUKUNAGA, M., KELLMAN, P., HOLROYD, T., AND DUYN, J. H. Hunting for neuronal currents: absence of rapid MRI signal changes during visual-evoked response. *Neuroimage 23*, 3 (2004), 1059–1067.

[27] COHEN, L. B., SALZBERG, B. M., AND GRINVALD, A. Optical Methods for Monitoring Neuron Activity. *Annual Review of Neuroscience 1* (1978), 171–182.

[28] DICKSON, M. L., NORTON, T. T., AND FERNANDEZ, E. J. Chemical imaging of multicomponent viscous fingering in chromatography. *AIChE Journal 43* (1997), 409–418.

[29] DUNN, K. J. Enhanced transverse relaxation in porous media due to internal field gradients. *Journal of Magnetic Resonance 156*, 2 (2002), 171–180.

[30] DUVVURI, U., CHARAGUNDLA, S. R., KUDCHODKAR, S. B., KAUFMAN, J. H., KNEELAND, J. B., RIZI, R., LEIGH, J. S., AND REDDY, R. Human Knee: In Vivo $T_{1\rho}$-weighted MR Imaging at 1.5 T - Preliminary Experience. *Radiology 220*, 3 (2001), 822–826.

[31] EDWARDS, E., SOLTANI, M., DEOUELL, L. Y., BERGER, M. S., AND KNIGHT, R. T. High gamma activity in response to deviant auditory stimuli recorded directly from human cortex. *Journal of Neurophysiology 94*, 6 (2005), 4269–4280.

[32] FEINAUER, A., ALTOBELLI, S. A., AND FUKUSHIMA, E. NMR measurements of flow profiles in a coarse bed of packed spheres. *Magnetic Resonance Imaging 15*, 4 (1997), 479–487.

[33] FERNANDEZ-PELLO, A. C. Micropower generation using combustion: Issues and approaches. *Proceedings of the Combustion Institute 29* (2003), 883–899.

[34] GEISER, L., EELTINK, S., SVEC, F., AND FRECHET, J. M. J. In-line system containing porous polymer monoliths for protein digestion with immobilized pepsin, peptide preconcentration and nano-liquid chromatography separation coupled to electrospray ionization mass spectroscopy. *Journal of Chromatography A 1188*, 2 (2008), 88–96.

[35] GERMAIN, J., FRECHET, J., AND SVEC, F. Nanoporous Polymers for Hydrogen Storage. *Small 5*, 10 (2009), 1098–1111.

[36] GERMAIN, J., HRADIL, J., FRCHET, J. M. J., AND SVEC, F. High Surface Area Nanoporous Polymers for Reversible Hydrogen Storage. *Chemistry of Materials 18*, 18 (2006), 4430–4435.

[37] GOLDMAN, R. I., STERN, J. M., ENGEL, J., AND COHEN, M. S. Acquiring simultaneous EEG and functional MRI. *Clinical Neurophysiology 111*, 11 (2000), 1974–1980.

[38] Goldman, R. I., Wei, C.-Y., Philiastides, M. G., Gerson, A. D., Friedman, D., Brown, T. R., and Sajda, P. Single-trial discrimination for integrating simultaneous EEG and fMRI: Identifying cortical areas contributing to trial-to-trial variability in the auditory oddball task. *NeuroImage 47*, 1 (2009), 136 – 147.

[39] Goodson, B. M. Nuclear Magnetic Resonance of Laser-Polarized Noble Gases in Molecules, Materials, and Organisms. *Journal of Magnetic Resonance 155*, 2 (2002), 157 – 216.

[40] Granwehr, J., Harel, E., Han, S., Garcia, S., Pines, A., Sen, P. N., and Song, Y. Q. Time-of-flight flow imaging using NMR remote detection. *Physical Review Letters 95*, 7 (2005), 075503.

[41] Granwehr, J., and Seeley, J. A. Sensitivity quantification of remote detection NMR and MRI. *Journal of Magnetic Resonance 179*, 2 (2006), 280–289.

[42] Grynbaum, M. D., Kreidler, D., Rehbein, J., Purea, A., Schuler, P., Schaal, W., Czesla, H., Webb, A., Schurig, V., and Albert, K. Hyphenation of gas chromatography to microcoil 1H nuclear magnetic resonance spectroscopy. *Analytical Chemistry 79*, 7 (2007), 2708–13.

[43] Hagberg, G. E., Bianciardi, M., and Maraviglia, B. Challenges for detection of neuronal currents by MRI. *Magnetic Resonance Imaging 24*, 4 (2006), 483–493.

[44] Hahn, E. L. Spin Echoes. *Phys. Rev. 80*, 4 (Nov 1950), 580–594.

[45] Hall, L. D., and Rajanayagam, V. Visualization of Chromatography Columns by NMR Imaging. *Journal of the American Chemical Society*, 8 (1985), 499–501.

[46] Halpern-Manners, N. W., Bajaj, V. S., Teisseyre, T. Z., and Pines, A. Magnetic resonance imaging of oscillating electrical currents. *Proceedings of the National Academy of Sciences of the United States of America 107*, 19 (2010), 8519–8524.

[47] Halpern-Manners, N. W., Paulsen, J. L., Bajaj, V. S., and Pines, A. Remotely Detected MRI Velocimetry in Microporous Bead Packs. *The Journal of Physical Chemistry A 115*, 16 (2011), 4023–4030.

[48] Han, S. I., Granwehr, J., Garcia, S., McDonnell, E. E., and Pines, A. Auxiliary probe design adaptable to existing probes for remote detection NMR, MRI, and time-of-flight tracing, journal = Journal of Magnetic Resonance. 260–272.

[49] Harel, E. *Multidimensional Remote Detection of Magnetic Resonance*. PhD thesis, University of California, Berkeley, 2008.

[50] Harel, E., Granwehr, J., Seeley, J. A., and Pines, A. Multiphase imaging of gas flow in a nanoporous material using remote-detection NMR. *Nature Materials 5*, 4 (2006), 321–327.

[51] HAREL, E., HILTY, C., KOEN, K., MCDONNELL, E. E., AND PINES, A. Time-of-Flight Flow Imaging of Two-Component Flow inside a Microfluidic Chip. *Phys. Rev. Lett. 98*, 1 (Jan 2007), 017601.

[52] HAREL, E., AND PINES, A. Spectrally resolved flow imaging of fluids inside a microfluidic chip with ultrahigh time resolution. *Journal of Magnetic Resonance 193*, 2 (2008), 199–206.

[53] HERRMANN, C. S., MUNK, M. H. J., AND ENGEL, A. K. Cognitive functions of gamma-band activity: memory match and utilization. *Trends in Cognitive Sciences 8*, 8 (2004), 347–355.

[54] HILTY, C., MCDONNELL, E. E., GRANWEHR, J., PIERCE, K. L., HAN, S. I., AND PINES, A. Microfluidic gas-flow profiling using remote-detection NMR. *Proceedings of the National Academy of Sciences of the United States of America 102*, 42 (2005), 14960–14963.

[55] HMLINEN, M., HARI, R., ILMONIEMI, R. J., KNUUTILA, J., AND LOUNASMAA, O. V. Magnetoencephalography - theory, instrumentation, and applications to noninvasive studies of the working human brain. *Reviews of Modern Physics 65*, 2 (1993), 413.

[56] HORVATH, C., AND LIN, H.-J. Band spreading in liquid chromatography: General plate height equation and a method for the evaluation of the individual plate height contributions. *Journal of Chromatography A 149* (1978), 43 – 70.

[57] HOULT, D. I., AND RICHARDS, R. E. The signal-to-noise ratio of the nuclear magnetic resonance experiment. *Journal of Magnetic Resonance 24*, 1 (1976), 71 – 85.

[58] HOWARD, J. J. Quantitative estimates of porous media wettability from proton NMR measurements. *Magnetic Resonance Imaging 16*, 5-6 (1998), 529–533.

[59] HRLIMANN, M. D. Effective Gradients in Porous Media Due to Susceptibility Differences. *Journal of Magnetic Resonance 131*, 2 (1998), 232–240.

[60] HRLIMANN, M. D., LATOUR, L. L., AND SOTAK, C. H. Diffusion Measurement in Sandstone Core - Nmr Determination of Surface-to-Volume Ratio and Surface Relaxivity. *Magnetic Resonance Imaging 12*, 2 (1994), 325–327.

[61] HUNTER, M. W., AND CALLAGHAN, P. T. NMR Measurement of Nonlocal Dispersion in Complex Flows. *Physical Review Letters 99*, 21 (2007), 210602.

[62] JENSEN, O., KAISER, J., AND LACHAUX, J. P. Human gamma-frequency oscillations associated with attention and memory. *Trends in Neurosciences 30*, 7 (2007), 317–324.

[63] JOHNS, M. L., SEDERMAN, A. J., BRAMLEY, A. S., GLADDEN, L. F., AND ALEXANDER, P. Local transitions in flow phenomena through packed beds identified by MRI. *AIChE Journal 46*, 11 (2000), 2151–2161.

[64] Joy, M., Scott, G., and Henkelman, M. Invivo Detection of Applied Electric Currents by Magnetic-Resonance Imaging. *Magnetic Resonance Imaging 7*, 1 (1989), 89–94.

[65] Joy, M. L. G., Lebedev, V. P., and Gati, J. S. Imaging of current density and current pathways in rabbit brain during transcranial electrostimulation. *IEEE Transactions on Biomedical Engineering 46*, 9 (1999), 1139–1149.

[66] Kamei, H., Iramina, K., Yoshikawa, K., and Ueno, S. Neuronal current distribution imaging using magnetic resonance. *IEEE Transactions on Magnetics 35*, 5 (1999), 4109–4111.

[67] Ketcham, R. A., and Carlson, W. D. Acquisition, optimization and interpretation of X-ray computed tomographic imagery: applications to the geosciences. *Computers & Geosciences 27*, 4 (2001), 381–400.

[68] Khrapitchev, A. A., and Callaghan, P. T. Reversible and irreversible dispersion in a porous medium. *Physics of Fluids 15*, 9 (2003), 2649–2660.

[69] Klimesch, W. EEG alpha and theta oscillations reflect cognitive and memory performance: a review and analysis. *Brain Research Reviews 29*, 2-3 (1999), 169–195.

[70] Konn, D., Gowland, P., and Bowtell, R. MRI detection of weak magnetic fields due to an extended current dipole in a conducting sphere: A model for direct detection of neuronal currents in the brain. *Magnetic Resonance in Medicine 50*, 1 (2003), 40–49.

[71] Konn, D., Leach, S., Gowland, P., and Bowtell, R. Initial attempts at directly detecting alpha wave activity in the brain using MRI. *Magnetic Resonance Imaging 22*, 10 (2004), 1413–1427.

[72] Korringa, J., Seevers, D. O., and Torrey, H. C. Theory of Spin Pumping and Relaxation in Systems with a Low Concentration of Electron Spin Resonance Centers. *Physical Review 127*, 4 (1962), 1143–1150.

[73] Kraus, R. H., Espy, M. A., Volegov, P. L., Matlachov, A. N., Mosher, J. C., Urbaitis, A. V., and Zotev, V. S. Toward SQUID-based direct measurement of neural currents by nuclear magnetic resonance. *IEEE Transactions on Applied Superconductivity 17*, 2 (2007), 854–857.

[74] Kraus, R. H., Volegov, P., Matlachov, A., and Espy, M. Toward direct neural current imaging by resonant mechanisms at ultra-low field. *Neuroimage 39*, 1 (2008), 310–317.

[75] Krenkova, J., and Svec, F. Less common applications of monoliths: IV. Recent developments in immobilized enzyme reactors for proteomics and biotechnology. *Journal of Separation Science 32*, 5-6 (2009), 706–718.

[76] Kutsovsky, Y. E., Scriven, L. E., Davis, H. T., and Hammer, B. E. NMR imaging of velocity profiles and velocity distributions in bead packs. *Physics of Fluids 8*, 4 (1996), 863–871.

[77] Lacey, M. E., Subramanian, R., Olson, D. L., Webb, A. G., and Sweedler, J. V. High-Resolution NMR Spectroscopy of Sample Volumes from 1 nL to 10 μL. *Chemical Reviews 99*, 10 (1999), 3133–3152. PMID: 11749512.

[78] Lacey, M. E., Tan, Z. J., Webb, A. G., and Sweedler, J. V. Union of capillary high-performance liquid chromatography and microcoil nuclear magnetic resonance spectroscopy applied to the separation and identification of terpenoids. *Journal of Chromatography A 922*, 1-2 (2001), 139–49.

[79] Lanzer, P., Botvinick, E. H., Schiller, N. B., Crooks, L. E., Arakawa, M., Kaufman, L., Davis, P. L., Herfkens, R., Lipton, M. J., and Higgins, C. B. Cardiac Imaging Using Gated Magnetic-Resonance. *Radiology 150*, 1 (1984), 121–127.

[80] Lazar, I. M., Trisiripisal, P., and Sarvaiya, H. A. Microfluidic liquid chromatography system for proteomic applications and biomarker screening. *Analytical Chemistry 78*, 15 (2006), 5513–5524.

[81] Lee, K. H., Williams, L. M., Breakspear, M., and Gordon, E. Synchronous Gamma activity: a review and contribution to an integrative neuroscience model of schizophrenia. *Brain Research Reviews 41*, 1 (2003), 57–78.

[82] Levitt, M. *Spin Dynamics: Basics of Nuclear Magnetic Resonance.* John Wiley & Sons, 2008.

[83] Li, T. Q., Kastrup, A., Takahashi, A. M., and Moseley, M. E. Functional MRI of human brain during breath holding by BOLD and FAIR techniques. *NeuroImage 9*, 2 (1999), 243–249.

[84] Liaw, H. K., Kulkarni, R., Chen, S. H., and Watson, A. T. Characterization of fluid distributions in porous media by NMR techniques. *AIChE Journal 42*, 2 (1996), 538–546.

[85] Limtiaco, J. F. K., Jones, C. J., and Larive, C. K. Characterization of Heparin Impurities with HPLC-NMR Using Weak Anion Exchange Chromatography. *Analytical Chemistry 81*, 24 (2009), 10116–10123.

[86] Logothetis, N. K. What we can do and what we cannot do with fMRI. *Nature 453*, 7197 (2008), 869–878.

[87] Luo, Q. F., Lu, H., Lu, H. B., Senseman, D., Worsley, K., Yang, Y. H., and Gao, J. H. Physiologically evoked neuronal current MRI in a bloodless turtle brain: Detectable or not? *Neuroimage 47*, 4 (2009), 1268–1276.

[88] Luo, Q. Z., Mutlu, S., Gianchandani, Y. B., Svec, F., and Frechet, J. M. J. Monolithic valves for microfluidic chips based on thermoresponsive polymer gels. *Electrophoresis 24*, 21 (2003), 3694–3702.

[89] Lustig, M., Donoho, D., and Pauly, J. M. Sparse MRI: The application of compressed sensing for rapid MR imaging. *Magnetic Resonance in Medicine 58*, 6 (2007), 1182–1195.

[90] Mair, D. A., Schwei, T. R., Dinio, T. S., Svec, F., and Frechet, J. M. J. Use of photopatterned porous polymer monoliths as passive micromixers to enhance mixing efficiency for on-chip labeling reactions. *Lab on a Chip 9*, 7 (2009), 877–883.

[91] Mair, R. W., Wong, G. P., Hoffmann, D., Hurlimann, M. D., Patz, S., Schwartz, L. M., and Walsworth, R. L. Probing Porous Media with Gas Diffusion NMR. *Physical Review Letters 83*, 16 (1999), 3324.

[92] Majumdar, S., and Gore, J. C. Studies of Diffusion in Random-Fields Produced by Variations in Susceptibility. *Journal of Magnetic Resonance 78*, 1 (1988), 41–55.

[93] Maly, T., Debelouchina, G. T., Bajaj, V. S., Hu, K.-N., Joo, C.-G., Mak-Jurkauskas, M. L., Sirigiri, J. R., van der Wel, P. C. A., Herzfeld, J., Temkin, R. J., and Griffin, R. G. Dynamic nuclear polarization at high magnetic fields. *Journal of Chemical Physics 128*, 5 (2008).

[94] Massin, C., Vincent, F., Homsy, A., Ehrmann, K., Boero, G., Besse, P.-A., Daridon, A., Verpoorte, E., de Rooij, N. F., and Popovic, R. S. Planar microcoil-based microfluidic NMR probes. *Journal of Magnetic Resonance 164*, 2 (2003), 242 – 255.

[95] McDonnell, E. E., Han, S. L., Hilty, C., Pierce, K. L., and Pines, A. NMR analysis on microfluidic devices by remote detection. *Analytical Chemistry 77*, 24 (2005), 8109–8114.

[96] Menon, R. S., and Kim, S. G. Spatial and temporal limits in cognitive neuroimaging with fMRI. *Trends in Cognitive Sciences 3*, 6 (1999), 207–216.

[97] Mikac, U., Demsar, F., Beravs, K., and Sersa, I. Magnetic resonance imaging of alternating electric currents. *Magnetic Resonance Imaging 19*, 6 (2001), 845–856.

[98] Moule, A. J., Spence, M. M., Han, S. I., Seeley, J. A., Pierce, K. L., Saxena, S., and Pines, A. Amplification of xenon NMR and MRI by remote detection. *Proceedings of the National Academy of Sciences of the United States of America 100*, 16 (2003), 9122–9127.

[99] Natterer, J., and Bargon, J. Parahydrogen induced polarization. *Progress in Nuclear Magnetic Resonance Spectroscopy 31*, 4 (1997), 293 – 315.

[100] OGAWA, S., LEE, T. M., NAYAK, A. S., AND GLYNN, P. Oxygenation-Sensitive Contrast in Magnetic-Resonance Image of Rodent Brain at High Magnetic-Fields. *Magnetic Resonance in Medicine 14*, 1 (1990), 68–78.

[101] OLSON, D. L., PECK, T. L., WEBB, A. G., MAGIN, R. L., AND SWEEDLER, J. V. High-Resolution Microcoil 1H-NMR for Mass-Limited, Nanoliter-Volume Samples. *Science 270*, 5244 (1995), 1967–1970.

[102] PALEY, M. N. J., CHOW, L. S., WHITBY, E. H., AND COOK, G. G. Modelling of axonal fields in the optic nerve for direct MR detection studies. *Image and Vision Computing 27*, 4 (2009), 331–341.

[103] PALVA, S., AND PALVA, J. M. New vistas for [alpha]-frequency band oscillations. *Trends in Neurosciences 30*, 4 (2007), 150 – 158.

[104] PANTEV, C., MAKEIG, S., HOKE, M., GALAMBOS, R., HAMPSON, S., AND GALLEN, C. Human Auditory Evoked Gamma-Band Magnetic-Fields. *Proceedings of the National Academy of Sciences of the United States of America 88*, 20 (1991), 8996–9000.

[105] PAPE, H., ARNOLD, J., PECHNIG, R., CLAUSER, C., TALNISHNIKH, E., ANFEROVA, S., AND BLUMICH, B. Permeability Prediction for Low Porosity Rocks by Mobile NMR. *Pure and Applied Geophysics 166*, 5-7 (2009), 1125–1163.

[106] PARK, T. S., AND LEE, S. Y. Effects of neuronal magnetic fields on MRI: Numerical analysis with axon and dendrite models. *Neuroimage 35*, 2 (2007), 531–538.

[107] PARK, T. S., LEE, S. Y., PARK, J. H., CHO, M. H., AND LEE, S. Y. Observation of the fast response of a magnetic resonance signal to neuronal activity: a snail ganglia study. *Physiological Measurement 27*, 2 (2006), 181–190.

[108] PARKES, L. M., DE LANGE, F. P., FRIES, P., TONI, I., AND NORRIS, D. G. Inability to directly detect magnetic field changes associated with neuronal activity. *Magnetic Resonance in Medicine 57*, 2 (2007), 411–416.

[109] PAULSEN, J. *The Design and Application of an Adjustable NMR Sensor and The MRI Imaging of Flow in Microfluidics with Remote Detection.* PhD thesis, University of California, Berkeley, 2009.

[110] PAULSEN, J., BAJAJ, V. S., AND PINES, A. Compressed sensing of remotely detected MRI velocimetry in microfluidics. *Journal of Magnetic Resonance 205*, 2 (2010), 196–201.

[111] PETERS, E. C., SVEC, F., AND FRECHET, J. M. J. Rigid Macroporous Polymer Monoliths. *Advanced Materials 11*, 14 (1999), 1524–4095.

[112] PETRIDOU, N., PLENZ, D., SILVA, A. C., LOEW, M., BODURKA, J., AND BANDETTINI, P. A. Direct magnetic resonance detection of neuronal electrical activity. *Proceedings of the National Academy of Sciences of the United States of America 103*, 43 (2006), 16015–16020.

[113] POPE, J. M., AND YAO, S. Quantitative NMR imaging of flow. *Concepts in Magnetic Resonance 5*, 4 (1993), 281–302.

[114] POPTANI, H., DUVVURI, U., MILLER, C. G., MANCUSO, A., CHARAGUNDLA, S., FRASER, N. W., GLICKSON, J. D., LEIGH, J. S., AND REDDY, R. $T_{1\rho}$ Imaging of Murine Brain Tumors at 4 T. *Academic Radiology 8*, 1 (2001), 42 – 47.

[115] PUTZBACH, K., KRUCKER, M., GRYNBAUM, M. D., HENTSCHEL, P., WEBB, A. G., AND ALBERT, K. Hyphenation of capillary high-performance liquid chromatography to microcoil magnetic resonance spectroscopy - determination of various carotenoids in a small-sized spinach sample. *Journal of Pharmaceutical and Biomedical Analysis 38*, 5 (2005), 910–7.

[116] ROHR, T., YU, C., DAVEY, M. H., SVEC, F., AND FRECHET, J. M. J. Porous polymer monoliths: Simple and efficient mixers prepared by direct polymerization in the channels of microfluidic chips. *Electrophoresis 22*, 18 (2001), 3959–3967.

[117] SCHWINDT, P. D. D., KNAPPE, S., SHAH, V., HOLLBERG, L., KITCHING, J., LIEW, L. A., AND MORELAND, J. Chip-scale atomic magnetometer. *Applied Physics Letters 85*, 26 (2004), 6409–6411.

[118] SCOTT, G. C., JOY, M. L. G., ARMSTRONG, R. L., AND HENKELMAN, R. M. Measurement of Nonuniform Current-Density by Magnetic-Resonance. *IEEE Transactions on Medical Imaging 10*, 3 (1991), 362–374.

[119] SCOTT, G. C., JOY, M. L. G., ARMSTRONG, R. L., AND HENKELMAN, R. M. Rf Current-Density Imaging in Homogeneous Media. *Magnetic Resonance in Medicine 28*, 2 (1992), 186–201.

[120] SCOTT, G. C., JOY, M. L. G., ARMSTRONG, R. L., AND HENKELMAN, R. M. Rotating-Frame Rf Current-Density Imaging. *Magnetic Resonance in Medicine 33*, 3 (1995), 355–369.

[121] SEDERMAN, A. J., JOHNS, M. L., ALEXANDER, P., AND GLADDEN, L. F. Structure-flow correlations in packed beds. *Chemical Engineering Science 53*, 12 (1998), 2117–2128.

[122] SEDERMAN, A. J., JOHNS, M. L., BRAMLEY, A. S., ALEXANDER, P., AND GLADDEN, L. F. Magnetic resonance imaging of liquid flow and pore structure within packed beds. *Chemical Engineering Science 52*, 14 (1997), 2239–2250.

[123] SEELEY, J. A., HAN, S. I., AND PINES, A. Remotely detected high-field MRI of porous samples. *Journal of Magnetic Resonance 167*, 2 (2004), 282–290.

[124] SEN, P. N., AND AXELROD, S. Inhomogeneity in local magnetic field due to susceptibility contrast. *Journal of Applied Physics 86*, 8 (1999), 4548–4554.

[125] SEPPONEN, R., POHJONEN, J., SIPPONEN, J., AND TANTTU, J. A method for $T_{1\rho}$ imaging. *J. Comput. Assist. Tomogr. 9*, 6 (1985), 1007–1011.

[126] SEYMOUR, J. D., AND CALLAGHAN, P. T. Generalized approach to NMR analysis of flow and dispersion in porous media. *AIChE Journal 43*, 8 (1997), 2096–2111.

[127] SIROTIN, Y. B., AND DAS, A. Anticipatory haemodynamic signals in sensory cortex not predicted by local neuronal activity. *Nature 457*, 7228 (2009), 475–479.

[128] SMITH, N. W., AND JIANG, Z. Developments in the use and fabrication of organic monolithic phases for use with high-performance liquid chromatography and capillary electrochromatography. *Journal of Chromatography A 1184*, 1-2 (2008), 416 – 440.

[129] SNYDER, L. R., KIRKLAND, J. J., AND DOLAN, J. W. *Introduction to Modern Liquid Chromatography*, 3rd ed. Wiley, New York, 2009.

[130] SONG, Y.-Q. Using internal magnetic fields to obtain pore size distributions of porous media. *Concepts in Magnetic Resonance Part A 18A*, 2 (2003), 97–110.

[131] SONG, Y. Q., CHO, H., HOPPER, T., POMERANTZ, A. E., AND SUN, P. Z. Magnetic resonance in porous media: Recent progress. *Journal of Chemical Physics 128*, 5 (2008), 052212.

[132] STANISZ, G. J., ODROBINA, E. E., PUN, J., ESCARAVAGE, M., GRAHAM, S. J., BRONSKILL, M. J., AND HENKELMAN, R. M. T_1, T_2 relaxation and magnetization transfer in tissue at 3T. *Magnetic Resonance in Medicine 54*, 3 (2005), 507–512.

[133] STEHLING, M. K., TURNER, R., AND MANSFIELD, P. Echo-Planar Imaging - Magnetic-Resonance-Imaging in a Fraction of a Second. *Science 254*, 5028 (1991), 43–50.

[134] SUBRAMANIAN, R., AND WEBB, A. G. Design of solenoidal microcoils for high-resolution 13c nmr spectroscopy. *Analytical Chemistry 70*, 13 (1998), 2454–2458.

[135] SUN, B., AND DUNN, K.-J. Probing the internal field gradients of porous media. *Physical Review E 65*, 5 (2002), 051309.

[136] SVEC, F. Less common applications of monoliths: Preconcentration and solid-phase extraction. *Journal of Chromatography B 841*, 1-2 (2006), 52 – 64.

[137] SVEC, F., AND FRECHET, J. M. J. Continuous rods of macroporous polymer as high-performance liquid chromatography separation media. *Analytical Chemistry 64* (1992), 820–822.

[138] SVEC, F., AND HUBER, C. G. Monolithic Materials: Promises, Challenges, Achievements. *Analytical Chemistry 78*, 7 (2006), 2100–2107.

[139] TALLAREK, U., BAUMEISTER, E., ALBERT, K., BAYER, E., AND GUIOCHON, G. NMR Imaging of the Chromatographic Process - Migration and Separation of Bands of Gadolinium Chelates. *Journal of Chromatography A 696*, 1 (1995), 1–18.

[140] Tallarek, U., Bayer, E., van Dusschoten, D., Scheenen, T., Van As, H., Guiochon, G., and Neue, U. D. Dynamic NMR microscopy of chromatographic columns. *AiChe Journal 44*, 9 (1998), 1962–1975.

[141] Tallarek, U., van Dusschoten, D., Van As, H., Bayer, E., and Guiochon, G. Study of transport phenomena in chromatographic columns by pulsed field gradient NMR. *Journal of Physical Chemistry B 102*, 18 (1998), 3486–3497.

[142] Tallarek, U., Vergeldt, F. J., and As, H. V. Stagnant Mobile Phase Mass Transfer in Chromatographic Media: Intraparticle Diffusion and Exchange Kinetics. *The Journal of Physical Chemistry B 103*, 36 (1999), 7654–7664.

[143] Tang, L., Avison, M. J., Gatenby, J. C., and Gore, J. C. Failure to direct detect magnetic field-dephasing corresponding to ERP generation. *Magnetic Resonance Imaging 26*, 4 (2008), 484–489.

[144] Taylor, J. M., Cappellaro, P., Childress, L., Jiang, L., Budker, D., Hemmer, P. R., Yacoby, A., Walsworth, R., and Lukin, M. D. High-sensitivity diamond magnetometer with nanoscale resolution. *Nature Physics 4*, 10 (2008), 810–816.

[145] Teisseyre, T., Paulsen, J., Bajaj, V., Halpern-Manners, N., and Pines, A. Compressed Sensing with Prior Information Accelerates Microfluidic Magnetic Resonance Imaging. *Journal of Magnetic Resonance (submitted)*.

[146] Telkki, V. V., Hilty, C., Garcia, S., Harel, E., and Pines, A. Quantifying the diffusion of a fluid through membranes by double phase encoded remote detection magnetic resonance imaging. *Journal of Physical Chemistry B 111*, 50 (2007), 13929–13936.

[147] Tran, B. Q., Lundanes, E., and Greibrokk, T. The influence of stop-flow on band broadening of peptides in micro-liquid chromatography. *Chromatographia 64*, 1-2 (2006), 1–5.

[148] Tripp, J. A., Svec, F., Frechet, J. M. J., Zeng, S., Mikkelsen, J. C., and Santiago, J. G. High-pressure electroosmotic pumps based on porous polymer monoliths. *Sensors and Actuators B: Chemical 99*, 1 (2004), 66 – 73.

[149] Urban, J., Svec, F., and Frechet, J. M. J. Efficient Separation of Small Molecules Using a Large Surface Area Hypercrosslinked Monolithic Polymer Capillary Column. *Analytical Chemistry 82*, 5 (2010), 1621–1623.

[150] Urban, J., Svec, F., and Frechet, J. M. J. Hypercrosslinking: New approach to porous polymer monolithic capillary columns with large surface area for the highly efficient separation of small molecules. *Journal of Chromatography A 1217*, 52 (2010), 8212–8221.

[151] Vissers, J. P. C. Recent developments in microcolumn liquid chromatography. *Journal of Chromatography A 856*, 1-2 (1999), 117–143.

[152] WASHBURN, K. E., AND CALLAGHAN, P. T. Tracking Pore to Pore Exchange Using Relaxation Exchange Spectroscopy. *Physical Review Letters 97*, 17 (2006), 175502.

[153] WATSON, A. T., AND CHANG, C. T. P. Characterizing porous media with NMR methods. *Progress in Nuclear Magnetic Resonance Spectroscopy 31* (1997), 343–386.

[154] WEBB, A. G. Nuclear magnetic resonance coupled microseparations. *Magnetic Resonance in Chemistry 43*, 9 (2005), 688–696.

[155] WEBB, A. G., AND SWEEDLER, J. V. Interfacing magnetic resonance detectors with chemical microseparations. *Abstracts of Papers of the American Chemical Society 224* (2002), U150–U150.

[156] WEISSKOFF, R. M., ZUO, C. S., BOXERMAN, J. L., AND ROSEN, B. R. Microscopic Susceptibility Variation and Transverse Relaxation - Theory and Experiment. *Magnetic Resonance in Medicine 31*, 6 (1994), 601–610.

[157] WINKLER, M., ZHOU, M., BERNARDO, M., ENDEWARD, B., AND THOMANN, H. Internal magnetic gradient fields in glass bead packs from numerical simulations and constant time diffusion spin echo measurements. *Magnetic Resonance Imaging 21*, 3-4 (2003), 311–315.

[158] WITSCHEY, W. R. T., BORTHAKUR, A., ELLIOTT, M. A., MELLON, E., NIYOGI, S., WALLMAN, D. J., WANG, C. Y., AND REDDY, R. Artifacts in $T_{1\rho}$-weighted imaging: Compensation for B-1 and B-0 field imperfections. *Journal of Magnetic Resonance 186*, 1 (2007), 75–85.

[159] WITZEL, T., LIN, F. H., ROSEN, B. R., AND WALD, L. L. Stimulus-induced Rotary Saturation (SIRS): A potential method for the detection of neuronal currents with MRI. *Neuroimage 42*, 4 (2008), 1357–1365.

[160] WOOLRICH, M. W., RIPLEY, B. D., BRADY, M., AND SMITH, S. M. Temporal Autocorrelation in Univariate Linear Modeling of fMRI Data. *NeuroImage 14*, 6 (2001), 1370 – 1386.

[161] XUE, Y. Q., CHEN, X. Y., GRABOWSKI, T., AND XIONG, J. H. Direct MRI Mapping of Neuronal Activity Evoked by Electrical Stimulation of the Median Nerve at the Right Wrist. *Magnetic Resonance in Medicine 61*, 5 (2009), 1073–1082.

[162] XUE, Y. Q., GAO, J. H., AND XIONG, J. H. Direct MRI detection of neuronal magnetic fields in the brain: Theoretical modeling. *Neuroimage 31*, 2 (2006), 550–559.

[163] YOON, R. S., CZAYA, A., KWAN, H. C., AND JOY, M. L. G. Changes in the complex permittivity during spreading depression in rat cortex. *IEEE Transactions on Biomedical Engineering 46*, 11 (1999), 1330–1338.

[164] YOON, R. S., DEMONTE, T. P., HASANOV, K. F., JORGENSON, D. B., AND JOY, M. L. G. Measurement of thoracic current flow in pigs for the study of defibrillation and cardioversion. *IEEE Transactions on Biomedical Engineering 50*, 10 (2003), 1167–1173.

[165] ZARAHN, E., AGUIRRE, G. K., AND D'ESPOSITO, M. Empirical Analyses of BOLD fMRI Statistics. *NeuroImage 5*, 3 (1997), 179 – 197.

[166] ZHANG, X., AND WEBB, A. G. Magnetic resonance microimaging and numerical simulations of velocity fields inside enlarged flow cells used for coupled NMR microseparations. *Analytical Chemistry 77* (2005), 1338–44.

[167] ZIELINSKI, L. J., AND SEN, P. N. Relaxation of nuclear magnetization in a nonuniform magnetic field gradient and in a restricted geometry. *Journal of Magnetic Resonance 147*, 1 (2000), 95–103.

Appendix A

Remote Detection Probe Schematics

A.1 Microcoil Detection Probe

While the microcoil detection probe described here was designed by past members of the Pines lab, a complete set of standardized, up-to-date schematics has not been previously collected. Therefore, in conjunction with the schematics for the modular surface coil encoding probe, I have created and included a set of schematics giving detailed specifications for each component of the microcoil detection probe. A discussion of the design concepts behind auxiliary remote detection probes may be found in ref [48], although the probe shown here makes use of a later generation design (see Chapter 3 and the thesis of E. Harel [49] for further details).
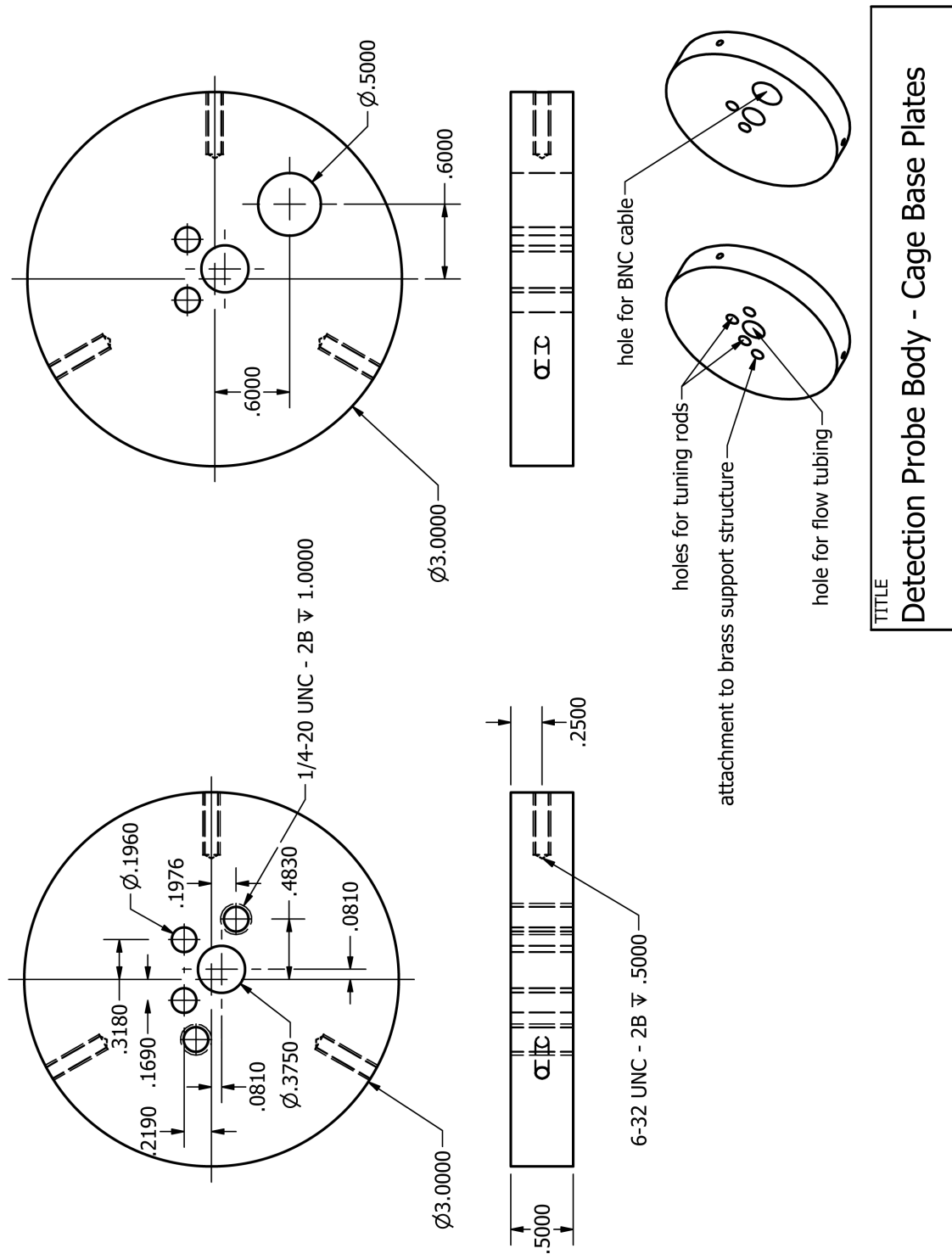
Figure A.1: Detection probe body - cage base plates

This is the uppermost portion of the probe, and is partly inserted into the top of the magnet bore. The aluminum ring attaches around the cage and can be adjusted to determine the depth of the probe within the magnet. This design is for an 89mm bore. The dimensions can be adjusted as needed for differing bore sizes.

TITLE
Detection Probe Body - End Cage

1/4-20 UNC - 2B

.2500
.5000

Ø.1875 ⩛ 1.2500
1/4-20 UNC - 2B

30°

Ø3.5000
Ø5.0000
Ø4.2500

6-32 UNC ⩛ THRU

70°
50°

R1.6250
R1.5000
.2500

.2500
14.0000
.5000

Figure A.2: Detection probe body - end cage

117
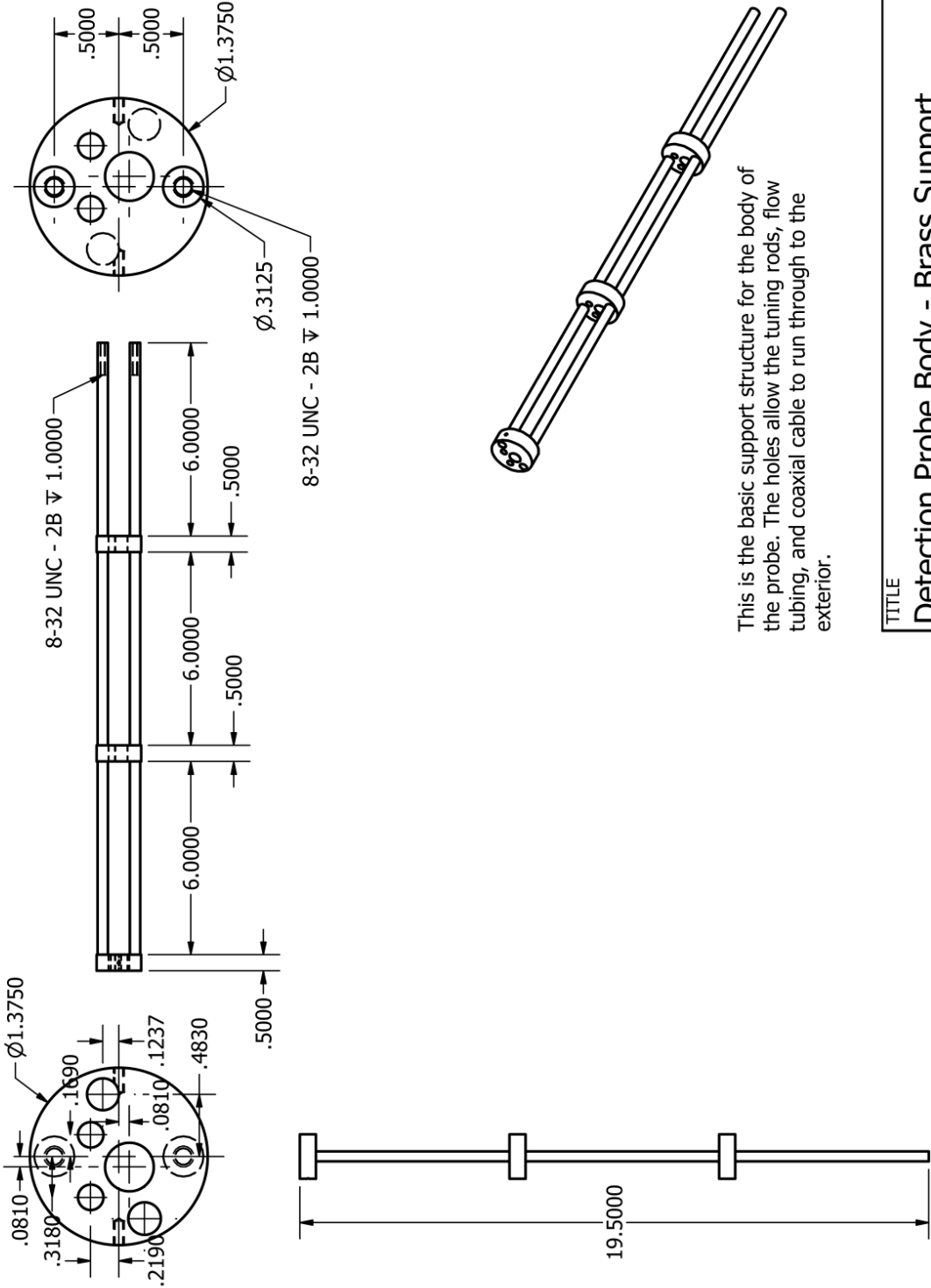
Figure A.3: Detection probe body - brass support
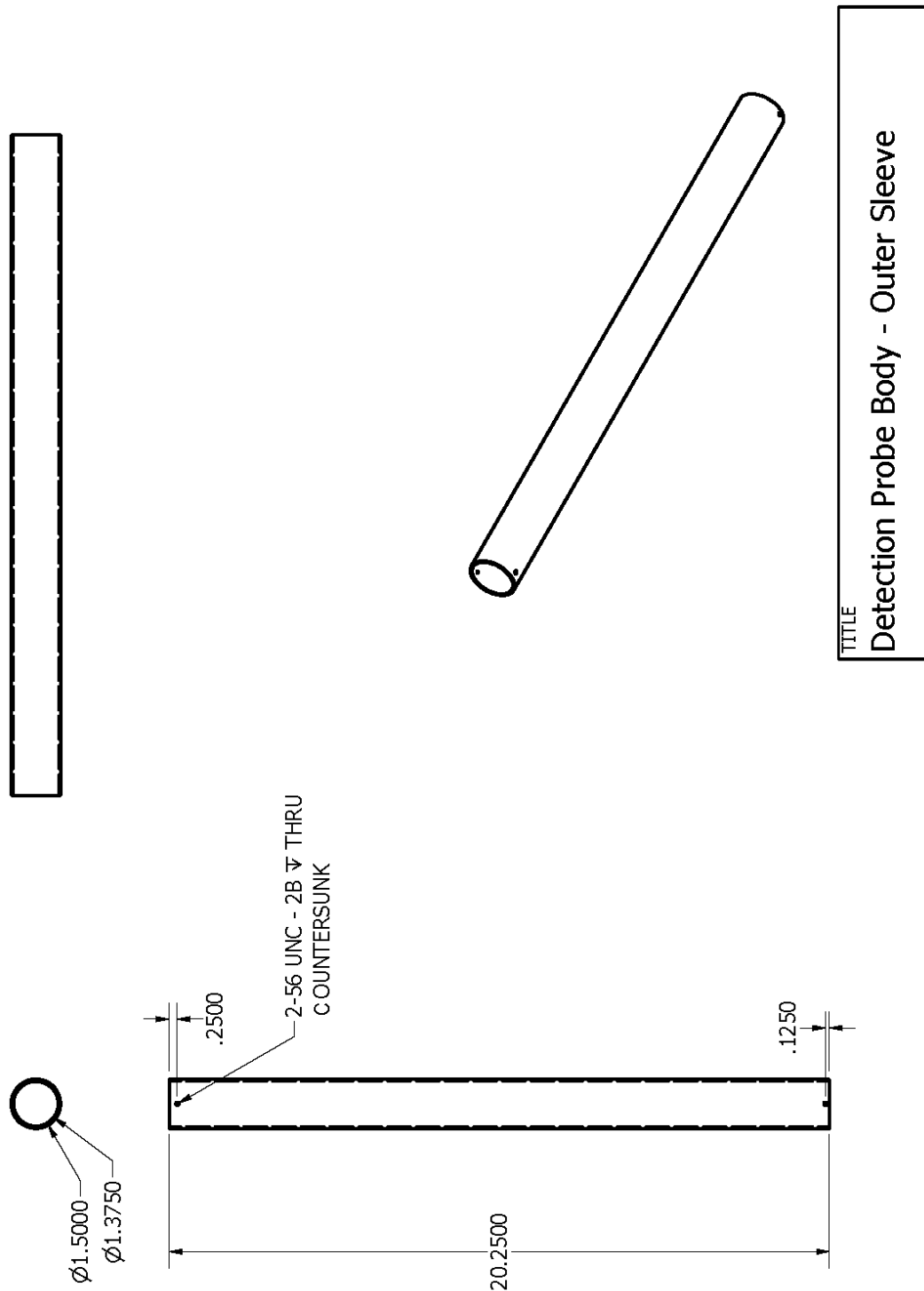
Figure A.4: Detection probe body - outer sleeve

This circuitboard is designed for use with Johanson 5641 non-magnetic capacitors (1-30 pF), which bridge the metallic regions using the holes specified in the diagram. Often, additional small fixed or variable capacitors may be added to the LC circuit in order to move the resonance to the desired frequency. As with the rest of the probe, this board can be easily redesigned to suit the needs of a particular user.

substrate (milled away)

copper

the coaxial cable is fed in here, with the ground soldered to the left and the lead soldered above, past the gap

TITLE
Probe Circuitboard

Figure A.5: Microcoil probe - circuitboard
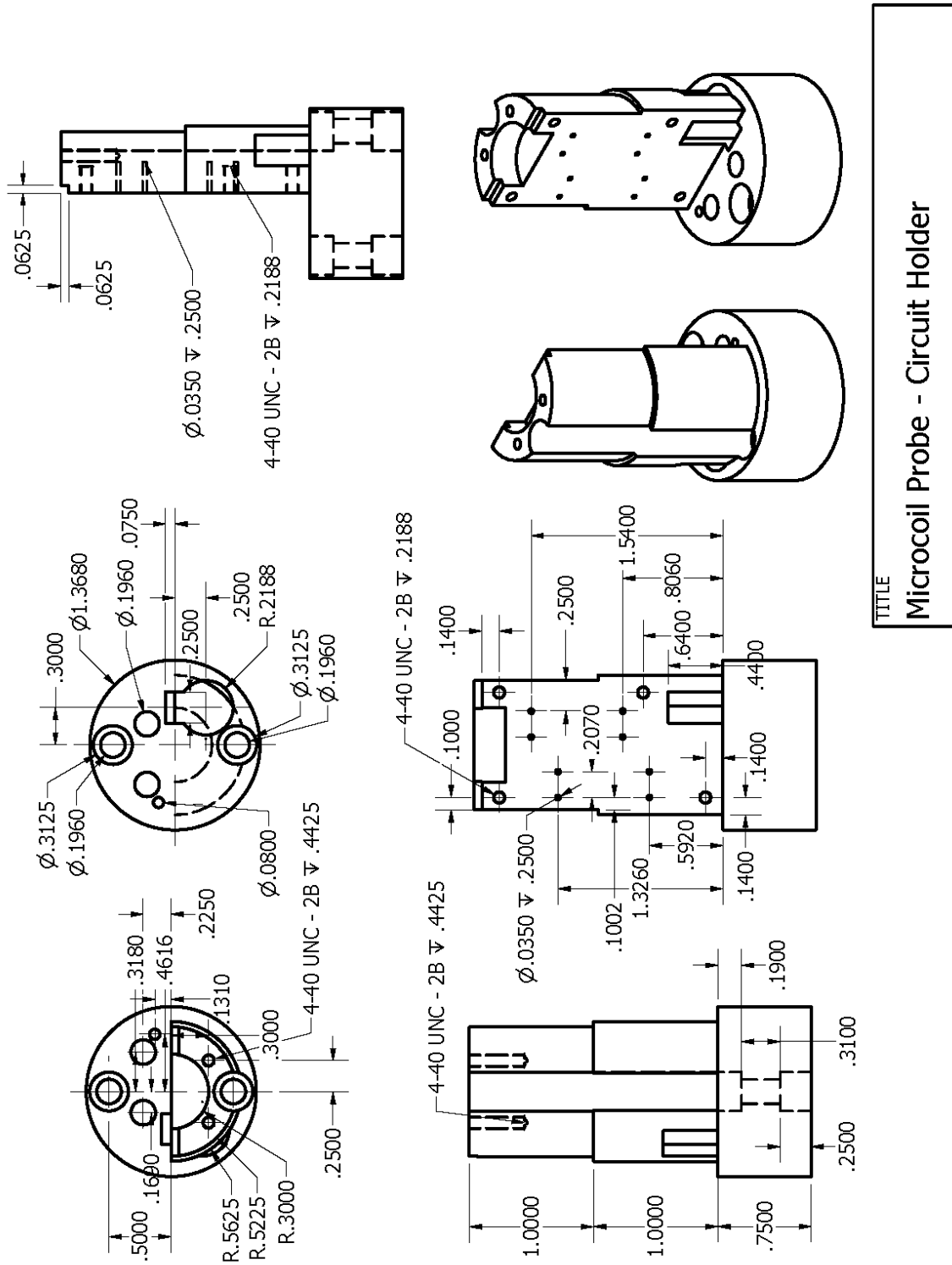
Figure A.6: Microcoil probe - circuit holder
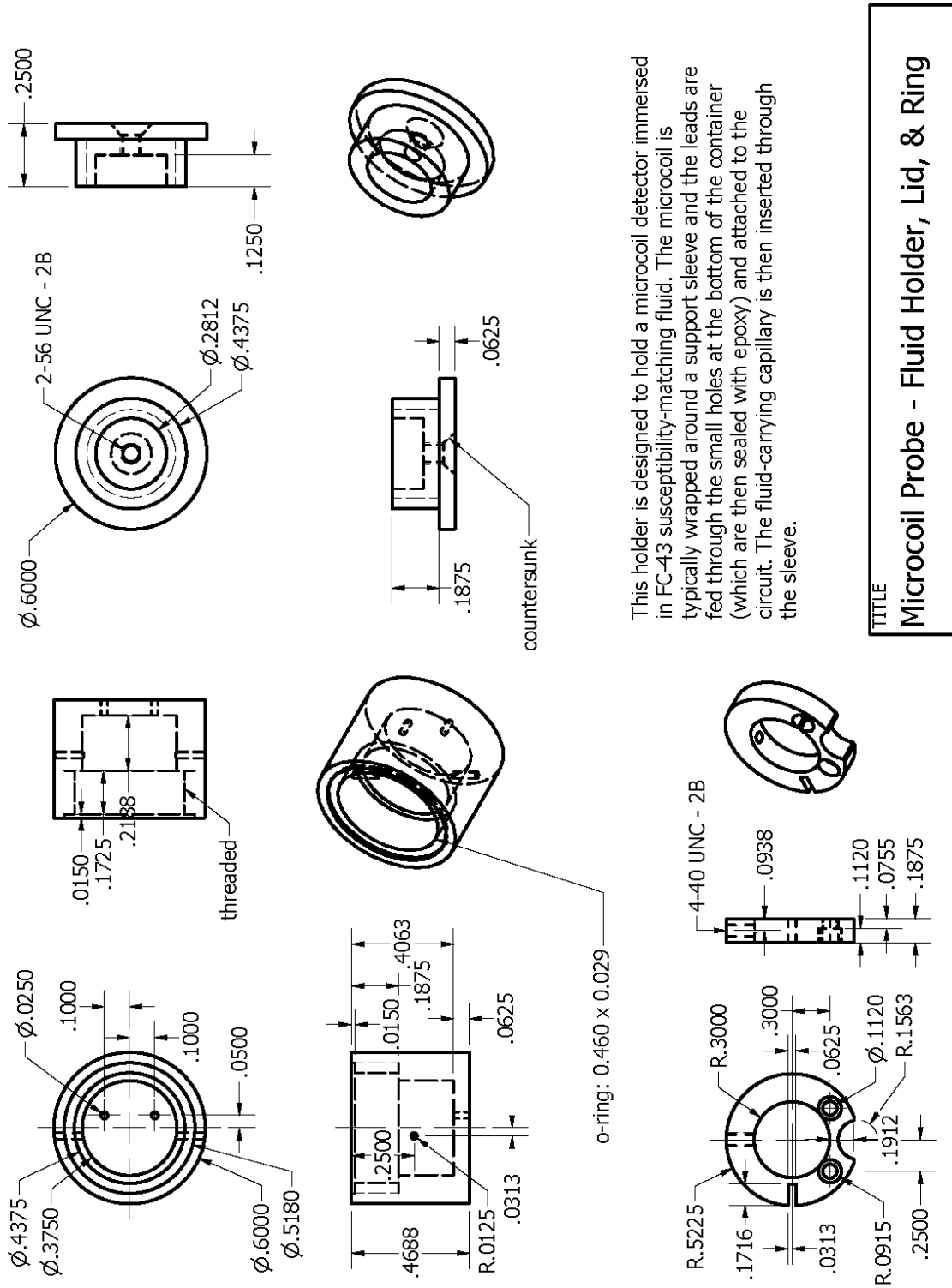
This holder is designed to hold a microcoil detector immersed in FC-43 susceptibility-matching fluid. The microcoil is typically wrapped around a support sleeve and the leads are fed through the small holes at the bottom of the container (which are then sealed with epoxy) and attached to the circuit. The fluid-carrying capillary is then inserted through the sleeve.

TITLE
Microcoil Probe - Fluid Holder, Lid, & Ring

Figure A.7: Microcoil probe - fluid holder, lid, & ring

Figure A.8: Microcoil probe - circuit shield

A.2 Surface Coil Encoding Probe

Schematics for a modular surface coil encoding probe are given in the following pages. I designed and constructed this probe in order to provide a low-cost alternative to the use of a standard NMR volume encoding probe (which typically run into the tens of thousands of dollars). The surface coil geometry is also a natural fit when dealing with planar regions, such as microfluidic chips. The probe is constructed to accomodate the circuitboard shown in the previous set of schematics. While a combination of small chip capacitors can be used, I have found it beneficial to instead add a variable capacitor (in series with the coil), in order to more easily match the circuit resonance to the magnet frequency. To enable easy access to this capacitor without having to remove the outer shield, a small hole was cut in the shield directly above it, large enough for a screwdriver to pass through to adjust the capacitance. The design of the probe is discussed further in Section 3.3.2.
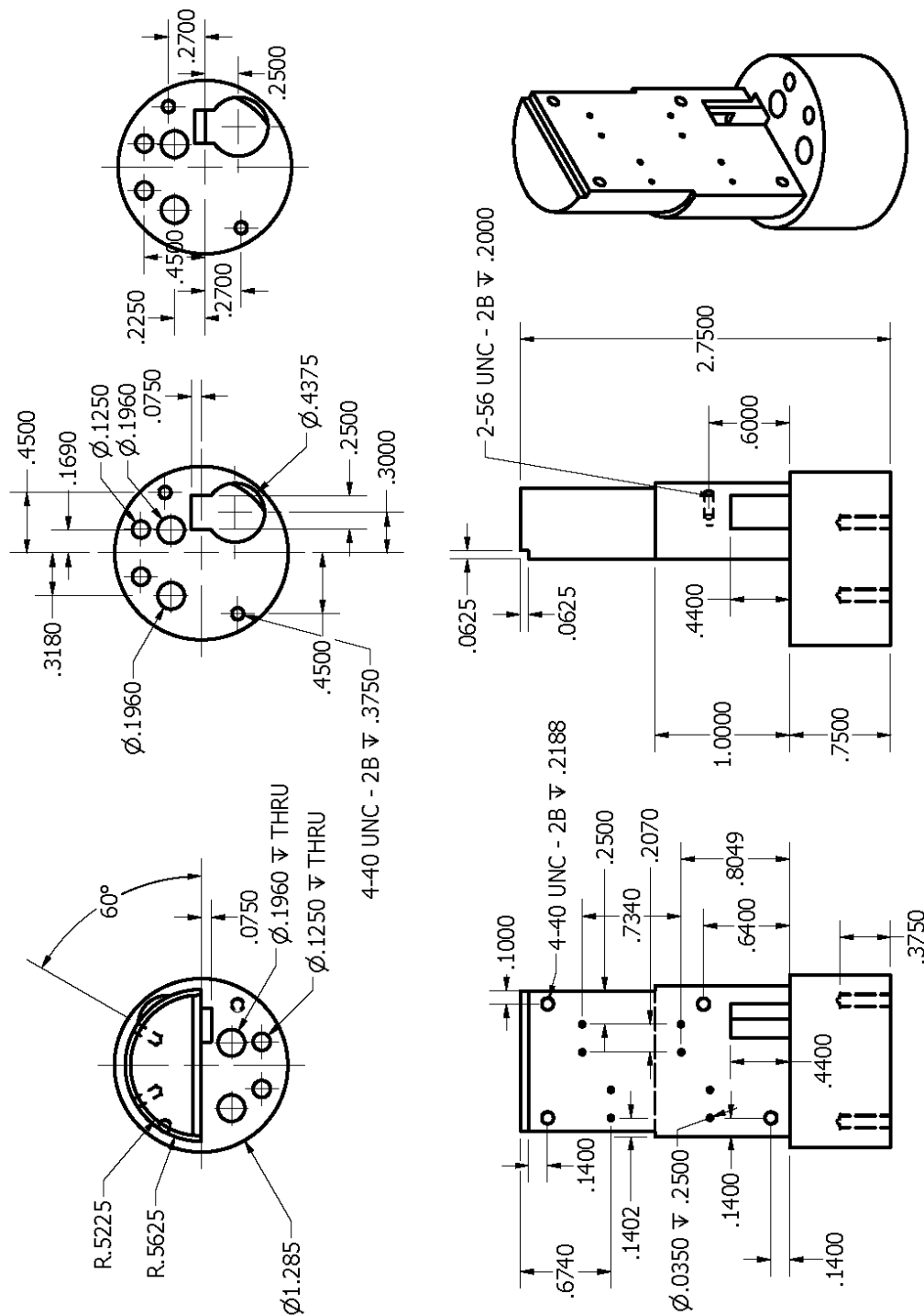
Figure A.9: Surface coil probe - circuit holder

Ø.1120 THRU

2-56 UNC - 2B

4-40 UNC - 2B ▼ .2500

holes for flow tubing

sleeve attachment point

attachment point for
the circuitboard holder

TITLE
Surface Coil Probe - Circuit Shield

Ø1.2850
Ø1.1250
R.5300
.2500
R.0900
Ø.1250

.2000

.2500

.3000

.5000

.3500
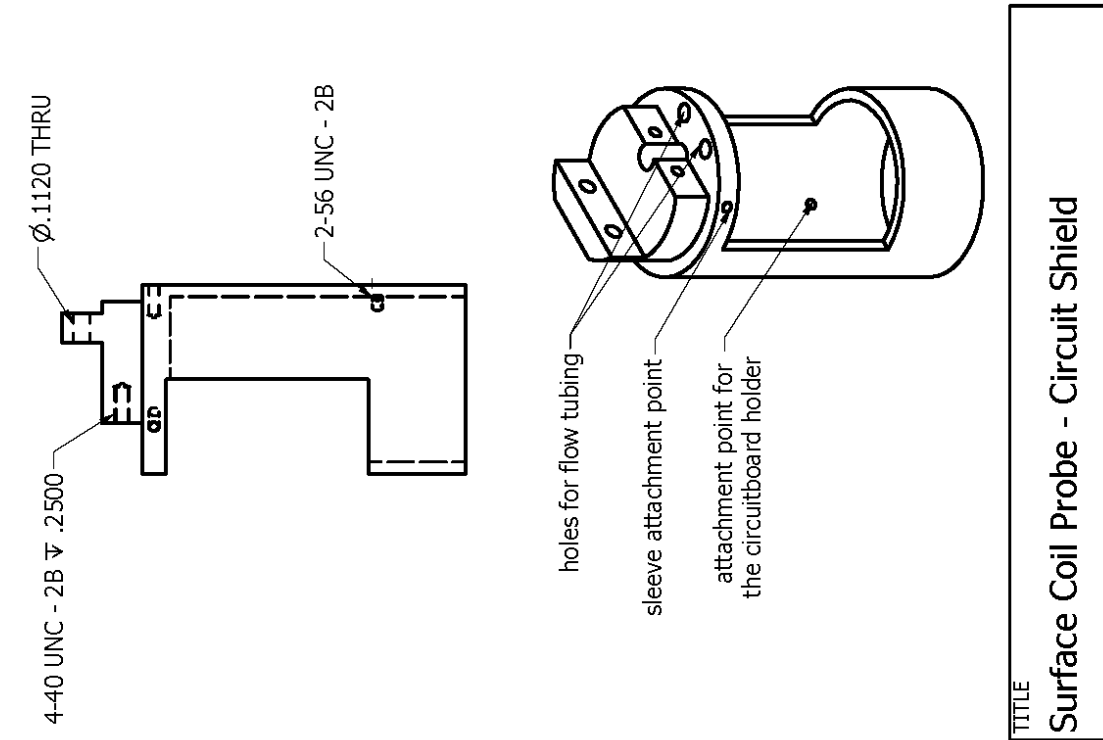
.275

.2500

.1625
.1869

1.375
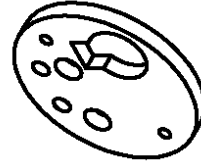
.3738

.275

.2500

2.7500

.6625

Figure A.10: Surface coil probe - circuit shield
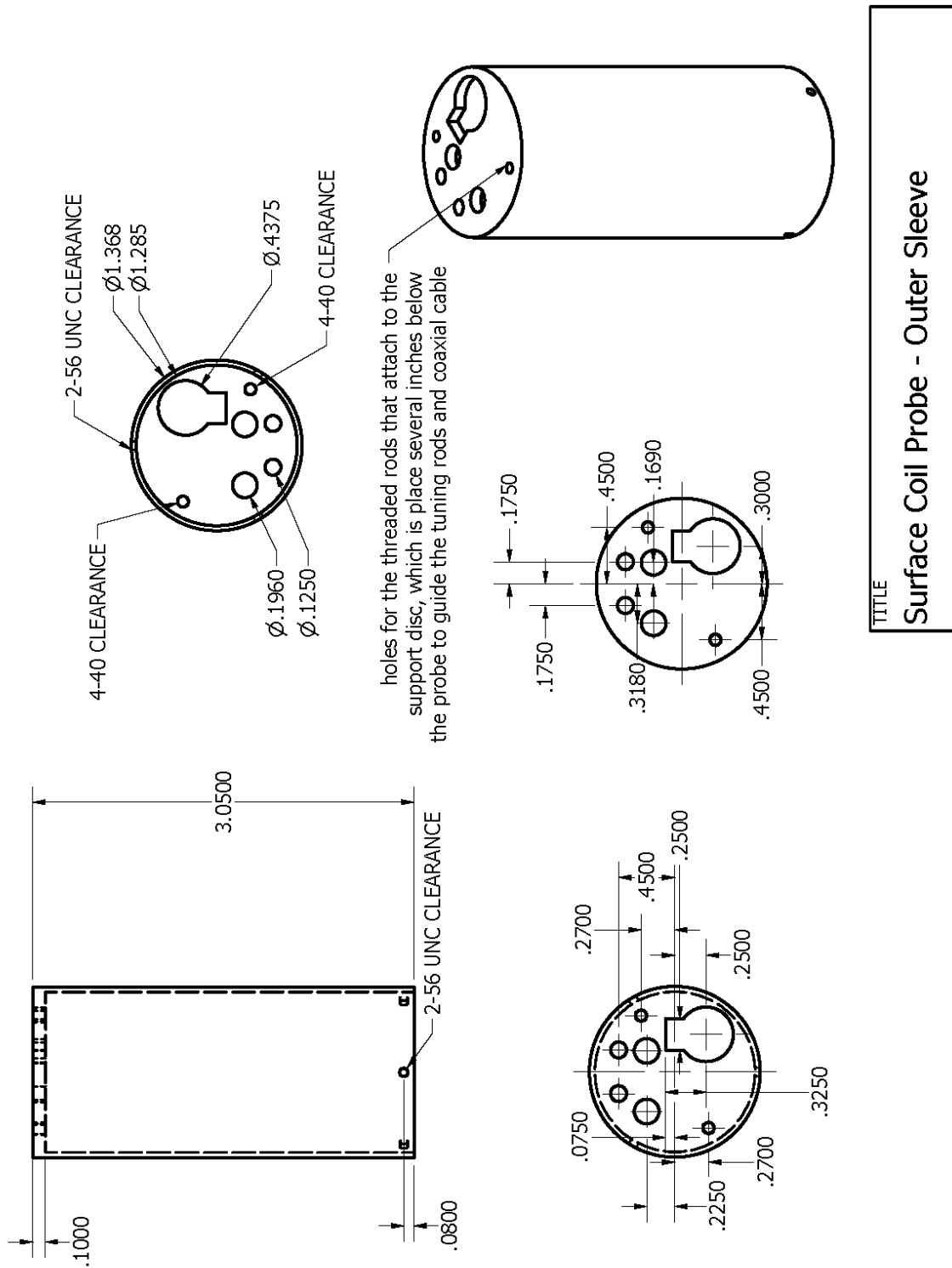
Figure A.11: Surface coil probe - outer sleeve
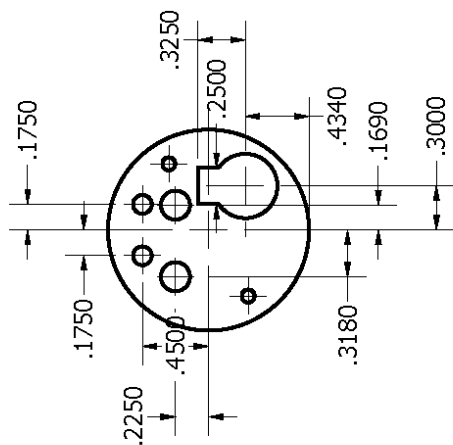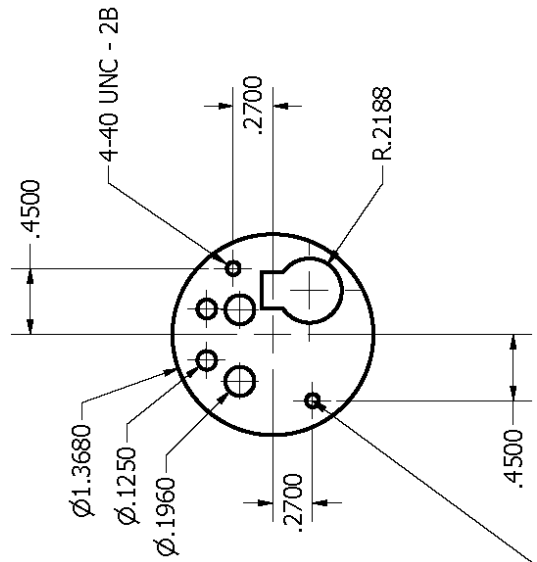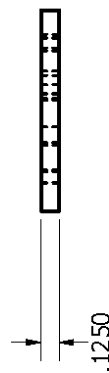
Figure A.12: Surface coil probe - supporting disc